Two Degrees of Freedom Miniaturized Gyroscope based on Active Magnetic Bearings

THÈSE N^{O} 4154 (2008)

PRÉSENTÉE LE 28 NOVEMBRE 2008
À LA FACULTÉ SCIENCES ET TECHNIQUES DE L'INGÉNIEUR
LABORATOIRE DE SYSTÈMES ROBOTIQUES 1
PROGRAMME DOCTORAL EN SYSTÈMES DE PRODUCTION ET ROBOTIQUE

ÉCOLE POLYTECHNIQUE FÉDÉRALE DE LAUSANNE

POUR L'OBTENTION DU GRADE DE DOCTEUR ÈS SCIENCES

PAR

Thomas BOSGIRAUD

acceptée sur proposition du jury:

Prof. M.-O. Hongler, président du jury
Prof. H. Bleuler, directeur de thèse
Dr D. Hoover, rapporteur
Prof. T. Mizuno, rapporteur
Prof. Y. Perriard, rapporteur

ÉCOLE POLYTECHNIQUE
FÉDÉRALE DE LAUSANNE
Suisse
2008

The evolution of stoicism along different periods of history:

Antic Greece:	*ανεχου και απεχου*
Rom:	*sustine et abstine*
France:	*tais-toi et nage*

Acknowledgements

I wish to express my thanks to my thesis advisor Prof. Hannes Bleuler, who offered me the possibility to do this study and supported me all through this work. My thanks are also going to my thesis jury composed of Prof. Max-Olivier Hongler, Prof. Takeshi Mizuno, Dr. David Hoover and Prof. Yves Perriard, who took so much of their time on reviewing this dissertation.

For the (re-re-re-re-) manufacturing of my prototypes, I would like to thank the people of our workshops, especially, Marc Salle, Jean-Jacques Crozat and Claude Amendola. Their patience and advice on better mechanical arrangements made these prototypes work. I would also like to acknowledge Dr. Ryouichi Takahata and Mr. Takayuka Ishigami from JTEKT Corp. for their cooperation to this work.

I would like to thank my colleagues and friends from the Laboratoire de Systèmes Robotiques I. Without their advice about diverse directions to explore inside and offside the laboratory, this thesis would have stayed a non rotating work. Two persons of the laboratory would deserve to be placed as coauthor of this thesis: Dominique and François. Special thanks are going to Roger, Laurent, Lindo, Guillaume (so many yellow coffees with bubbles have made him a full member of the lab), Thomas and Dejan.

A gyroscope needs a good spinning to be efficient, so does the so-called "calebasse". This egg-shaped object drags friendships in its whirl. I would like to thank my rugby partners on the field or on the tap. I would particularly like to mention Marc and Thomas who had a direct influence on this work.

I would like to express the everlasting love of a son to my mother Viviane. I would like to emphasize the love of a brother to my sister Marie and my brother Mathias and my gratitude to Antoine for making my sister happy. My love obviously goes to my family: Catherine, Claudine et Philippe, Pierre et Marie-Charlotte.

I address all my gratitude to Yves, Sabine and all my brothers and sisters in law.

Cette thèse est dédiée à trois personnes en particulier. Mon Grand-Père, le Dr. Ervin Zalán, qui m'a inspiré le goût de l'ingénierie. Mon Père, le Dr. François Bosgiraud, qui est ce Monsieur qui démontre par sa conduite et sa retenue de tous les jours que la qualité d'une personne n'est affaire ni de mots ni de paraître. Mon épouse et la femme de ma vie, Camille, qui m'a soutenu, supporté (et continue), motivé et appris l'Amour.

Résumé

L'introduction du freinage ABS dans les voitures a révélé l'importance croissante des capteurs inertiels. Parmi toutes les données caractérisant les mouvements d'un véhicule, la vitesse angulaire décrit la variation de l'assiette de ce dernier. L'art de mesurer la vitesse angulaire a été baptisé gyroscopie (du Grec $\sigma\kappa o\pi\varepsilon\iota\nu$=observer et $\gamma\upsilon\rho o\varsigma$=rotation) par Foucault en 1852. Les gyroscopes actuellement disponibles sont soit des instruments de très haute précision (et d'un prix en conséquence), utilisés notamment dans les avions, soit des produits meilleur marché mais souffrant d'un tel manque de sensibilité que leur utilisation pour la navigation de véhicules est impossible. Ainsi, il existe un besoin réel de gyroscopes alliant bas prix et précision. Cette thèse présente le développement d'un gyroscope miniature fondé sur la technologie des paliers magnétiques actifs (AMB). L'avantage d'un tel outil est de faire léviter la masse en rotation la libérant ainsi de tout lien mécanique avec la base de l'instrument, lien à l'origine des prix exorbitants des gyroscopes mécaniques classiques.

Cette thèse, présente deux prototypes de gyroscopes AMB. Le premier s'appuie sur la *détection de l'orbite d'une bille*, méthode développée durant ce travail. En raison des incertitudes liées à la non linéarité inhérente aux AMB, on a choisi de contrôler la position de la masse en sustentation de manière adaptative. Des mesures effectuées sur ce prototype ont démontré la faisabilité de cette méthode avec une bille décrivant une orbite soit circulaire soit verticale.

Le second prototype repose sur le théorème du moment cinétique. Pour pallier les incertitudes liées aux AMB et les couplages entre les forces dans ce prototype, un compensateur H_∞ asservit la position de la masse en lévitation. Des simulations ont permis de comparer trois différents types de régulateurs H_∞ en prenant la qualité de la mesure de la vitesse angulaire comme critère de sélection. Finalement, un contrôleur H_∞ comprenant un correcteur d'anticipation a démontré, par des simulations réalisées sur le second prototype de gyroscope, les meilleures performances.

Mots clé: *navigation, gyroscope, vitesse angulaire, lévitation magnétique, contrôle adaptatif, contrôle* H_∞.

Abstract

The introduction of the active blocking system, better known as ABS, into cars revealed the growing need for inertial sensing. Among other data, that permit to apprehend the movements of a vehicle, the measurement of the vehicle angular velocity describes the change rate of the vehicle attitude. This measurement has been called by Foucault in 1852 gyroscopic sensing (from the Greek words $\sigma\kappa o\pi\varepsilon\iota\nu$=observe and $\gamma\upsilon\rho o\varsigma$=rotation). The currently available gyroscopes are either very high precision instruments (hence very costly), used in planes, or cheaper products but with a lack of sensitivity to be used in vehicle navigation. Therefore, a real need for gyroscopes combining low cost and precision exists. This thesis proposes to develop a gyroscope based on miniaturized active magnetic bearings (AMB). The advantage of such a device is that the spun mass will be levitated what frees it from any mechanical link to the base of the instrument what render precise classical mechanical gyroscopes so expensive.

This thesis presents two prototypes of AMB based gyroscopes. The first one relies on the *ball orbit sensing method* which is a new theory proposed in this work. Because of the uncertainties due to the nonlinearities inherent to active magnetic bearings, the position of the levitated mass is adaptively controlled. Measurements performed on the prototype have demonstrated the feasibility of this solution with a ball following either a *circular* or a *vertical* orbit.

The second designed prototype relies on the Newton's second law of motion. Due to the AMB inherent uncertainties and to the force coupling present in the proposed prototype, it has been chosen to drive the levitated mass with a H_∞ controller. Simulations are run to compare three different H_∞ controllers with the quality of the angular velocity measurement as criterion. Finally, a feed forward H_∞ controller showed the best performances in terms of angular velocity measurements during simulations run on the prototype developed during this thesis.

Keywords: *navigation, gyroscope, angular velocity, magnetic levitation, adaptive control, H_∞ control.*

Terminology

Abbreviations

AMB: Active Magnetic Bearing
CM: Center of mass
DOF: Degree of Freedom
DTG: Dynamically Tuned Gyroscope
EGG: External Gimbal Gyroscope
GPS: Global Positioning System
IFOG: Interferometric Fiber Optic Gyroscope
IMU: Inertial Measurement Unit
JTEKT: Company created by a merging agreement among of Koyo Seiko and Toyota Machine Works
LFT: Linear Fractional Transformation
LTI: Linear Time Invariant
MOG: Micro Optic Gyroscope
MIMO: Multiple Inputs Multiple Outputs
MRAC: Model-Reference Adaptive Controller
PMB: Passive Magnetic Bearinf
Pitch: Rotor inclination about the stator Y-axis
Roll: Rotor inclination about the stator X-axis
RFOG: Resonant Fiber Optic Gyroscope
RLG: Ring Laser Gyroscope
TFG: Tuning Fork Gyroscope
SDFG: Single Degree of Freedom Gyroscope
SISO: Single Input Single Output
SPR: Strictly Positive Real
STC: Self-Tuning Controller
Vehicle: Object on which acceleration and angular velocity sensors are fixedly mounted

Subscripts and Superscripts

acc: Acceleration
amb: State space model of the gyroscope expressed in the AMB actuator coordinates
gyro: Data related to the gyroscopic effects exerted on the rotor
m: Minus direction of a coordinate axis
p: Plus direction of a coordinate axis
rs: Movements of the rotor expressed in the stator coordinate frame
sf: Movements of the stator expressed in the inertial reference frame
u: Unbalance effects

Physical Constants

χ: Magnetic susceptibility
μ: Magnetic permeability

Contents

Résumé **vii**

Abstract **ix**

Terminology **xi**

1 Introduction **1**

1.1 Motivations 1

1.2 Originality and Objectives 2

1.3 Thesis Outline 3

I Introduction to Gyroscopic and to AMB **5**

2 Gyroscopic Sensing **7**

2.1 Coordinate Systems 7

2.1.1 Absolute and Relative Coordinate Systems 7

2.1.2 The Euler Angles 8

2.2 Families of Gyroscopes 9

2.2.1 Mechanical Gyroscopes 9

2.2.2 Vibrating Gyroscopes 14

2.2.3 Optical Gyroscopes 16

2.3 Summary 18

3 Active Magnetic Bearings **19**

3.1 Definition 19

3.2 AMB: Interest and Applications 20

II 1^{st} Gyroscopic Sensing Method: Ball Orbit Observation 23

4 Ball Orbit Observation 25

4.1 Description of the Measurement Principle 25

4.2 Angular Velocity Computation 26

4.2.1 Computation of the Disc Normal Vector Coordinates 26

4.2.2 Computation of the Angle between the Normal Vector and the Z-axis 27

4.2.3 Computation of the Angular Velocity 27

5 Prototype Design and Control 29

5.1 Prototype Design 29

5.2 Prototype Model 29

5.2.1 Force calculation 29

5.2.2 Transfer Function of the Electromagnetic Force 33

5.3 Prototype Control 34

5.3.1 PID Control 34

5.3.2 Electronics Transfer Function 36

5.3.3 Adaptive Control 37

6 Experimental Results 43

6.1 Test Rig 43

6.2 Experiments: Moving Rotary Table 44

6.3 Experiments: Noise Measurement 45

6.4 Performance 46

7 Conclusions about the Ball Orbit Method 47

7.1 Advantages 47

7.2 Inconvenients 48

III 2^{nd} Gyroscopic Sensing Method: Cylindrical Spinning Rotor 49

8 Mechanical Design 51

8.1 Constraints on the Design 51

8.2 Actuation System 51

8.2.1 Radial Actuators 51

8.2.2 Axial Actuators 54

8.3 Rotor Design 54

8.4 The Induction Motor 56

8.5 Summary 57

9 Model of the AMB based Gyroscope 59

9.1 Actuators 59

9.1.1 Single Actuator 59

9.1.2 Complete Actuation System 64

9.2 Rotor Mechanics 66

9.2.1 Gyroscopic Effects 66

9.2.2 Unbalance Effects 69

9.2.3 Rigid Body Model 69

9.3 Complete Model 70

9.4 Angular Velocity 72

9.5 Summary 74

10 Gyroscope Control 75

10.1 Control Method 75

10.2 Loop Shaping 76

10.3 Introduction to Robust Control 77

10.3.1 Representing Uncertainty 77

10.3.2 The H_∞ Problem 78

10.3.3 The Weighted H_∞ Synthesis 82

10.3.4 Two DOF H_∞ Controller 86

10.3.5 H_∞ Controller with Explicit Integrator 89
10.4 Design of the H_∞ Controller 90
10.4.1 Control in the AMB Actuator Coordinates 90
10.4.2 Choice of the Weights 91
10.5 Summary 92

11 Theoretical Tests and Results **93**
11.1 Introduction 93
11.2 Unspun Rotor:
Trajectory Tracking 94
11.3 Maximal Spinning Speed 95
11.4 Angular Velocity Measurements 96
11.4.1 Analysis of the Mean Error 96
11.4.2 Effect of a $2g$ Acceleration on the Plant 97
11.4.3 Conclusion about the Gyroscope Tests 98

12 Conclusions about the Cylindrical Spinning Rotor Method **101**
12.1 Advantages 101
12.2 Drawbacks 102

13 Conclusion **103**
13.1 Summary 103
13.2 Outlook 104

IV Appendices **107**

A Kinematics **109**
A.1 Rotor Angular Momentum 110
A.1.1 Angular Velocity of (G,x_r, y_r, z_r) relatively to (O,x_f, y_f, z_f) . 110
A.1.2 Angular Velocity of the Rotor 110
A.1.3 Rotor Angular Momentum 110
A.2 Derivation of the Angular Momentum 111

A.2.1 Derivation of the Rotor Angular Momentum Relatively to the Rotor Reference Frame 111
A.2.2 Computation of the Cross Product of the Newton's 2^{nd} Law of Motion 111
A.2.3 Complete expression of the Derivative of the Rotor Angular Momentum 112

B Matrices 113
B.1 Mechanical Matrices 113
B.2 Transformation Matrices 115

C Model of the Torques Generated by the AMB Radial Actuators 117

D Matrix Theory and Norms 121
D.1 State Space Representation of a System 121
D.2 Frequency Domain Representation 121
D.3 Closed Loop Transfer Functions 122
D.4 Signal and System Norms 122
D.4.1 Definition of a Signal Norm 122
D.4.2 The H_∞ Norm of a System 123
D.5 Singular Values 123

E Sensing System 125
E.1 Sensor Selection 125
E.2 Configuration Choice 125
E.3 Position and Angle Calculation 126

List of Figures 131

List of Tables 133

Bibliography 139

Curriculum Vitae 141

Chapter 1

Introduction

1.1 Motivations

The tremendous growth of the Global Positioning System (GPS) has shown how important vehicle navigation becomes in our everyday life. In this particular case, the position of a vehicle (for example a car or the apron of the "viaduc de Millau [Lib08]") is detected by satellites and sent back to the vehicle driver so that he/she can adjust the vehicle instantaneous trajectory in order for the vehicle to reach its destination.

More generally, navigation consists in a set of constraints on the dynamics of a vehicle; these constraints on the vehicle can be for example its trajectory (travel between two geographical locations for the GPS), its attitude regarding the ground (all four wheels of a car must stick on the road)... This requires sensors to inform the driver (human being or computer) about the current dynamical state of the vehicle. Thus the driver can adapt his action in order to stick to predefined constraints.

Two ways of navigation sensing exist: sensing the vehicle dynamics from its outside or from its inside. The two families can according to the circumstances coexist. Outside navigation sensors are for example the GPS, radars, light reflectors... The second sensor family is better known as *inertial sensors* [Law98]. For example, the magnetic compass belongs to the latter family.

Inertial navigation (named after inertial sensors) uses gyroscopes and accelerometers to tell the driver about the vehicle current state of motion. With the help of this information, the driver can compute the vehicle trajectory.

Inertial navigation has the main advantage of being self sufficient, i.e. the vehicle does not need to communicate with an external source of information. This advantage has firstly been used by the military consortium for material (submarines among others) that, in war circumstances, must stay invisible for the enemy.

Twenty years ago, the inertial sensor price started to diminish because of a change of technology towards the electronics. By breaking this prosaic bottleneck, the inertial sensors were admitted into civil applications.

Beside the price, two criteria for a large scale commercialization of inertial sensors are few maintenance needs and precision. Indeed, depending on the application, short term or long term precision are required [Law98]. Mechanical gyroscopes are more accurate for short term measurements whereas optical gyroscopes better behave the latter one. Therefore, an overlap of the two domains of use is desirable.

In the case of mechanical gyroscopes, the angular velocity is measured by means of a mass spun about its inertia axis (more details can be found in §2)). One main limit of mechanical gyroscopes is the link between the spun mass and the base of the instrument. As a matter of fact, the ball bearings will induce friction responsible for imprecisions and fatigue (a limit for the maintenance criterion) which can even lead to failure. Moreover, limitations in the instrument sensitivity will occur due to this contact between the mass and the base.

This observation led to the idea of levitating, by means of electrostatic or magnetic forces, the spun mass to prevent it from any contact with the base. Hence, this levitation should extend the domain of use of mechanical gyroscopes towards short term use.

1.2 Originality and Objectives

Magnetic Bearings have been implemented in various applications, such as high precision accelerometers or high rotational speed motor with very low vibrations, which were limited by the friction due to conventional mechanical bearings. The main originality and goal of this thesis is the adaptation of the magnetic levitation advantages to a high precision gyroscope. It must be noted that the developed gyroscope can only measure the roll and tilt angular velocities, hence its name of two-degree-of-freedom gyroscope.

Two fully different methods to measure angular velocity have been investigated in this thesis. The first solution is called *ball orbit observation method* and has been developed in this work, the second solution relies on the second law of Newton. One key component to reach high precision in the measurement is the levitation control accuracy, which is correlated to the desired gyroscope bandwidth and sensitivity. This accuracy depends among other on the ability of the controller to compensate for uncertainties of the gyroscope model and for external disturbances. On that purpose, two controllers have been developed during this study: an adaptive controller for the gyroscope based on the *ball orbit observation method*, and a robust two-degree-of-freedom H_∞ controller including an explicit integrator for the other gyroscope.

Another challenge of this thesis consists in the integration of the active magnetic bearings within a cube of 40[mm] ridge length.

1.3 Thesis Outline

The structure of the thesis is organized as follow:

- **Part I** consists of an overview of the existing types of gyroscopes with a short explanation of the principles on which they rely (Chapter 2), and of a description of active magnetic levitation with its advantages and its domains of application (Chapter 3). We will explain the interest to apply this technology to gyroscopic sensing.

- **Part II** presents the gyroscope prototype based on the *ball orbit observation method* which will be introduced in Chapter 4. Chapter 5 describes the design of the prototype mechanics and the synthesis of its adaptive control. The prototype is experimentally evaluated in Chapter 6, what permits to conclude on the advantages and disadvantages of the *ball orbit observation method* (Chapter 7).

- **Part III** exposes the sensing method based on the Newton's second law of motion; this method will be referred in this thesis as *cylindrical spinning rotor method*. Chapter 8 presents the design of the gyroscope prototype relying on this sensing method. Chapter 9 consists of the modeling of the gyroscope and of an explanation of the method to measure the angular velocity of the vehicle. Chapter 10 introduces the H_∞ robust control. Some strategies to control the actively levitated shaft according to the sensor bandwidth and sensitivity will be exposed. The synthesis of a two-degree-of-freedom H_∞ controller including an explicit integrator will be described in this chapter. In chapter 11 simulations based on the different control strategies will be analyzed. This will permit to deduce some rules and criteria to design a controller that fits the needs required to use Active Magnetic Bearings as a gyroscope. Finally, Chapter 12 lists the advantages and disadvantages presented by the *cylindrical spinning rotor method*.

- **Chapter 13** finally concludes the thesis with a summary, a discussion and an outlook for future works.

Part I

General Introduction to Gyroscopic Sensing and to Active Magnetic Bearings

Chapter 2

Gyroscopic Sensing

The name *gyroscope*, which is a concatenation of the Greek words $\sigma\kappa o\pi\varepsilon\iota\nu$ (observe) and $\gamma\upsilon\rho o\varsigma$ (rotation), was introduced in 1852 by the French scientist Léon de Foucault[Fou52b] to describe any instrument that signals or measures a rotation.

There are three families of gyroscopes: mechanical, vibrating and optical gyroscopes. These families and the theoretical principles, on which they rely, will be briefly presented in this chapter.

2.1 Coordinate Systems

2.1.1 Absolute and Relative Coordinate Systems

Before evoking the different existing types of gyroscopes, appropriate coordinate systems should be introduced. On that purpose, we will describe Fig.(2.1). A reference frame (O,x_f, y_f, z_f) is bound to the ground and therefore is considered fix in space, hence the name of *absolute* reference frame.

A second reference frame (S,x_s, y_s, z_s) bound to the pink cube (the sensor stator in our case) is introduced. This reference frame is called *relative* reference frame. The movements of the pink cube within the absolute reference frame are fully described by the movements of (S,x_s, y_s, z_s) relatively to (O,x_f, y_f, z_f).

A blue cylinder (the active part of the sensor, for example the rotor for mechanical gyroscopes) can freely move in space. Once again to describe the movements of the cylinder, a reference frame (G,x_r, y_r, z_r) bound to this cylinder is introduced.

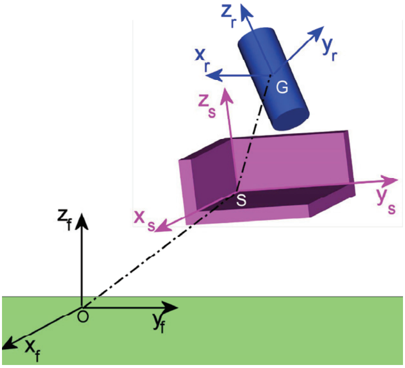

Figure 2.1: Representation of the different reference frames that will be used throughout the thesis.

In the following, the subscript (sf) represents the movements of the stator (the pink object) relatively to the fix reference frame, the subscript (rs) the movements of the rotor (the blue cylinder) relatively to the stator reference frame, the subscript (rf) the movements of the rotor relatively to the fix reference frame.

2.1.2 The Euler Angles

For the rest of this thesis, the Euler angles will be used to describe the behavior of a coordinate system relatively to another reference frame. To present the Euler angles, the rotations of (S,x_s, y_s, z_s) relatively to (O,x_f, y_f, z_f) will be described. The rotations of (G,x_r, y_r, z_r) relatively to (S,x_s, y_s, z_s) can be described in a similar way.

Different definitions of the Euler angles exist depending of the sequence in which the rotations between the two coordinate systems are considered [1]. Throughout this thesis, we will consider (see Fig.(2.2)) that (S,x_s, y_s, z_s) is first subject to a rotation ϕ_y^{sf} around the vector y_f and then to a rotation ϕ_x^{sf} around an intermediate vector $x' = \cos\left(\phi_y^{sf}\right) \cdot x_f - \sin\left(\phi_y^{sf}\right) \cdot z_f$.

Therefore the complete rotation of (S,x_s, y_s, z_s) about the frame (O,x_f, y_f, z_f) is given by:

$$\vec{\phi}^{sf} = \phi_y^{sf} \cdot \vec{y}_f + \phi_x^{sf} \cdot \vec{x}'$$

---

[1] Rotations are not commutative, therefore once a rotation sequence has been chosen, it cannot be changed any more.

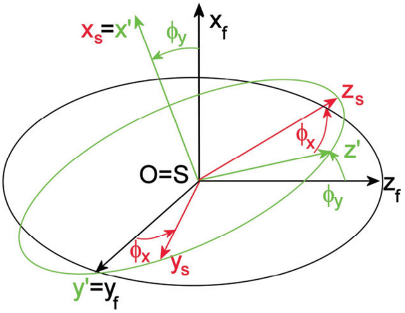

Figure 2.2: Rotation of (S,x_s, y_s, z_s) relatively to (O,x_f, y_f, z_f). First, rotation of (S,x_s, y_s, z_s) by an angle ϕ_y^{sf} (green) about y_f. Second, rotation of (S,x_s, y_s, z_s) by an angle ϕ_x^{sf} (red) about the intermediate vector $x^{'}$.

If the rotation $\vec{\phi}_{sf}$ is expressed in a frame i, it is noted $\left[\vec{\phi}_{sf}\right]_i$. With this notation, the expression of $\vec{\phi}_{sf}$ becomes:

$$\left[\vec{\phi}_{sf}\right]_f = \left[\vec{\phi}_{sf}\right]_s^T = \begin{bmatrix} c_y & s_x s_y & c_x s_y \\ 0 & c_x & -s_x \\ -s_y & s_x c_y & c_x c_y \end{bmatrix}_f \tag{2.1}$$

with $c_x = \cos(\phi_x^{sf})$ and $s_x = \sin(\phi_x^{sf})$.

2.2 Families of Gyroscopes

2.2.1 Mechanical Gyroscopes

The first modern gyroscope with a spinning mass was designed by the German scientist Bohnenberger in 1810.

2.2.1.a Principles

The gyroscopic effects can be derived from the Newton's Second Law of Motion[New87]:

$$\vec{\tau}|_{rf} = \left.\frac{d\vec{L}}{dt}\right|_{rf} = \left.\frac{d\left[J\vec{\Omega}\right]}{dt}\right|_{rs} + \vec{\omega}|_{rf} \times \left.\left[J\vec{\Omega}\right]\right|_{rs} \tag{2.2}$$

In Eq.(2.2), τ is the torque applied to the considered body (the blue cylinder in Fig.(2.1)), L its angular momentum, J its inertia matrix considered as constant in the following, ω the absolute (i.e. expressed in the fix reference frame) angular velocity of the rotating axes and Ω the angular velocity of the body.

In the following we consider a body with a symmetrical axis $Z|_r$. Therefore its inertia matrix is diagonal and the inertia J_x (resp. J_y) about the X-axis (resp. the Y-axis) will be called radial inertia and noted J_r in the following. The mentioned body spins about $Z|_r$ with an angular velocity Ω_z. Eq.(2.2) thus becomes:

$$\left.\begin{bmatrix} \tau_x \\ \tau_y \\ \tau_z \end{bmatrix}\right|_{rf} = \left.\left(\frac{d}{dt} \begin{bmatrix} J_r\Omega_x \\ J_r\Omega_y \\ J_z\Omega_z \end{bmatrix} \right)\right|_{rs} + \begin{bmatrix} J_z\Omega_z\omega_y \\ -J_z\Omega_z\omega_x \\ 0 \end{bmatrix} \tag{2.3}$$

Eq.2.3 shows that each component of the torque $\vec{\tau}$ has two kinds of effects on the spinning body:

1. the derivative term $J_i\dot{\Omega}_i, i \in \{x, y, z\}$, means that the effect of the component τ_i about the axis i is proportional to the angular velocity of the body about this particular axis.
2. the effect of the cross product term of the form $J_z\omega_i\Omega_z, i \in \{x, y\}$. In this case, a torque applied along a direction orthogonal to the spin axis will have no effect on the angular velocity magnitude, but it can change its direction (see fig.2.3). The angular velocity ω_x (resp. ω_y) is called **precession** rate about the x-axis (resp. y-axis). This effect is called the **gyroscopic** effect, and the corresponding law is referred to as **Law of Gyroscopics**.

The solutions of Eq.(2.3) contain the previously mentioned steady precession and an oscillatory term of frequency ω_n:

$$\begin{aligned} \omega_x &= -\tfrac{\tau_y}{J_z} + K_1\sin(\omega_n t) + K_2\cos(\omega_n t) \\ \omega_y &= \tfrac{\tau_x}{J_z} - K_1\cos(\omega_n t) + K_2\sin(\omega_n t) \end{aligned}$$

where $\omega_n = \frac{J_z}{J_r}\Omega_z$ is called the *nutation* frequency. The amplitude of nutation depends on the damping. Generally, two-axis mechanical gyroscopes (the only ones able to nutate) have small damping and therefore need electronics that can feed the instrument with a damping force.

Eq.(2.3) shows the stability advantage presented by a spinning body over a stationary one to measure angular velocity. As a matter of fact, a torque τ acting on the spinning body will induce an angular velocity $\omega_2 = \tau/(J_z\Omega_z)$, whereas in the case of a stationary body ($\Omega_z = 0$) it will be $\omega_1 = \tau/J_z \cdot t$ (the variable t representing

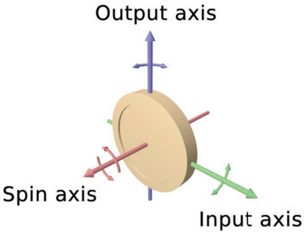

Figure 2.3: Law of gyroscopics. Diagram of a wheel rotating around an axis(spin axis in red). Reaction arrows about the output axis (blue) correspond to forces applied about the input axis (green), and vice versa [Kie08].

the time). Thus, the effect of τ will be $\Omega_z t$ times greater for the stationery body compared to the spinning one. For that reason, mechanical gyroscopes have been designed based on spinning bodies as in [Fou52a].

2.2.1.b External Gimbal (EGG)

As shown in Fig.(2.4), the rotor is mounted on gimbals. The rotor is spun by means of electrical energy transmitted through slip rings mounted on the different gimbal articulations. Finally, the gimbal angles can be measured with the help of potentiometers placed on these articulations.

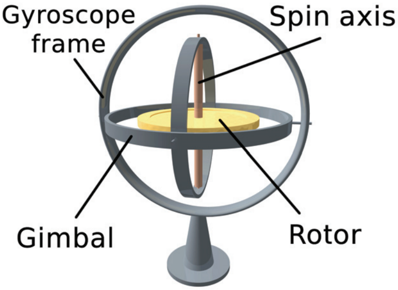

Figure 2.4: A two-axis external gimbal type gyroscope [Kie08].

Due to the encapsulation of the rotor within the gimbals, these gyroscopes present a small angular momentum compared to their size. Thus, their performance is not sufficient for inertial navigation.

2.2.1.c Dry Tuned Gyros

As shown in Fig.(2.5), a dry tuned gyroscope is made out of a rotating shaft, a gimbal, a momentum wheel and two pairs of flexible hinges. The rotating shaft supports the gimbal by means of a pair of flexible hinges. The momentum wheel is mounted on the gimbal through the second set of hinges, the direction of these last hinges is orthogonal to the first pair. This architecture was first described by Arnold and Maunder in the 1940's [Wil74].

Rotation of the gimbal causes a reaction at the rotor that is equivalent to a negative torsional spring stiffness. This effect occurs when the angular momentum of the shaft does not coincide with that of the rotor, the angular momentum of the gimbal jumping between that of the shaft and the rotor, at twice the speed of the rotor. Thus, careful selection of the torsional stiffness of the gimbal components and the rotational speed of the rotor allows the rotor suspension to have a net zero spring stiffness at a particular rotor speed, known as the tuned speed. Under these conditions, the rotor is decoupled from the motion of the rest of the sensor and hence its movement are free from the influence of the stator[How64].

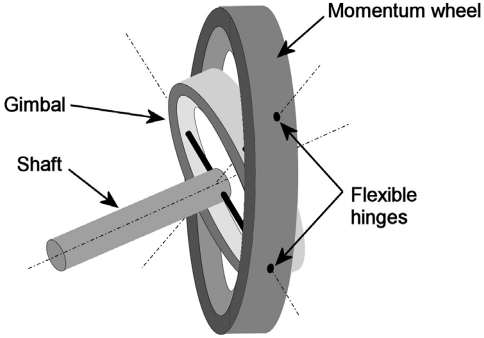

Figure 2.5: Dry Tuned Gyroscope.

A second advantage of the dry tuned architecture is that the wheel is placed on the outer side of the gyroscope, inducing a higher angular momentum compared to the gyroscope with external gimbals. A third advantage: because they are dry, they provide good performance over a wider range of temperature than single degree of freedom gyroscopes (SDFG) [Law98].

However, such advantages have a cost which is the high complexity of the flexures hinges design and of the servo due to DTG's low damping, cross coupling and nutation [Joo77]. Despite this complexity, DTG's have been commercialized, an example being the AN/ASN141 inertial sensor used navigation in the F-16 aircraft [Par08].

2.2.1.d Levitated Gyros

In conventional mechanical gyroscopes, the friction between the stator and the rotor is a source of measurement error. To avoid this problem, gyroscopes based on contactless levitation of the rotor inside the stator have been imagined.

2.2.1.d.i) Gas Bearing Gyros

For this gyroscope type (see Fig.(2.6)), the momentum wheel turns around a spherical bearing with a thin gas layer between the two moving parts. This type of gyroscope has been mounted on US intercontinental missiles because of its mean time-to-failure of over 1 million hours.

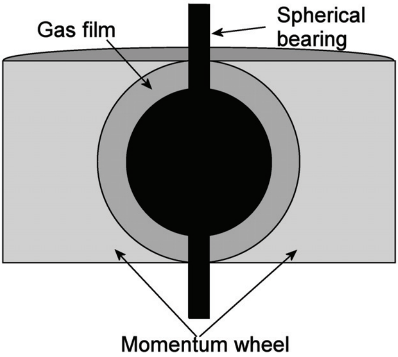

Figure 2.6: A gas bearing gyroscope.

2.2.1.d.ii) Electrically Suspended Gyros (ESG)

In 1954, Nordsieck [Nor96] introduced the first levitated gyroscope consisting of a sphere suspended by means of electrostatic levitation and spun by coils. In order to give to this sphere a principal inertial axis, two implementations were developed: Honeywell [Had84] placed a ring inside the sphere, whereas Rockwell placed a cylinder inside of it. The attitude of the sphere is then detected by optical sensors. Due to its drift performance below 0.0001°/h, Honeywell's solution has been integrated into nuclear submarines.

Due to a strong ratio force/size that electrical field allows, some implementations of ESG's have been developed in MEMS [Mur03] with a resolution of 0.05°/s for a disc shaped rotor of 4 [mm] in diameter.

2.2.1.d.iii) Magnetically Suspended Gyros (MSG)

The *Levitron* [Har83] is the first practical "implementation" of an MSG. It consists of a rotor placed over an arrangement of electromagnets, but is not used as a gyroscope but more as a demonstration toy which is described in [Fas08]. More seriously the use of magnetic suspension for gyroscopes has been introduced in a patent by Barrot et al. [Bol07]. Such devices are currently under development [Mar06] with promising results, but no industrial product is available for the moment. The miniaturization of the AMB gyroscope developed in the present thesis is a novelty compared with other work and a key factor for widening the use of gyroscopes to mass market applications.

2.2.2 Vibrating Gyroscopes

The first vibrating gyroscopes were realized during the 1960's and all relied on vibrating bodies used to provide torques from the Coriolis acceleration. Three different implementations of this theory will shortly be introduced in this section: the vibrating string gyro [Qui64], the tuning fork gyro [Hun64] and the vibrating shell gyro [Lyn84].

2.2.2.a The Vibrating String

The idea of the vibrating string was first proposed by Quick [Qui64], the principle is described in Fig.(2.7):

As shown on Fig.(2.7), a string is vibrated in the xz-plane with a sinusoidal velocity profile $v = v_0 \cos \omega_0 t$. If the gyroscope is exposed to an angular velocity Ω about the z axis, then because of the Coriolis acceleration ($2v\Omega$) the string begins to also vibrate in the y direction. Using the knowledge of the frequency ω_0 and the measurement along the y axis, one obtains the angular velocity Ω.

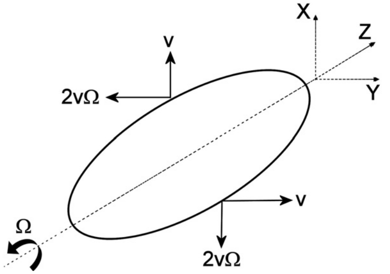

Figure 2.7: Effect of the Coriolis acceleration on a vibrating string. v is the instantaneous velocity of the string in the xz plane, and Ω describes the rotation speed that acts on the gyroscope.

2.2.2.b The Tuning Fork Gyro (TFG)

This idea was introduced by Hunt[Hun64] in 1964, but a realization with results satisfactory enough for its industrialization was firstly achieved at the Draper Lab [Wei93] in 1993.

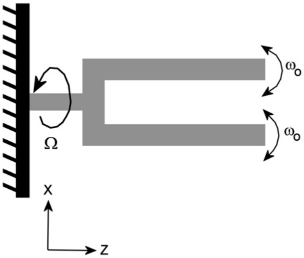

Figure 2.8: The tuning fork gyroscope. ω_0 describes the tine frequency, and Ω the vehicle angular velocity around the z axis.

As shown in Fig.(2.8), the tines of the fork oscillate in opposite phase at the frequency ω_0 within the xz plane. As an angular velocity Ω is applied about the z axis, the tines, due to the Coriolis acceleration, experience a movement not only within the xz plane but also along the y direction. The amplitude of the movement along the y axis is:

$$a = 4v_0 \cos(\omega_0 t)\,\Omega/K \tag{2.4}$$

In Eq.(2.4), v_0 describes the velocity amplitude of the tines and K the torsional stiffness constant of the stem.

2.2.2.c The Vibrating Cylinder Gyroscope

The vibrating cylinder gyroscope is based on an observation of Bryan [Bry90] that the rotation of a vibrating cylinder about its central axis induces a change in the position of its circumferential nodes relatively to the cylinder. This means that these nodes do not rotate at the same speed as the cylinder (see Fig.(2.9)), but at a rate proportional to the total turn. This phenomenon arises because of the Coriolis acceleration induced by the rotation.

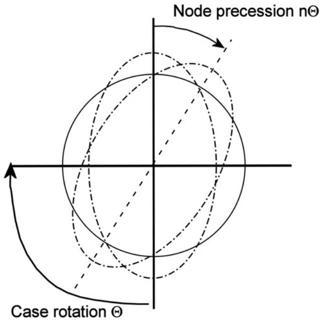

Figure 2.9: The vibrating cylinder gyroscope. n represents the percentage of the case rotation traveled by the vibrating node.

2.2.3 Optical Gyroscopes

This chapter consists of a brief description of the theoretical principles on which optical gyroscopes are based, as well as a short overview of some of the physical realizations of this theory.

2.2.3.a Sagnac Effect

All optical gyroscopes rely on the same theory: the Sagnac Effect [Sag13], which is an interference phenomenon. As shown in Fig.(2.10), two light beams of wavelength λ are emitted by the same light source/collector (S) in two opposite directions within an optical path of radius R, for example a glass fiber.

If the vehicle on which the gyroscope (consisting of the light source/receptor and of the optical path) is mounted starts turning with an instantaneous angular velocity Ω, then the arrival of the two light beams on the receptor will be shifted in time (see Eq.(2.5), in which the subscript + (resp. -) describes the positive (resp. negative) light beam):

$$\left.\begin{aligned} t_+ &= d_+/c = \tfrac{2\pi R + R\Omega t_+}{c} \\ t_- &= d_-/c = \tfrac{2\pi R - R\Omega t_-}{c} \end{aligned}\right\} \Rightarrow \Delta t = t_+ - t_- = \frac{4\pi R^2 \Omega}{c^2 - R^2\Omega^2} \approx \frac{4\pi R^2\Omega}{c^2}, \text{ as } c \gg R\Omega \tag{2.5}$$

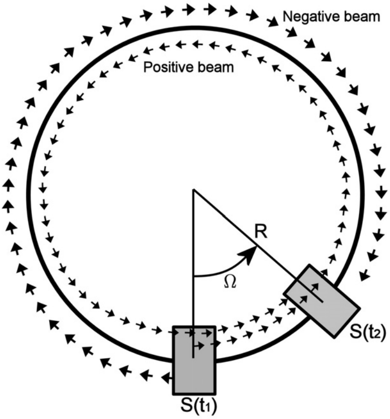

Figure 2.10: Illustration of the Sagnac Effect. S represents the light source, R the radius of the interferometer, and Ω describes the rotation speed of the object on which the gyroscope is mounted.

Thanks to the time delay between the two light beams, interference fringes appear with a phase shift Φ that is directly related to the vehicle instantaneous speed Ω (see Eq.(2.6)):

$$\underline{\text{Sagnac effect:}} \quad \Phi = 2\pi \frac{c}{\lambda} \Delta t = \frac{8\pi^2 R^2}{c\lambda} \Omega \tag{2.6}$$

2.2.3.b Types of Optical Gyroscopes

Four categories of optical gyroscopes exist: resonant or nonresonant and active or passive. Passive sensors use an external device to measure the Sagnac phase, whereas in active optical gyroscopes the phase causes a change in frequency that directly corresponds to the rotation speed.

The most widely used optical gyroscope is the active resonant ring laser gyroscope (RLG), but it could be supplanted by the Interferometric Fiber Optic Gyroscope (IFOG) which is based on the Sagnac interferometer. Two passive resonant gyroscopes, the Resonant Fiber Optic Gyroscope (RFOG) and the Micro Optic Gyro (MOG) show good performances and a very attractive cost and are therefore becoming more and more used [Law98].

2.3 Summary

A summary of typical performance characteristics for some of the previously introduced kinds of gyroscopes is given in table which is inspired from [Tit] concludes this brief review of the different existing types of gyroscopes and the theoretical principles on which they rely.

Characteristic	EGG	DTG	ESG	TFG	Vibratory cylinder	RLG	FOG
Bias [$°/h$]	0.05-10	0.05	NA	360-1800	360-1800	0.001-10	0.5-50
Linearity [%]	0.01-0.1	0.01-0.1	0.2	0.05-0.1	0.2-0.3	5-100	0.05-0.5
Maximum Input Rate [$°/s$]	>400	1000	200	600	>1000	>1000	>1000
Bandwidth [Hz]	60	100	10	100	500	>200	>100

Table 2.1: Typical performances of different types of gyroscopes.

Chapter 3

Active Magnetic Bearings

3.1 Definition

Magnetic bearings depict in a general manner the levitation of an object called the *rotor* (or *flotor* [Bar08]) by means of forces created by a magnetic actuators arrangement, the *stator*.

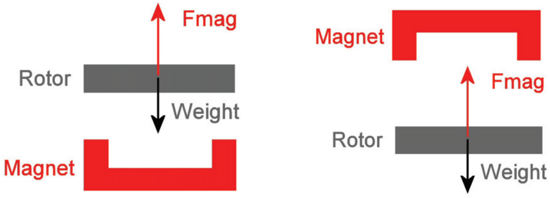

(a) (b)

Figure 3.1: Position of the rotor relatively to the magnet to have levitation at stand still without perturbation in the case of (a) a diamagnetic material and of (b) a ferromagnetic or paramagnetic material.

There exist two types of magnetic bearings: the *passive* (referred as PMB) and the *active* ones (referred as AMB). The classification is made by means of the achievable levitation which is directly linked to the relative permeability μ_r of the rotor material. If μ_r is higher (resp. lower) than 1 the material is called ferromagnetic (resp. diamagnetic). To illustrate the difference, we consider a bar placed near a magnet. The norm of the force exerted by the magnet on the bar increases as the bar gets closer to the magnet. On the opposite, the direction of the force is directly relied to μ_r: if $\mu_r > 1$ then the force is attractive (see Fig.(3.1(b))), otherwise it is reluctant see Fig.(3.1(a)).

In the case of a diamagnetic material, a perturbation of the rotor will lead to an increase or in a decrease of the distance between the rotor and the magnet, thus reducing or increasing the magnetic force strength. This will result in an attraction towards the stand still position of the rotor. Therefore diamagnetic levitation does not need any action of the environment to stabilize the rotor. On that purpose, diamagnetic levitation is called *passive*.

On the opposite, a slight deviation from the stand still position of a ferromagnetic or paramagnetic rotor towards the magnet (resp. away from the magnet) will lead in an increase (resp. a decrease) of the magnetic force strength, thus destabilizing the whole system. Hence, in the presence of a static field, such a system can not be stabilized. Therefore, a dynamic field depending on the distance can stabilize the system. Therefore, a controller that adapts the magnetic force in function of the distance between the rotor and the electromagnet is required, whence the name of *active* levitation.

Nowadays the existing diamagnetic material have a very small negative magnetic susceptibility χ. Therefore, the response of passive magnetic forces is too long to compensate for fast perturbations. On that purpose, for the time being passive magnetic forces are only used for the rotor levitation [Bar08]. Thus, passive magnetic levitation will not be considered in our application of magnetic bearings for a gyroscope. On the opposite, because of their high χ, ferromagnetic materials driven by active magnetic bearings can compensate for fast perturbations and therefore suit the requirement for gyroscopic sensing. On that purpose, this thesis will focus on active magnetic levitation of ferromagnetic materials.

3.2 AMB: Interest and Applications

The interest for AMB relies on the following advantages:

- no contact.
- no lubrication needed.
- no contamination by the dust created by friction between the rotor and the stator.
- viscous friction can be avoided if the rotor is confined in high vacuum.
- low vibration level.

- dynamics adaptable to the desired application by tuning of the control loop.
- precise positioning of the rotor due to the control loop.
- achievable fast positioning and/or high rotational speed of the rotor.

Nowadays, AMB are mainly used to replace the conventional ball bearings for turbomolecular pumps, high speed motors, flywheels, turbo compressors, vacuum pumps, grinding and milling spindles [AG08], friction spindles for textile industry[Mos06] and motors for hard disk drives [Zoe02]. Another application that can also be seen as the replacement of ball bearings is the substitution of wheels in the case of magnetically levitated trains [RTR08], [Sie08].

Recently, AMB have started to being used as inertial sensors. Accelerometers and inclinometers have been developed [Bar08]. The idea of adapting actively levitated motors as gyroscopes has been introduced in [Bol05] and [Bol07]. Maruyama et al. [Mar06] experimentally succeeded to use an industrial AMB motor as gyroscope. However, due to its size, this AMB based gyroscope is not yet suited for implementation on common vehicles as cars among others. Thus, the small size (a cube of 40[mm] ridge length) of the AMB gyroscope developed in this thesis is a key factor for a possible commercialization into the mass market.

Part II

1^{st} Gyroscopic Sensing Method: Ball Orbit Observation

Chapter 4

Ball Orbit Observation

4.1 Description of the Measurement Principle

A new way to measure the angular velocity is proposed in the current part. One makes a ball[1] shaped rotor describe a circular orbit[2] of 200[μm] in diameter in the XY-plane (see Fig.(4.1(a))). This trajectory may be seen as a disc with a normal vector $\overrightarrow{N}$. At this time the angle between $\overrightarrow{Z}$ and $\overrightarrow{N}$ is zero.

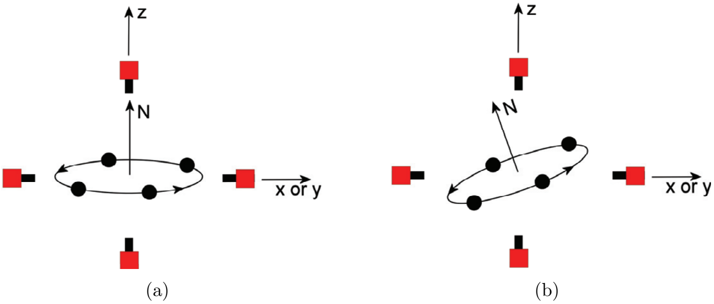

(a) (b)

Figure 4.1: Orbit of the ball: (a) in the presence (resp. (b) in the absence) of external movement. The ball shaped rotor is represented in black and the stator actuators as red and black squares. The vector $\vec{N}$ is the vector normal to the ball orbit.

---

[1] The chosen rotor shape is a ball because it is the easiest one to control in position, what is sufficient for this measurement method.

[2] An analog method with the ball following a segment along the Z-axis instead of an orbit has been tested but with less success.

When the stator (the set of actuators) is moved, the disc described by the ball will not follow the basis movement instantaneously (see Fig.(4.1(b))). Due to this latency an angle between $\overrightarrow{N}$ and $\overrightarrow{Z}$ will appear. The algorithm to compute this angle is presented in the following section.

4.2 Computation of the Angular Velocity

4.2.1 Computation of the Disc Normal Vector Coordinates

Fig.(4.2) is a top view of the orbit described by the rotor and will be used to explain the measurement of the vector normal to the disc.

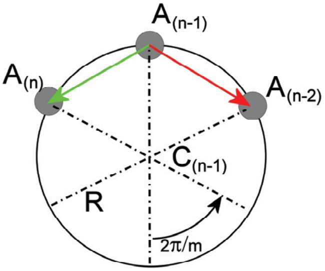

Figure 4.2: Top view of the orbit described by the ball shaped rotor. $A_{(n)}$ (resp. $C_{(n)}$) represents the ball position (resp. the orbit center) at the time $t_{(n)}$. m is the number of ball position measurements per revolution.

$A_{(n)}$ and $C_{(n)}$ are respectively the position of the ball and the position of the orbit center at the time $t_{(n)}$. Eq.(4.1) presents how the vector $\overrightarrow{N}_{(n-1)}$ (i.e. $\overrightarrow{N}$ at the time $t_{(n-1)}$) is computed:

$$\overrightarrow{N}_{(n-1)} = \frac{\overrightarrow{A_{(n-1)}A_{(n)}} \times \overrightarrow{A_{(n-1)}A_{(n-2)}}}{\|\overrightarrow{A_{(n-1)}A_{(n)}}\| \cdot \|\overrightarrow{A_{(n-1)}A_{(n-2)}}\|} \tag{4.1}$$

4.2.2 Computation of the Angle between the Normal Vector and the Z-axis

From the measurement of the coordinates of the normal vector $\overrightarrow{N}_{(n-1)}$, the relative angles (ϕ_x, ϕ_y) between the vectors $\overrightarrow{N}_{(n-1)}$ and $\vec{Z}$ can be computed using the definition of the Euler angles (see Eq.(2.1)):

$$\overrightarrow{N}_{(n-1)} = \begin{bmatrix} \cos(\phi_x) \cdot \sin(\phi_y) \\ -\sin(\phi_x) \\ \cos(\phi_x) \cdot \cos(\phi_y) \end{bmatrix} \tag{4.2}$$

4.2.3 Computation of the Angular Velocity

The angular velocity corresponding to the angle ϕ_x, resp. ϕ_y, will be noted $\dot{\phi}_x$, resp. $\dot{\phi}_y$. The total angle ϕ_x (this is analog for ϕ_y) described by the gyroscope from the beginning of the experiment (time $t = 0$) to the current time t is given by Eq.(4.3):

$$\phi_x(t) - \phi_x(0) = \int_0^t \dot{\phi}_x(t) \cdot dt \tag{4.3}$$

The digital form of Eq.(4.3), with T_s as sampling time, permits to compute the angular velocity $\dot{\phi}_x$ at time $k \cdot T_s$:

$$\begin{aligned} & \phi_x(k \cdot T_s) - \phi_x(0) = \sum_{i=1}^{k} \dot{\phi}_x(i \cdot T_s) \cdot T_s \\ & \Rightarrow \dot{\phi}_x(k) = \tfrac{1}{T_s}\left(\phi_x(k) - \phi_x(0)\right) - \sum_{i=1}^{k-1} \dot{\phi}_x(i) = \frac{\phi_x(k)}{T_s} - S_{k-1}, \\ & \text{with} \quad S_{k-1} = \tfrac{\phi_x(0)}{T_s} + \sum_{i=1}^{k-1} \dot{\phi}_x(i) \end{aligned} \tag{4.4}$$

Chapter 5

Prototype Design and Control

In this chapter, the rotor levitated by the active magnetic bearings can be designated by the terms "rotor" or "ball". This possible change in terminology has no influence.

5.1 Prototype Design

As presented in §4, the ball shaped rotor only needs to be controlled in position, what can be fulfilled by three pairs of actuators. On that purpose, a prototype inspired from the one used by [Bol05] has been developed. Further precisions about the sensing system can be found in [Bol05].

The prototype developed in this thesis is presented in Fig.(5.1).

5.2 Prototype Model

5.2.1 Force calculation

5.2.1.a General Expression of the Force

According to [Bol05], the magnetic force applied on the ball shaped rotor by an electromagnetic actuator is given by :

$$F(u,i) = \frac{1}{2} \cdot \frac{\partial L(u)}{\partial u} \cdot i^2 \tag{5.1}$$

$$\text{with} \begin{cases} L: & \text{the inductance of the actuator coil} \\ u: & \text{the air gap between the actuator and the ball} \\ i: & \text{the current flowing in the actuator coil} \end{cases}$$

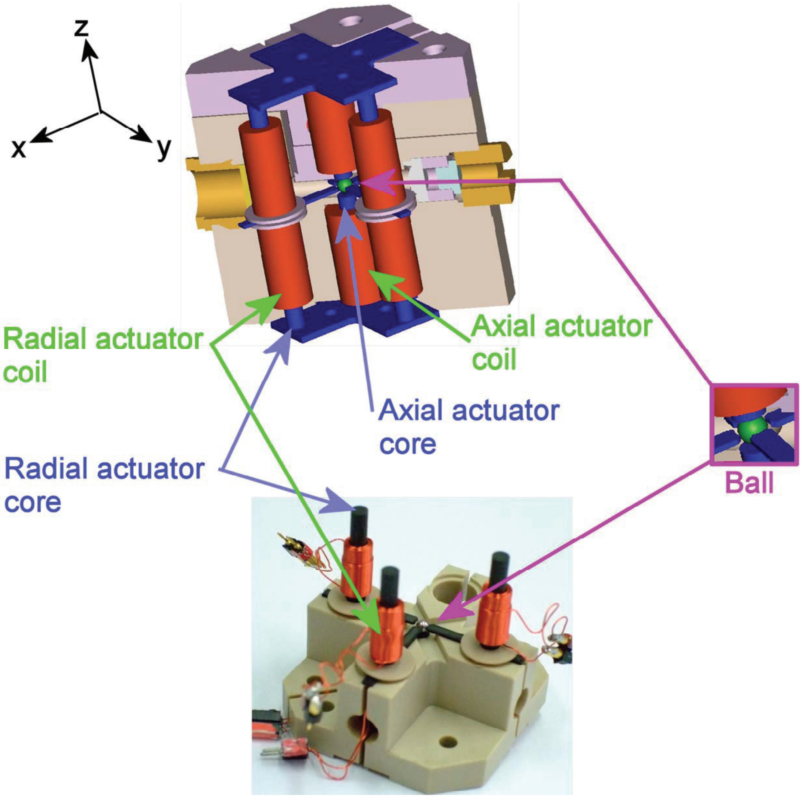
z
x
y
Radial actuator coil
Axial actuator coil
Axial actuator core
Radial actuator core
Ball

Figure 5.1: Exploded view of the prototype. The ball shaped rotor is represented in green, the electromagnetic actuator coils in red and their cores in blue.

[Bol05] proposes Eq.(5.2) as linearized expression of the coil inductance:

$$L(u) = L_0 + \frac{\Delta L}{1 + a \cdot u} \tag{5.2}$$

$$\text{with} \begin{cases} L_0 : & \text{the inductance of the coil without the rotor} \\ \Delta L : & \text{the maximum variation of the coil inductance} \\ a : & \text{constant} \end{cases}$$

With the help of Eq.(5.1) and Eq.(5.2), the linearized expression of the force exerted by the actuator on the ball is:

$$F\left(u,i\right)=-\frac{1}{2}\frac{\Delta L\cdot a}{\left(1+a\cdot u\right)^{2}}\cdot i^{2} \tag{5.3}$$

For the present prototype, [Bol05] proposes Eq.(5.4) as expression for the air gap u between the actuator and the ball. In this equation, d (resp. r) represents the axial (resp. radial) distance between the actuator and the ball center (see Fig.(5.6)), and r_{ball} the ball radius.

$$u=\sqrt{r^2+d^2}-\frac{\pi}{4}r_{ball} \tag{5.4}$$

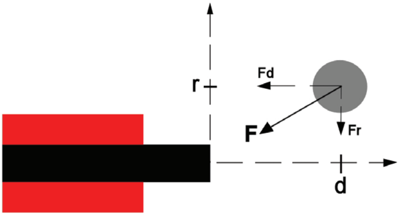

Figure 5.2: Schematic representation of the magnetic force exerted by the ferrite/coil actuator onto the ball.

The general form of the force becomes with the help of Eq.(5.3) and Eq.(5.4):

$$\overrightarrow{F}=\begin{cases} F_r=F\left(u,i\right)\cdot\frac{r}{\sqrt{r^2+d^2}} \\ F_d=F\left(u,i\right)\cdot\frac{d}{\sqrt{r^2+d^2}} \end{cases} \tag{5.5}$$

5.2.1.b Linearization of the Force

The electromagnetic actuators have been dimensioned so that the electromagnetic force exerted by an actuator placed over the ball must exactly compensate for its weight $m\cdot g$. Therefore, at the the nominal air gap u_0 (i.e half the distance between two opposed actuators), the nominal current i_0 flowing through the actuator is given by:

$$i_0=\left[1+a\cdot u_0\right]\cdot\sqrt{\frac{2\cdot m\cdot g}{a\cdot\Delta L}} \tag{5.6}$$

Therefore the linearization of Eq.(5.3) around $u=u_0$ (i.e. $r=0$ and $d=d_0$) and $i=i_0$ returns:

$$
\begin{aligned}
F(r,\Delta d,\Delta i) &= F(u_0,i_0) + \left.\tfrac{\partial F}{\partial r}\right|_{(u_0,i_0)} \cdot r + \left.\tfrac{\partial F}{\partial(\Delta d)}\right|_{(u_0,i_0)} \cdot \Delta d + \left.\tfrac{\partial F}{\partial i}\right|_{(u_0,i_0)} \cdot \Delta i \\
&= -\tfrac{1}{2}\tfrac{\Delta L\cdot a\cdot i_0^2}{(1+a\cdot u_0)^2} + \tfrac{\Delta L\cdot a^2\cdot i_0^2}{(1+a\cdot u_0)^3}\Delta d - \tfrac{\Delta L\cdot a\cdot i_0}{(1+a\cdot u_0)^2}\Delta i \\
\text{with} &\left\{\begin{array}{rl} \Delta d: & \text{the position deviation from the nominal distance } d_0 \\ \Delta i: & \text{the current deviation from the nominal current } i_0 \end{array}\right.
\end{aligned}
\tag{5.7}
$$

5.2.1.c Global Magnetic Force

In this section, we will use the following designations for the forces created by two electromagnetic actuators placed on each of the rotor and placed on a same axis of the stator:

- F_m designates the force by the actuator placed on the negative part of the axis.
- F_p designates the force by the actuator placed on the positive part of the axis.

5.2.1.c.i) Expression of the force F_m

$$
\overrightarrow{F_m}(r,\Delta d,\Delta i_m) = \frac{1}{d_0}F_m(r,\Delta d,\Delta i_m)\cdot\begin{bmatrix} r \\ d_0+\Delta d \end{bmatrix} \tag{5.8}
$$

with Δi_m the deviation of the nominal current for the negative actuator.

5.2.1.c.ii) Expression of the force F_p

$$
\overrightarrow{F_p}(r,\Delta d,\Delta i_p) = \frac{1}{d_0}F_p(r,\Delta d,\Delta i_p)\cdot\begin{bmatrix} -r \\ d_0-\Delta d \end{bmatrix} \tag{5.9}
$$

with Δi_p the deviation of the nominal current for the positive actuator.

5.2.1.c.iii) Calculation of the resulting force $F = F_p + F_m$

With the help of Eq.(5.8) and Eq.(5.9), the resulting electromagnetic force exerted on the ball shaped rotor is given by:

$$\begin{aligned}\vec{F} &= \vec{F_m}\left(r,\Delta d,\Delta i_m\right)+\vec{F_p}\left(r,\Delta d,\Delta i_p\right)\\ &= \tfrac{\Delta L\cdot a\cdot i_0^2}{(1+a\cdot u_0)^2}\begin{bmatrix}-\left(1+\frac{\Delta i_m+\Delta i_p}{i_0}\right)\cdot\frac{r}{d_0}\\ \\ \left(\frac{2\cdot a}{1+a\cdot u_0}\cdot\Delta d+\frac{\Delta i_p-\Delta i_m}{i_0}\right)-\left(1+\frac{\Delta i_m+\Delta i_p}{i_0}\right)\cdot\frac{\Delta d}{d_0}\end{bmatrix}\end{aligned} \tag{5.10}$$

We consider that the ball shaped rotor is only subject to small displacement from its nominal position, i.e. that $r \ll d_0$ and $\Delta d \ll d_0$. With this assumption Eq.(5.10) becomes:

$$\begin{aligned}\vec{F} &= \vec{F_m}\left(r,\Delta d,\Delta i_m\right)+\vec{F_p}\left(r,\Delta d,\Delta i_p\right)\\ &= \tfrac{\Delta L\cdot a\cdot i_0^2}{(1+a\cdot u_0)^2}\begin{bmatrix}0\\ \\ \frac{2\cdot a}{1+a\cdot u_0}\cdot\Delta d+\frac{\Delta i_p-\Delta i_m}{i_0}\end{bmatrix}=\begin{bmatrix}0\\ \\ k_d\cdot\Delta d+k_i\cdot\Delta i\end{bmatrix}\\ &\text{with } \Delta i=\frac{1}{2}\left(\Delta i_p-\Delta i_m\right)=\frac{1}{2}\left[\left(\Delta i-i_0\right)-\left(-\Delta i-i_0\right)\right]\end{aligned} \tag{5.11}$$

Thus, Eq.(5.11) confirms that the electromagnetic force exerted on the ball shaped rotor along one axis can be assumed to be directed along the considered axis and that it only depends from the position deviation along that axis and from the current flowing within the actuator coils.

5.2.2 Transfer Function of the Electromagnetic Force

As the behaviors of the ball movement along the three stator directions x,y,z are governed by Eq.(5.11), the term Δd of this equation will be replaced by z (it could be x or y as well) in the following developments and Δi by i_z.

Introduction the force exerted by the electromagnetic actuators onto the ball shaped rotor (see Eq.(5.11)) into the second Newton law of motion returns:

$$m\cdot\frac{d^2z}{dt^2}=k_d\cdot\Delta z+k_i\cdot i_z \tag{5.12}$$

The previous equation leads to the following transfer function in the Laplace domain:

$$G_{i_z\rightarrow z}=\frac{Z}{I_z}=\frac{k_i}{m\cdot s^2-k_d} \tag{5.13}$$

Eq.(5.13) shows a placement of the poles of the system transfer function on the imaginary axis. This means that the plant is intrinsically unstable and that it requires a controller to be stabilized.

5.3 Prototype Control

5.3.1 PID Control

To stabilize the model, a closed-loop controller is needed to shift the transfer function poles (see equation 5.13) to the left half-plane. A PID controller is introduced in order to inject a current i_z related to the ball displacement into the electromagnetic actuators, Eq.(5.12) becomes:

$$m \cdot \ddot{z} = k_d \cdot z + k_i \cdot i = k_d \cdot z + k_i \cdot K \left(1 + T_d \cdot \frac{d}{dt} + \frac{1}{T_i} \cdot \int_t \right) \cdot (-z) \tag{5.14}$$

$$\text{with} \begin{cases} K: & \text{the proportional term of the PID controller} \\ T_i: & \text{the integrative term of the PID controller} \\ T_d: & \text{the derivative term of the PID controller} \end{cases}$$

Hence, the plant transfer function integrating the controller (see Fig.(5.6)) in the Laplace domain becomes:

$$GC = G_{i \to z} C_{z \to i} = \frac{Z}{Z_0} = \frac{k_i K T_d}{m} \cdot \frac{s^2 + \frac{1}{T_d} \cdot s + \frac{1}{T_i T_d}}{s^3 + \frac{k_i K T_d}{m} \cdot s^2 + \frac{k_i K - k_d}{m} \cdot s + \frac{k_i K}{m T_i}} \tag{5.15}$$

$$\text{with} \begin{cases} Z_0: & \text{the reference position of the ball shaped rotor} \\ C_{z \to i}: & \text{the transfer function of the PID controller} \end{cases}$$

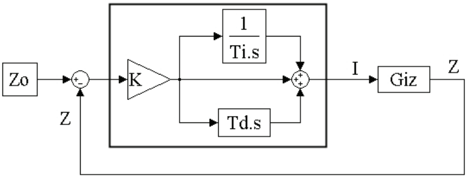

Figure 5.3: Block diagram representation of the controller/plant system. The controller is represented within the square.

5.3.1.a Stability Condition: Routh Criterion

The Routh Criterion [Rou77] is used to stabilize the GC transfer function. This criteria tells that the poles of the GC transfer function are placed in the left half-plane if and only if the following conditions are fulfilled:

$$\begin{aligned} \tfrac{k_iK-k_z}{m} &> 0 \\ \frac{\frac{k_iKT_d}{m}\cdot\left(\frac{k_iK-k_z}{m}\right)-\frac{k_iK}{mT_i}}{\frac{k_iKT_d}{m}} &= \tfrac{k_iK-k_z}{m}-\tfrac{1}{T_iT_d}>0 \\ \tfrac{k_iK}{mT_i} &> 0 \end{aligned} \tag{5.16}$$

5.3.1.b Specifications in Time Domain

The denominator in Eq.(5.15) is of 3^{rd} degree, therefore it has one purely real root and two imaginary roots. Hence, the denominator can be rewritten as:

$$D(s) = (s-p_r)\cdot\left(s^2+2\cdot\xi\cdot\omega_n\cdot s+\omega_n^2\right) \tag{5.17}$$

$$\text{with}\begin{cases} p_r: & \text{the real root of D(s)} \\ \xi: & \text{a constant called damping factor} \\ \omega_n: & \text{the natural frequency of D(s)} \end{cases}$$

Time domain specifications (rise time, overshoot and settling time) will be used to determine ξ and w_n. According to [Fra94], the time domain specifications and the constants presented in Eq.(5.17) are bound by the following relationships:

$$\begin{array}{ll} \text{rise time:} & t_r \simeq \frac{1.8}{\omega_n} \\ \text{overshoot:} & M_p = e^{-\frac{\pi\xi}{\sqrt{1-\xi^2}}} \\ \text{settling time:} & t_s \simeq \frac{4.6}{\xi\omega_n} \end{array} \tag{5.18}$$

To get an overshoot $M_p \simeq 5\%$, the damping factor will be chosen as $\xi = 0.7$.

We will choose the settling time $t_s = 3T_s$, with T_s = sampling time. Thus $\omega_n \simeq \frac{2.19}{T_s}$.

Finally, the controller parameters K, T_d and T_i, can be identified using the time specifications (with $p_r = -\alpha\cdot\omega_n$ and $\alpha > 0$) .

$$\begin{aligned} K &= \tfrac{1}{k_i}\cdot\left[m\omega_n^2\cdot(1+2\xi\alpha)+k_z\right] \\ T_d &= \tfrac{m}{k_iK}\cdot(2\xi+\alpha)\,\omega_n \\ T_i &= \tfrac{k_iK}{m\alpha\omega_n^3} \end{aligned} \tag{5.19}$$

5.3.2 Electronics Transfer Function

As the computer DA card can not deliver any current but only voltages, a voltage to current converter is needed at the output of the DA card.

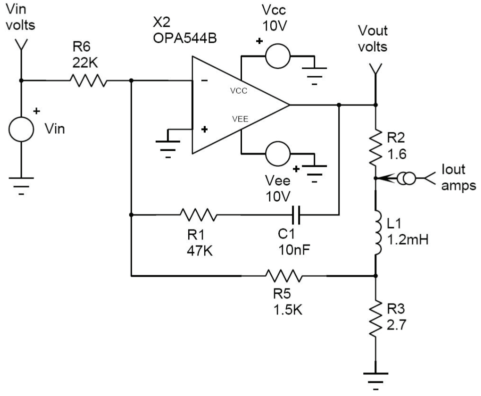

Figure 5.4: Schematics of the coil command electronics.

The transfer function of the coil command electronics is:

$$\begin{aligned} G_{elec}(s) &= \frac{i_{out}}{V_{in}} \\ &= -\frac{R_3+R_5}{R_3R_6} \cdot \frac{1+R_1Cs}{1+(R_1+R_2+R_2R_5/R_3+R_5)Cs+LC(1+R_5/R_3)s^2} \end{aligned} \tag{5.20}$$

The command electronics has a gain of $-25[mA \cdot V^{-1}]$ and a bandwidth of $5kHz$.

As the DA card can only deliver a voltage in the domain [-5V; 5V], a saturation must be included at the output of the controller. Thus the global plant system including the DA card and the coil command electronics becomes:

5.3.2..i) Introduction of an Antiwindup Feedback Structure

When the voltage V$_{sat}$ (see Fig.(5.5)) does not belong to the linear domain of the saturation block, V$_d$ may become very high because of an excessive buildup of the integral action, whenever $Z_0 - Z$ is large and V_d exceeds its saturation values. This phenomenon, known as "reset windup" leads to a loss in the control quality resulting in an overshoot of Z [Fra94].

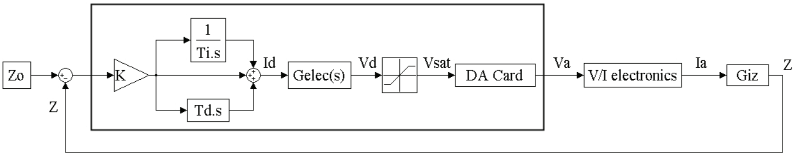

Figure 5.5: Block diagram representation of the controller/plant system with the DA card and the coil command electronics. The subscript "d" means digital, "sat" saturated and "a" analog.

To alleviate this reset windup effect, the basic idea is to monitor the difference e_a of the input and output signal to the saturation block. It is zero within the linear operating range, and nonzero outside, where the integral action would "wind up". Then feedback of $e_a = V_{sat} - V_d$ is used to keep the integral action from running too far off [Gla02].

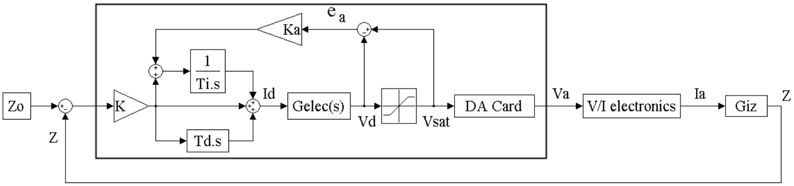

Figure 5.6: Block diagram representation of the controller/plant system including the antiwindup feedback structure.

5.3.3 Adaptive Control

5.3.3.a Adaptive Control Choice

The basic idea of adaptive control is to deal with complex systems that have unpredictable parameter deviations and uncertainties. This uncertainty has many origins as an insufficient knowledge of the system, linearization of the system, time-varying system parameters... This lack of knowledge about the system can lead to inaccuracy and/or to instability. Therefore, to get rid off this uncertainty, the controller should be able to be redesigned on-line to maintain consistent performance of the system.

Adaptive control is divided into two families that will be presented in the following sections:

1. Model-reference adaptive controllers (MRAC)
2. Self-tuning controllers (STC)

5.3.3.a.i) Model-reference adaptive controllers

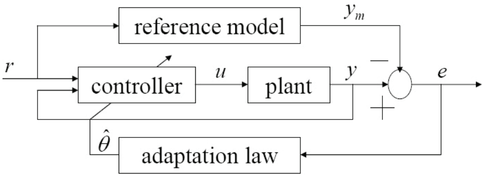
reference model
y_m
r
controller
u
plant
y
—
e
+
$\hat{\theta}$
adaptation law

Figure 5.7: General representation of MRACs.

MRACs are composed of four main blocks as shown on Fig.(5.7):

- The plant to be controller whose structure is known but not its parameters.
- The reference model specifies the ideal response y_m of the adaptive control to the external command r imposed by the user.
- The adaption law is used to adjust the controller parameters to the actual and current plant parameters.
- The controller is parameterized by a number of adjustable parameters and provides perfect tracking capacity.

5.3.3.a.ii) Self-tuning controllers

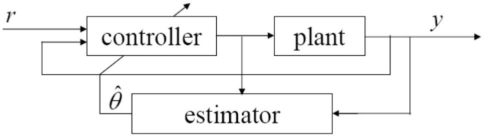
r
controller
plant
y
$\hat{\theta}$
estimator

Figure 5.8: General representation of STCs.

As shown on fig.(5.8), STCs combine a controller with an on-line (recursive) plant parameter estimator. The estimator is a process that finds a set of parameters that fits the available input-output data from a plant.

5.3.3.a.iii) MRAC choice

As written in [Slo91], STCs are more flexible than MRACs because of the separation of control and estimation which leads to the possible coupling of different controllers with various estimators. However, the stability and convergence of STCs are generally difficult to ensure if the reference signal is not very rich (a constant for example). In opposite, MRACs guarantee stability and convergence whatever the signal richness. In our case, the ball position is a constant and therefore the choice of the MRAC.

5.3.3.b Design of the adaptive controller

5.3.3.b.i) The Reference Model

Along this section, we will use for the action of the electromagnetic actuators on the ball shaped rotor the model proposed in Eq.(5.12).
Adaptive control requires a *strictly positive real*(SPR) plant to work [Slo91]. To achieve this requirement, the reference plant will consist in the electromagnetic actuators plus the PID controller presented in Eq.(5.15) whose parameters have been defined according to Eq.(5.19).

From now on, the transfer function that will be used for the reference model is the following one:

$$W_m(s) = \frac{k_m \cdot (s^2 + b_{m1} \cdot s + b_{m2})}{s^3 + a_{m1} \cdot s^2 + a_{m2} \cdot s + a_{m3}} \tag{5.21}$$

The reference model parameters b_m and a_m presented in Eq.(5.21) are fully known.

5.3.3.b.ii) The Real Plant

As written in the previous section, the transfer function of the plant includes a PID controller in order to have a SPR system. The plant will be *a priori* considered to be linear with the same order as the reference model:

$$W_m(s) = \frac{k_p \cdot (s^2 + b_{p1} \cdot s + b_{p2})}{s^3 + a_{p1} \cdot s^2 + a_{p2} \cdot s + a_{p3}} \tag{5.22}$$

The plant parameters b_p and a_p presented in Eq.(5.22) are uncertain.

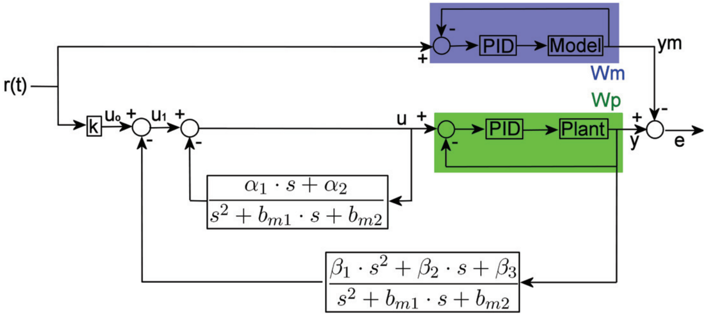
r(t)
k
u₀
u₁
u
+
-
PID
Model
ym
Wm
Wp
PID
Plant
y
e
$\frac{\alpha_1 \cdot s + \alpha_2}{s^2 + b_{m1} \cdot s + b_{m2}}$
$\frac{\beta_1 \cdot s^2 + \beta_2 \cdot s + \beta_3}{s^2 + b_{m1} \cdot s + b_{m2}}$

Figure 5.9: Implementation of the MRAC to the AMB-Gyroscope. The blue and green rectangles respectively represent the reference model and the plant

5.3.3.b.iii) MRAC implementation to the AMB system

One of the goal of adaptive control is to fit the plant behavior to the perfectly known behavior of the reference model. On that purpose, two closed loop blocks (these are represented in white in Fig.(5.9)) are added to the plant. With these blocks the relation between the reference signal $r(t)$ and the plant output y becomes:

$$\begin{aligned} y &= W_p \cdot u = W_p \cdot \tfrac{s^2+b_{m1}\cdot s+b_{m2}}{s^2+(b_{m1}+\alpha_1)\cdot s+(b_{m2}+\alpha_2)} \cdot u_1 \\ &= W_p \cdot \tfrac{s^2+b_{m1}\cdot s+b_{m2}}{s^2+(b_{m1}+\alpha_1)\cdot s+(b_{m2}+\alpha_2)} \cdot \left[k \cdot r - \tfrac{\beta_1\cdot s^2+\beta_2\cdot s+\beta_3}{s^2+b_{m1}\cdot s+b_{m2}} \cdot y\right] \\ &= \tfrac{k_p\cdot\left(s^2+b_{p1}\cdot s+b_2\right)}{s^3+a_{p1}\cdot s^2+a_{p2}\cdot s+a_{p1}} \cdot \tfrac{k\left(s^2+b_{m1}\cdot s+b_{m2}\right)\cdot r-\left(\beta_1\cdot s^2+\beta_2\cdot s+\beta_3\right)\cdot y}{s^2+(b_{m1}+\alpha_1)\cdot s+(b_{m2}+\alpha_2)} \end{aligned} \tag{5.23}$$

Choosing $b_{m1} + \alpha_1 = b_{p1}$ and $b_{m2} + \alpha_2 = b_{p2}$, Eq.(5.23) becomes:

$$y = \tfrac{k_p\cdot\left[k\left(s^2+b_{m1}\cdot s+b_{m2}\right)\cdot r-\left(\beta_1\cdot s^2+\beta_2\cdot s+\beta_3\right)\cdot y\right]}{s^3+a_{p1}\cdot s^2+a_{p2}\cdot s+a_{p1}}$$

$$\Rightarrow W_{ry} = \tfrac{y}{r} = \tfrac{k_p\cdot k\cdot\left(s^2+b_{m1}\cdot s+b_{m2}\right)}{s^3+(a_{p1}+\beta_1)\cdot s^2+(a_{p2}+\beta_2)\cdot s+(a_{p3}+\beta_3)} \tag{5.24}$$

The following set of choices permits to get $W_{ry} = W_m$ and thus to achieve perfect tracking:

$$\begin{gathered} k = \tfrac{k_m}{k_p} \\ \beta_1 = a_{m1} - a_{p1} \\ \beta_2 = a_{m2} - a_{p2} \\ \beta_3 = a_{m3} - a_{p3} \end{gathered}$$

As the plant parameters (the terms b_p and a_p in Eq.(5.22)), are not known, the adaption law must modify the coefficient α_i and β_i according to the variations of the plant parameters. On that purpose an adaption law will be introduced (see Fig.(5.10)):

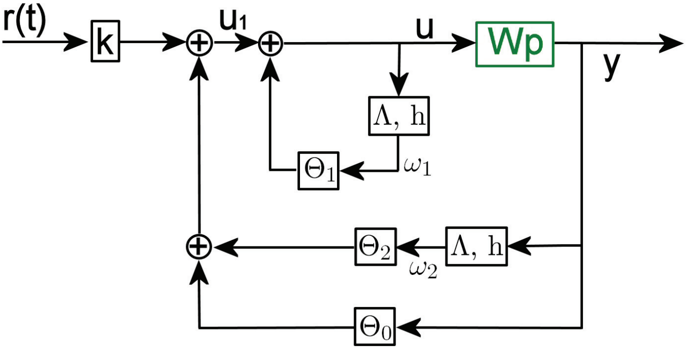

Figure 5.10: Introduction of the control law in the MRAC.

From Fig.(5.10), the plant input u can be written as:

$$u = \overrightarrow{\Theta_1}^T(t) \cdot \overrightarrow{\omega_1} + \overrightarrow{\Theta_2}^T(t) \cdot \overrightarrow{\omega_2} + \Theta_0(t) \cdot y + k(t) \cdot r \tag{5.25}$$

The vectors ω_i introduced in Eq.(5.25) are defined as follow:

$$\begin{aligned} \overrightarrow{\omega_i}^T &= [\omega_i \quad \dot{\omega}_i] \\ \dot{\overrightarrow{\omega_1}} &= \Lambda \cdot \overrightarrow{\omega_1} + h \cdot u \\ \dot{\overrightarrow{\omega_2}} &= \Lambda \cdot \overrightarrow{\omega_2} + h \cdot y \end{aligned} \tag{5.26}$$

The expression of the matrices Λ and h are given by:

$$\Lambda = \begin{bmatrix} 0 & 1 \\ -b_{m2} & -bm1 \end{bmatrix} \text{ and } h = \begin{bmatrix} 0 \\ 1 \end{bmatrix} \tag{5.27}$$

The introduction of Eq.(5.27) into Eq.(5.26) returns:

$$\overrightarrow{\omega_1} = \frac{1}{Z_m} \cdot \begin{bmatrix} s + b_{m1} & 1 \\ b_{m2} & s \end{bmatrix} \cdot \begin{bmatrix} 0 \\ 1 \end{bmatrix} \cdot u = \frac{1}{Z_m} \cdot \begin{bmatrix} 1 \\ s \end{bmatrix} \cdot u$$

$$\overrightarrow{\omega_2} = \frac{1}{Z_m} \cdot \begin{bmatrix} s + b_{m1} & 1 \\ b_{m2} & s \end{bmatrix} \cdot \begin{bmatrix} 0 \\ 1 \end{bmatrix} \cdot y = \frac{1}{Z_m} \cdot \begin{bmatrix} 1 \\ s \end{bmatrix} \cdot y \qquad (5.28)$$

$$\text{with } Z_m = s^2 + b_{m1} \cdot s + b_{m2}$$

The expressions of the terms ω_i's (see Eq.(5.28)) permit to find the vectors Θ_i presented Eq.(5.25):

$$\begin{aligned} \overrightarrow{\Theta_1}^T &= -\begin{bmatrix} \alpha_2 \\ \alpha_1 \end{bmatrix} \\ \overrightarrow{\Theta_2}^T &= -\begin{bmatrix} \beta_3 - \beta_1 \cdot b_{m2} \\ \beta_2 - \beta_1 \cdot b_{m1} \end{bmatrix} \\ \Theta_0 &= -\beta_1 \end{aligned}$$

5.3.3.b.iv) Choice of the adaption law

For conciseness reasons, the following notations for the control law will be used for now on:

$$u = \overrightarrow{\Theta}^T(t) \cdot \overrightarrow{\omega} \qquad (5.29)$$

with

$$\begin{aligned} \overrightarrow{\Theta}^T &= \begin{bmatrix} k(t) & \overrightarrow{\Theta_1}^T(t) & \overrightarrow{\Theta_2}^T(t) & \Theta_0(t) \end{bmatrix} \\ \overrightarrow{\omega}^T &= \begin{bmatrix} r(t) & \overrightarrow{\omega_1}^T(t) & \overrightarrow{\omega_2}^T(t) & y(t) \end{bmatrix} \end{aligned}$$

Eq.(5.29) can be rewritten as:

$$u = \overrightarrow{\Theta^\star}^T \cdot \overrightarrow{\omega} + \overrightarrow{\Phi}^T(t) \cdot \overrightarrow{\omega} \qquad (5.30)$$

$$\text{with } \begin{cases} \overrightarrow{\Theta^\star}\text{: the ideal value of } \overrightarrow{\Theta} \\ \overrightarrow{\Phi} = \overrightarrow{\Theta} - \overrightarrow{\Theta^\star}\text{: the error between } \overrightarrow{\Theta} \text{ and } \overrightarrow{\Theta^\star} \end{cases}$$

According to Fig.(5.9) and (5.10) the error *e(t)* between the plant output *y(t)* and the reference output y_m*(t)* becomes:

$$\begin{aligned} e(t) &= y(t) - y_m(t) = W_m \cdot u - W_m \cdot r \\ &= W_m \cdot \left[\overrightarrow{\Theta^\star}^T \cdot \overrightarrow{\omega} + \overrightarrow{\Phi}^T(t) \cdot \overrightarrow{\omega} / k^\star \right] - W_m \cdot r \\ &= W_m \cdot \overrightarrow{\Phi}^T(t) \cdot \overrightarrow{\omega} / k^\star \end{aligned} \qquad (5.31)$$

Applying Barbalat's lemma (see [Kha92]) to Eq.(5.31), the following control law is chosen:

$$\dot{\overrightarrow{\Theta}} = -sgn(k_p) \cdot \gamma \cdot e(t) \cdot \overrightarrow{\omega} \qquad (5.32)$$

In Eq.(5.32), the term γ is a positive number representing the adaption gain. As the output signal y is bounded, Barbalat's lemma shows that the tracking error in this adaptive control system asymptotically converges.

Chapter 6

Experimental Results for the Ball Orbit Measurement Method

Two types of experiments are presented in this chapter in order to characterize the specifications of the AMB based gyroscope regarding the angular velocity measurement. The angular velocity has been first measured while the vehicle is moving, and, in a second time, when the vehicle is at stand still. This last measurement permits to determine the noise of the AMB based gyroscope sensor.

The measurements of the angular velocity about the X and Y axes have returned the same results , therefore, only the results for the X axis will be presented in this chapter.

6.1 Test Rig

The experiments are performed with the help of a rotary table designed during this thesis. This rotary table is based on the pantoscope principle described by [Bau97]. The AMB based gyroscope is mounted on the upper side of the rotary table (see Fig.(6.1(a))), and the reference gyroscope (the inertial measurement unit IMU700CB-200 of Crossbow [Inc08]) on the lower side of the rotary table (see Fig.(6.1(b))). Thus, both gyroscopes are subject to the same angular velocity.

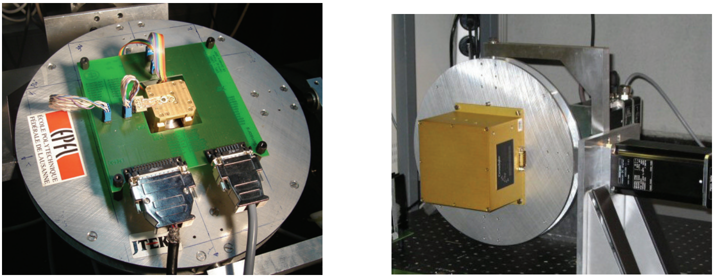

(a) (b)

Figure 6.1: Test rig: (a) top view of the rotary table with the AMB based gyroscope. (b) bottom of the rotary table with the reference gyroscope (Crossbow IMU700CB-200).

6.2 Experimental Results while the Rotary Table is Moving

The left picture of Fig.(6.2) demonstrates the ability of the AMB based gyroscope to measure the angular velocity of the rotary table.

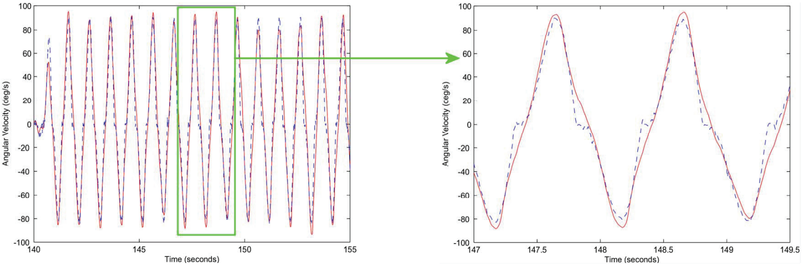

Figure 6.2: Angular velocity measurement about the X-axis. The ball shaped rotor has a diameter of 2[mm] and the orbital revolution frequency is 25[Hz]. The reference (resp. the prototype) measurement is represented in blue (resp. in red).

However, a zoom of this picture (see Fig.(6.2) right) shows a low pass filter behavior of the AMB based gyroscope. As a matter of fact, when the angular velocity becomes 0[°/s], the reference gyroscope measures a small step which corresponds to a signal containing high frequency components. This step is not measured by the AMB based gyroscope, hence its mentioned low pass filter behavior.

6.3 Experimental Results while the Rotary Table Stands Still: Noise Measurement

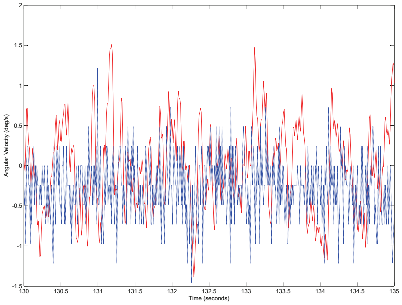

Figure 6.3: Noise in the measurement of the angular velocity about the X-axis. The ball shaped rotor has a diameter of 2[mm] and the orbital revolution frequency is 25[Hz]. The reference (resp. the prototype) measurement is represented in blue (resp. in red).

As shown in Fig.(6.3), the noise in the angular velocity measurement of 4[°/s] peak to peak for the AMB based gyroscope. This noise has been measured in the same conditions as the ones specified in the reference gyroscope datasheet [Inc08], i.e. with a refreshment rate of 100[Hz]. The experiments show a 2[°/s] peak to peak noise for the reference gyroscope.

6.4 Performance achieved with the Ball Orbit Measurement Method

The performances of the AMB based gyroscope when measuring the angular velocity with the ball orbit method are summarized in the following table:

Update rate	100 [Hz]
Start-up time valid data	< 1 [s]
Measurement range	±180 [°/s]
Bandwidth	10 [Hz]
Noise peak to peak	4 [°/s]

Table 6.1: Performance of AMB based gyroscope when measuring the angular velocity with the ball orbit method.

Chapter 7

Conclusions about the Ball Orbit Method

This angular velocity measurement method has shown a promising ability to measure the angular velocity (see §6.2). Its advantages and its inconvenients are presented in the following sections.

7.1 Advantages

The main advantage of this method results from the ball shape of the rotor. As matter of fact, this shape simplifies the mechanical design of the gyroscope as one only needs to control the spatial position of the rotor, what only requires three pairs of electromagnets. This low number of electromagnets should be an advantage for future miniaturization of such an AMB based gyroscope.

Moreover, the low coupling between the forces created by the pairs of electromagnets allows to consider that the rotor positionings along the X, Y and Z axes are fully independent from each other. This permits to have one controller per axis and to use a PID controller; the goal of the adaptive controller is only to fit the PID constants to the physical specifications of the prototype and not to the theoretical ones.

7.2 Inconvenients

Four main inconvenients with different origins have been pointed out for this orbital measurement method:

1. The creation of an orbit requires that the electromagnets have a motor function what results in an unbalanced dynamical force.
2. Because the rotor is only controlled in position, a cross-sensitivity between the acceleration and angular velocity measurements appears.
3. The measurement method is based on a derivation of the inclination angle of the plane of the ball orbit (see §4.2.3). Such a derivation is a source of noise.
4. The low pass filter behavior of this orbital method shown in §6.2 results in a lack of precision in the angular velocity measurement.

Part III

2^{nd} Gyroscopic Sensing Method: Cylindrical Spinning Rotor

Chapter 8

Mechanical Design of the AMB Gyroscope

8.1 Constraints on the Design

Constraints on the gyroscope size and measurement have been imposed by JTEKT at the beginning of the project.
The gyroscope outer volume must not exceed $40 \times 40 \times 40\,[\mathrm{cm}^3]$.
The gyroscope should measure angular velocities with a resolution of $1\,[^\circ/\mathrm{h}]$ and accelerations with a precision of $1\,[m \cdot g]$.

Because of their constant interaction, the actuating system, the sensor arrangement and the rotor have been simultaneously designed. This thesis proposes to describe the actuation system design and to derive the rotor shape and sensor arrangement from it. However, the reader should be aware of the arbitrary nature of the presentation order of these three pendants of a same design.

8.2 Actuation System

8.2.1 Radial Actuators

The radial actuators have three tasks:

- keeping the rotor polar axis parallel to the gyroscope stator main axis (attitude control).
- keeping the rotor center of gravity at the geometric center of the stator (position control).

- rotating the rotor around its main axis.

It has been chosen to place the radial actuators inside the rotor as in the AMB based hard drive prototype proposed by [Zoe02]. This configuration has some advantages:

- a strong integration of the radial actuation part.
- it offers more space outside the rotor for the sensing system, thus allowing more sensors to be mounted in order to have differential measurements.
- a more accurate rotor attitude measurement can be achieved through a bigger distance between the sensor positions and the gravity center of the rotor.
- as shown in §2.2.1.a, the rotor is larger and thus the precision of the measurement is increased.

8.2.1.a Attitude Control

In order to control the roll and pitch angles of the rotor, the radial actuators must be able to generate a torque and, therefore, need to be divided into at least two stages of identical sets of actuators as shown on Fig.(8.1).

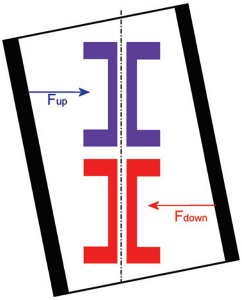

Figure 8.1: Cross section of the two stage distribution of the radial actuators. The upper (resp. lower) actuator stage is represented in blue (resp. red) and the rotor in black.

8.2.1.b Position Control

The radial actuators have been designed so that the weight of the rotor at the nominal actuator/rotor distance can be compensated with the force generated by a current of 100[mA] flowing through the coils of two actuators, each one belonging to one radial actuator stage. This limit has been chosen for three reasons: first to keep a sufficient margin in the case of a larger rotor/actuator distance, second to compensate for the vehicle movements and third to produce the motor currents to make the shaft rotate. The expression of this force is given by [Sch94] (this will be developed with more precision in chapter 9):

$$F_{act} = -\mu_0 \cdot N^2 \cdot A_c \cdot \frac{I^2}{\left[l_{rotor}/\mu_{rotor} + l_{stator}/\mu_{stator} + 2 \cdot d\right]^2} \tag{8.1}$$

In (Eq.8.1), N represents the number of turns of the coil, d the rotor to actuator distance, I the current flowing through the coil and A_c the active area of the actuator, i.e. the area through which the magnetic field flows from the actuator to the rotor. The influence of the other unknowns will not be considered in the dimensioning of the actuators because the high actuator and rotor relative permeabilities will lead to neglectable magnetic paths.

As the maximal current to compensate the rotor weight has been set, the magnetic force can only be increased by means of number (N) of coil turns or by the area A_c (see Eq.8.1). Two constraints limit the increase of these constants:

- Limit on N: the maximal volume of the coils so that they can fit inside the rotor.
- Limit on A_c: as A_c increases, the number of actuators decreases down to three actuators per stage. This is the minimum of actuators that are necessary to drive each the rotor upper and lower parts along two directions.

We have chosen to use three actuators per stage. This has two main drawbacks. First, the control of the rotor along the X and Y directions will be strongly coupled, because for each stage two out of the three electromagnets will be used for both the X and Y axis positioning of the rotor. Second the stiffness of the magnetic force along the Y axis will be multiplied by $\sin(120°) \approx 0.87$. Therefore, the magnetic force stiffness along the Y-axis will weaker than this along the X-axis.

Another solution which does not suffer from the control and coupling drawback would have been a solution with four actuators. This would have reduced the active area A_c by 30% and the number of turns N by 15%. Thus to get the same magnetic force along the Y axis (the weakest one when using three actuators) an increase of at least 40% in the current would have been necessary. On the other side, part of this current need would have been compensated by the easier four actuator based controller.

8.2.2 Axial Actuators

For the current application, the axial actuators have the only goal to suspend and position the gravity center of the rotor along the stator Z-axis. This will have two consequences:

- one axial actuator on each side of the rotor is sufficient to maintain its center of mass at a precise Z position. This configuration has been chosen to save space to meet the gyroscope constraints on the volume.
- the axial actuators should avoid to disturb the control of the rotor attitude control made by the radial actuators. Hence, their action line should be as close as possible to the stator Z-axis and symmetrical around this axis. Due to the placement of the radial actuators inside the rotor, a hole at the axial actuator center has to be bored to let the radial actuator cables pass.

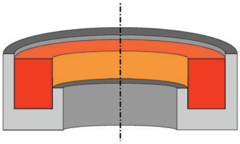

Figure 8.2: Cross section of the axial actuator shape. The electromagnet core and coil are respectively represented in grey and orange.

The choice of cylindrical electromagnets with a U-shape (see Fig.(8.2)) section has been made to close the flux with more efficiency and thus increasing the magnetic force. The electromagnet has been so designed that the attraction force on the rotor is always the same when horizontally displaced. One can say that the rotor is covered by the axial electromagnet.

However, when the rotor is slanted relatively to the stator main axis (see Fig.(8.3)), the strength of the axial forces will not be constant around the axial actuator resulting in the creation of a destabilizing moment. This phenomenon will be further described in the modeling of the axial moment (see §9.1.1.a).

8.3 Rotor Design

Fig.(8.4) shows the final rotor design as required by the actuation system configuration, i.e. a cylindrical tubular section to place the radial actuators inside the

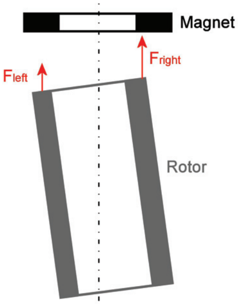

Figure 8.3: Cross section representation of the asymmetric forces exerted by one axial electromagnet on the rotor.

rotor and two discs in order to increase the axial force by means of a closer distance between the rotor and the outer axial actuator ring. Therefore, this force increase far from the rotor polar axis will all the more augment the destabilizing moment due to the axial actuators.

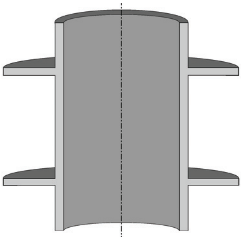

Figure 8.4: Cross section view of the rotor shape.

These two discs will permit to improve the measurement of the rotor attitude. Hence the measurement of the distance between these discs and the sensors will allow to compute the disc normal vector which has the same direction as the rotor polar axis. More details about the sensing system is given in appendix E.1.

8.4 The Induction Motor: a Precision Limit to the Angular Velocity Measurement

The developed prototype includes a motor function in order to spin the rotor around its polar axis to measure the angular velocity according to Eq.(2.3). Due to the prototype design the AMB radial actuators will also make the rotor spin. However, due its small dimensions, the rotor is very hard to modify. Moreover, as the actuators have been designed, there is no place to add magnets to spin the rotor. Due to these machining problems, it has been chosen to drive the rotor using the induction motor principle. This kind of motors permits to reach high rotation speed [Bol05], which is an advantage for the precision of angular velocity measurement (see Eq.(2.3)).

Principle of the Induction Motor

In this type of motors, eddy currents are induced onto a conductive rotor. In our case, these eddy currents will be induced by a rotating magnetic field at the stator. These eddy currents in the rotor generate a magnetic field whose frequency depends on the rotating speed of the rotor. The rotating magnetic fields at the rotor and at the stator interact and the difference between their frequencies will create the necessary torque to drive the rotor.

This type of motor is also called *asynchronous* because it cannot reach, without any external drive, the same speed as the stator magnetic field one. As a matter of fact, if it were the case, the rotor would not see any variation in the magnetic field. Hence, the currents would cancel as well as the torque that they induce and the rotor would not be driven any more. The quantity describing the difference between the rotor speed and the stator excitation frequency is called the *slip s* (see Eq.(8.2)).

$$s = \frac{\Omega_s - \Omega_z}{\Omega_s}, \text{ with } \begin{cases} \Omega_s \text{ the stator rotating field frequency.} \\ \Omega_z \text{ the rotor rotating field frequency.} \end{cases} \tag{8.2}$$

In general, the frequency of the stator rotating magnetic Ω_s field is given by Eq.(8.3) with ω_s the excitation frequency of the phases and the number of poles p. According to Eq.(8.3), the lower the number of poles, the higher Ω_s. The number of poles in our prototype corresponds to the number of radial actuators per stage, i.e. three (see Fig.(9.3)).

$$\Omega_s = \frac{\omega_s}{p} \tag{8.3}$$

A drawback of induction motors is their asynchronous behavior. As previously mentioned, their rotational speed is not the same as the actuator excitation frequency and varies along time. Hence, the achievable precision with such a type of motor will also depend of the range of variation of the actual rotor speed around the actuation excitation frequency. On that purpose, a sensor has been added to the gyroscope prototype to measure the rotor spinning speed.

8.5 Summary

A design of a miniaturized gyroscope has been proposed. Its cylindrical rotor is levitated by means of magnetic forces which are also responsible for spinning the rotor. A model of this prototype and the shaft attitude and position control will be presented in chapter 9 and chapter 10 respectively.

Chapter 9

Model of the AMB based Gyroscope

9.1 Actuators

9.1.1 Single Actuator

As a simple experience with a permanent magnet and a ferromagnetic rotor shows, the magnetic force exerted by the magnet on the rotor is an attractive force that increases as the rotor gets closer to the magnet. In the case of electromagnets the behavior of the magnetic force is the same one regarding the distance, but the effect due to the current flowing inside the coil has to be taken into account. As a matter of fact, even if the force created by an electromagnet will still be an attractive force, its strength can be modulated by the amount of current flowing inside the coil (see Fig.(9.1)).

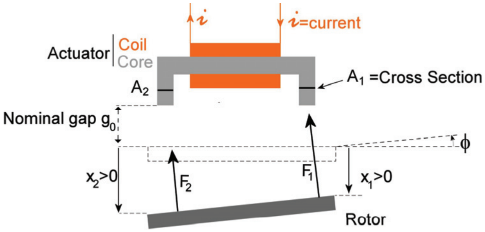

Figure 9.1: Scheme of the magnetic forces $\overrightarrow{F_1}$ and $\overrightarrow{F_2}$ exerted by a single actuator on the rotor.

According to [Sch94], the expression of the magnetic force created by one pole of the electromagnet on the rotor is:

$$F_p = \frac{-\mu_0 \cdot N^2 \cdot A_p \cdot i^2}{\left[l_{rotor}/\mu_{rotor} + l_{stator}/\mu_{stator} + d_1 + d_2\right]^2} \tag{9.1a}$$

$$= \frac{-a \cdot A_p}{\left[b + d_1 + d_2\right]^2} \cdot i^2, \quad \text{with } p \in \{1; 2\}. \tag{9.1b}$$

with:

A_p: the cross section of the electromagnet core.

N: the number of coil turns.

$(i_0 + \delta i)$: the current flowing inside the coil, i_0 being the nominal current.

l_{rotor}: the mean distance traveled by the magnetic field inside the rotor core.

l_{stator}: the mean distance traveled by the magnetic field inside the stator core.

μ_{rotor}: the relative permeability of the rotor core.

μ_{stator}: the relative permeability of the stator core.

d_p: distance between the actuator and the rotor. $d_p = g_0 + x_p$, g_0 being the nominal gap.

As shown in the last equality of Eq.(9.1b), the effect of these parameters can be included into two constants **a** and **b**. This last form will be more efficient in praxis as the effective values of **a** and **b** for each actuator will be derived from measurements.

9.1.1.a Single Axial Actuator

As mentioned in §8.2.2, when a disc is slanted relatively to the stator polar axis, all the points of the disc are not at the same distance from the axial actuator. Hence, the force exerted by the electromagnet on the disc will not be uniformly distributed on the disc. Therefore, we propose in this section a model of the force and torques exerted by an axial electromagnet on a disc. On that purpose, we consider Fig.(9.2). The model of this force is expressed in the stator reference frame (A,x_s, y_s, z_s) introduced in section §2.1.1.

In this figure, a point P belongs to a ring (inner radius r^i and outer radius r^o, with $r^o > r^i$) of center C. The coordinates of P within this ring are the distance CP called r and the angle α. This ring was subject to a rotation (ϕ_x,ϕ_y), as defined

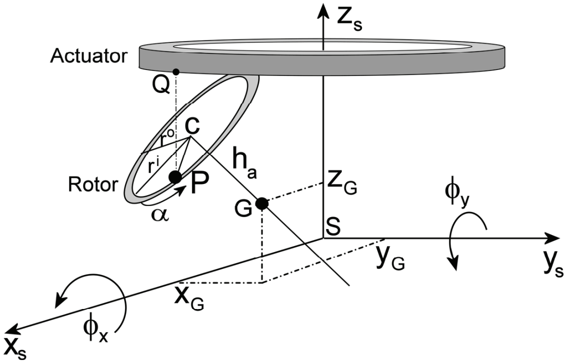

Figure 9.2: Representation of a rotor ring slanted relatively to the reference frame (S,x_s, y_s, z_s) with an axial actuator placed on the Z_s-axis.

in §2.1.2, around the X_s and Y_s axes. This rotation occurs around the axis $\overrightarrow{GC}$, G being the rotor center of mass with the coordinates x_G, y_G and z_G. The distance CG is noted h_a ("a" for axial).

We call Q the point of the axial actuator that is the closest to P and, thus, exerts the electromagnetic force on P. The coordinate of Q along the axis Z_s is called z_q. Therefore, the distance $QP = \|\overrightarrow{QP}\| = \|\overrightarrow{QS} + \overrightarrow{SP}\|$ becomes according to Eq.(9.2):

$$QP = \frac{z_q - z_G - h\cos(\phi_x)\cos(\phi_y) + r\cos(\alpha)\cos(\phi_x)\sin(\phi_y) - r\sin(\alpha)\sin(\phi_x)}{\cos(\phi_x)\cos(\phi_y)} \tag{9.2}$$

The attracting surface of the axial actuator (see Fig.(8.2)) is made out of two rings that will be called inner and outer rings (subscript 1 and 2 respectively). Hence, the part of the rotor that is attracted by the actuator can be seen as the projection along the Z-axis of these rings on the rotor. Therefore the expression of the electromagnetic force df_1 acting on the area $ds_1 = S_{a1}/(2\pi)d\alpha$ (S_{a1} being the total active surface of the inner ring) around a point P belonging to the inner ring (it is analog for a point belonging to the outer ring) is, according to Eq.(9.1), given by:

$$df_1 = \frac{S_{a1}}{2\pi}\frac{a \cdot i^2}{[b_a + d_1 + d_2]^2} \cdot d\alpha = \frac{S_{a1}}{2\pi}\frac{a \cdot i^2 \cos^2(\phi_x)\cos^2(\phi_y)}{\Delta_a^2} \cdot d\alpha \tag{9.3}$$

$$\text{with} \quad \Delta_a = \begin{aligned}[t] & b_a\cos(\phi_x)\cos(\phi_y) + (z_{q1} + z_{q2}) - 2z_{CM} - (h_{a1} + h_{a2})\cos(\phi_x)\cos(\phi_y) \\ & +(r_1 + r_2)\cos(\alpha)\cos(\phi_x)\sin(\phi_y) - (r_1 + r_2)\sin(\alpha)\sin(\phi_x) \end{aligned}$$

When z_G, ϕ_x and ϕ_y are small, first order Taylor series applied to Eq.(9.3) return for df_1 the following expression:

$$df_1 = ai^2 \cdot \frac{S_{a1}}{2\pi} \cdot \frac{\Delta_{a0} + 2\,(r_1 + r_2)\,(\sin(\alpha)\phi_x - \cos(\alpha)\phi_y) + 4z_G}{\Delta_{a0}^3} \cdot d\alpha \tag{9.4}$$

$$\text{with} \quad \Delta_{a0} = b_a + (z_{q1} + z_{q2}) - (h_{a1} + h_{a2})$$

Integrating the Taylor series of df_1 and df_2 over the surfaces ds_1 and ds_2 respectively, the expression of the force of the whole axial actuator is given by Eq.(9.5) with S_{a1} and S_{a2} the total surfaces of the inner and outer rings:

$$\overrightarrow{F_{act}} = \frac{ai_0}{\Delta_{a0}^3} \cdot (S_{a1} + S_{a2}) \begin{bmatrix} i_0\Delta_{a0} \cdot \phi_y \\ -i_0\Delta_{a0} \cdot \phi_x \\ i_0\Delta_{a0} + 4i_0 z_G + 2\Delta_{a0}\delta i \end{bmatrix} \tag{9.5}$$

The destabilizing effect of the axial force has for origin the torque created by this force on the rotor (see Fig.(8.3)). Therefore, the expression of the torque τ_x (resp. τ_y) about the x-axis (resp. the y-axis) exerted on the point P is given by:

$$\overrightarrow{d\tau_1} = \overrightarrow{AP_1} \times \overrightarrow{df_1} = r_1 \cdot df_1 \cdot \begin{bmatrix} \sin(\alpha)\cos(\phi_y) \\ \sin(\alpha)\sin(\phi_x)\sin(\phi_y) - \cos(\alpha)\cos(\phi_x) \\ -\sin(\alpha)\cos(\phi_x)\sin(\phi_y) - \cos(\alpha)\sin(\phi_x) \end{bmatrix}$$

The integration over the angle α of the Taylor series of these torque expressions for small z_G, ϕ_x and ϕ_y, the torque formulas are given by Eq.(9.6). According to this equation, the torque τ_{x1} and τ_{y1} are only proportional respectively to ϕ_x and ϕ_y.

$$\tau_p = \frac{ai^2}{\Delta_{a0}^3} \cdot (r_1 + r_2) \cdot (r_1 S_{a1} + r_2 S_{a2}) \cdot \phi_p, \quad p \in \{x; y\}. \tag{9.6}$$

9.1.1.b Single Radial Actuator

For the radial actuator, the distance between the point Q of the electromagnet that exerts a force on the rotor closest point P is harder to compute. In our prototype the maximal difference between the Z coordinate of P and Q is below $0.2[\mu m]$, therefore we can assume that they have the same Z coordinates. This simplifies the resolution and means that the electromagnetic force is fully radial.

The coordinates of Q are $[\rho\cos(\beta),\ \rho\sin(\beta),\ h_r]$. ρ is the radial actuator radius. The notations for the point P are the same than in the previous section. The coordinates of the vector $\overrightarrow{QP}$ are developed using Taylor series for x_G, y_G, z_G, ϕ_x and ϕ_y are small. These developed coordinates are given by:

$$\overrightarrow{QP} = \begin{bmatrix} x_G + r\cos(\alpha) + h_r\phi_y - \rho\cos(\beta) \\ y_G + r\sin(\alpha) - h_r\phi_x - \rho\sin(\beta) \\ 0 \end{bmatrix} \tag{9.7}$$

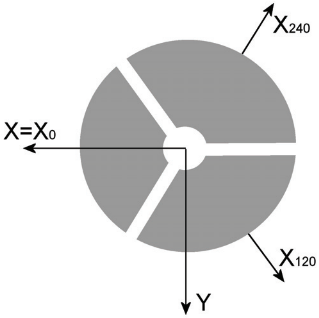

Figure 9.3: Upper view of a radial actuation stage. The actuators are represented in grey and their action axes are called X_0, X_{120} and X_{240}.

The angle β can be obtained by minimization of the square of the distance QP (see Eq.(9.7)). This minimization over the whole space in which the rotor can move returns a maximum angle $|\beta - \alpha| = 3.5°$, therefore we will assume in the following that $\beta = \alpha$. With this assumption the distance QP becomes:

$$QP^2 = [r-\rho] \cdot [(r-\rho) + 2\left(\cos(\alpha)x_G + \sin(\alpha)y_G\right) + 2h_r\left(\cos(\alpha)\phi_y - \sin(\alpha)\phi_x\right)] \tag{9.8}$$

Using the same method as in §9.1.1.a, the radial force created by a two pole electromagnet is given by:

$$\begin{aligned}\overrightarrow{F_{rad}} = \;& \tfrac{-ai^2(S_{r1}+S_{r2})}{\Delta_{r0}^3} \cdot \Big[\Delta_{r0} - 2\tfrac{\cos(\alpha_0)\sin(\gamma)}{\gamma}\left(2x_G + (h_{r1}+h_{r2})\phi_y\right) \\ & -2\tfrac{\sin(\alpha_0)\sin(\gamma)}{\gamma}\left(2y_G - (h_{r1}+h_{r2})\phi_x\right)\Big] \begin{bmatrix} \cos(\alpha_0) \\ \sin(\alpha_0) \\ 0 \end{bmatrix}\end{aligned} \tag{9.9a}$$

The new variables introduced in Eq.(9.9) are:

- $\Delta_{r0} = b + 2(r-\rho)$.
- $S_r = 2\gamma \cdot \rho \cdot e$. S_r is the surface of one pole of a radial electromagnet. The pole shape is cylindrical section with an angular opening of 2γ (see Fig.(9.3)). e is the pole thickness but this variable will not been used any further.
- α_0 is the mean angle of an actuator, in our case it can be 0, $\frac{2\pi}{3}$ or $\frac{4\pi}{3}$ depending on the actuator.

- $h_j,\ j \in \{1;2\}$ is the Z coordinate of the pole j.

The expression of the torque τ created by a single actuator is not developed here because it is too long and will not be directly used, but it can be found in §C.

9.1.2 Complete Actuation System

9.1.2.a Axial Actuators

As described in §8.2.2, two axial electromagnets are placed along the Z-axis symmetrically about the XY-plane.

According to Eq.(9.5), the sum of the forces by the two electromagnets is:

$$\overrightarrow{F_{axial}} = \overrightarrow{F_{axial}^{up}} + \overrightarrow{F_{axial}^{down}} = \frac{2ai_0}{\Delta_{a0}^3} \cdot (S_{a1} + S_{a2}) \left[4i_0 z_G + \Delta_{a0}\left(\delta i_z^{up} - \delta i_z^{down}\right)\right] \cdot \vec{z} \quad (9.10)$$

Refereing to Eq.(9.6), the sum of the axial torques is given by:

$$\tau_p = 2 \cdot \frac{ai_0^2}{\Delta_{a0}^3} \cdot (r_1 + r_2) \cdot (r_1 S_{a1} + r_2 S_{a2}) \cdot \phi_p, \quad p \in \{x;y\}. \quad (9.11)$$

Eq.(9.11) shows that the axial torques are only proportional to the angles. Therefore, the torques created by the axial electromagnets can only be compensated by the radial actuators.

9.1.2.b Radial Actuators

As described in §9.1.1.b, the radial actuation system is made out of two stages of three actuators.

The force exerted by the six radial actuators on the rotor is, according to Eq.(9.9), by:

$$\frac{\Delta_{r0}^3}{2ai_0\left(S_{r1} + S_{r2}\right)} \cdot \overrightarrow{F_{radial}} = \begin{bmatrix} \Delta_{r0}\left[\left(\delta i_{120}^{up} + \delta i_{120}^{down}\right) + \left(\delta i_{240}^{up} + \delta i_{240}^{down}\right)\right] \\ \sqrt{3}\Delta_{r0}\left[-\left(\delta i_{120}^{up} + \delta i_{120}^{down}\right) + \left(\delta i_{240}^{up} + \delta i_{240}^{down}\right)\right] \\ 0 \end{bmatrix} + \begin{bmatrix} -2\Delta_{r0}\left(\delta i_0^{up} + \delta i_0^{down}\right) + 3i_0\frac{\sin(\gamma)}{\gamma} \cdot x_G \\ 3i_0\frac{\sin(\gamma)}{\gamma} \cdot y_G \\ 0 \end{bmatrix} \quad (9.12a)$$

The computation of the expression of the global torque $\sum \overrightarrow{T_{radial}}$ is described in details in §C. Its expression is given by:

$$
\begin{aligned}
\sum T_x &= \frac{2ai_0S_r(h_{r1}+h_{r2})}{\gamma\Delta_{r0}^2}\sin(\gamma)\sin(\frac{2\pi}{3})\left[\left(\delta i_{120}^{up}-\delta i_{120}^{down}\right)-\left(\delta i_{240}^{up}-\delta i_{240}^{down}\right)\right] \\
&\quad +\frac{6ai_0^2S_r}{\Delta_{r0}^2}\cdot r\cdot\phi_x
\end{aligned}
\tag{9.13a}
$$

$$
\begin{aligned}
\sum T_y &= -\frac{2ai_0S_r(h_{r1}+h_{r2})}{\gamma\Delta_{r0}^2}\sin(\gamma)\Big[\left(\delta i_0^{up}-\delta i_0^{down}\right) \\
&\quad -\frac{1}{2}\cdot\left(\delta i_{120}^{up}-\delta i_{120}^{down}+\delta i_{240}^{up}-\delta i_{240}^{down}\right)\ \Big] \\
&\quad +\frac{6ai_0^2S_r}{\Delta_{r0}^2}\cdot r\cdot\phi_y
\end{aligned}
\tag{9.13b}
$$

$$
\sum T_z = 0 \tag{9.13c}
$$

9.1.2.c Combination of the Effect of the Axial and Radial Actuators

The force F_{AMB} and the torque T_{AMB} combining the effects of both the axial and radial actuators are respectively given by:

$$
\begin{aligned}
\vec{F}_{AMB} &= \begin{bmatrix} k_r\cdot x_G \\ k_r\cdot y_G \\ k_z\cdot z_G \end{bmatrix} \\
&\quad + \begin{bmatrix} k_{i_r}\cdot\left[-2\left(\delta i_0^{up}+\delta i_0^{do}\right)+\left(\delta i_{120}^{up}+\delta i_{120}^{do}\right)+\left(\delta i_{240}^{up}+\delta i_{240}^{do}\right)\right] \\ k_{i_r}\cdot\sqrt{3}\left[-\left(\delta i_{120}^{up}+\delta i_{120}^{do}\right)+\left(\delta i_{240}^{up}+\delta i_{240}^{do}\right)\right] \\ k_{i_z}\left(\delta i_z^{up}-\delta i_z^{do}\right) \end{bmatrix}
\end{aligned}
\tag{9.14a}
$$

$$
\begin{aligned}
\vec{T}_{AMB} &= \begin{bmatrix} k_\phi\cdot\Phi_x \\ k_\phi\cdot\Phi_y \\ 0 \end{bmatrix} \\
&\quad + \begin{bmatrix} k_{i_\phi}\sqrt{3}\left[\left(\delta i_{120}^{up}-\delta i_{120}^{do}\right)-\left(\delta i_{240}^{up}-\delta i_{240}^{do}\right)\right] \\ -k_{i_\phi}\left[2\left(\delta i_0^{up}-\delta i_0^{do}\right)-\sqrt{3}\cdot\left(\delta i_{120}^{up}-\delta i_{120}^{do}+\delta i_{240}^{up}-\delta i_{240}^{do}\right)\right] \\ 0 \end{bmatrix}
\end{aligned}
\tag{9.14b}
$$

Three vectors X_G, δI_c and FT_{amb} as well two matrices K_x and K_i are introduced (more details about these can be found in §B.1):

- X_G contains the coordinates of the rotor (z_G, x_G, ϕ_y, y_G, ϕ_x).

- δI_c contains the currents flowing in all the electromagnet coils.
- FT_{AMB} contains the forces and torques applied to the rotor by the electromagnets.
- K_x represents the force displacement stiffness matrix of the system.
- K_i represents the force current stiffness matrix of the system.

With these notations the AMB force tensor $\overrightarrow{FT_{AMB}}$ becomes:

$$\overrightarrow{FT_{AMB}} = -K_x \cdot X_G + K_i \cdot \delta I_c \tag{9.15}$$

9.2 Rotor Mechanics

9.2.1 Gyroscopic Effects

The hardest part to model the gyroscopic effects, on which the angular velocity measurement relies, may be to answer a question that seems simple: "In which reference frame is the current equation expressed?". Therefore precise notations need to be introduced:

- the inertial reference frame (O,x_f, y_f, z_f) which is considered as fix. Coordinates written in this frame will be described by the subscript f.
- the reference frame (S, x_s, y_s, z_s) bound to the stator with its origin at the electromagnetic center S of the stator. To simplify, we will consider in this thesis that the electromagnetic and the geometrical center of the stator are merged.
- the reference frame (G, x_r, y_r, z_r) bound to the center of gravity G of the rotor. The only movement of the rotor in this frame is its own spin speed Ω_z. This frame will be noted (r).
- the rotation angle and the rotation speed of the frame s about the frame f is given by $\phi_{sf} = \left(\phi_x^{sf}, \phi_y^{sf}\right)$ (see §2.1.2) resp. ω_{sf}.
- the rotation angle and the rotation speed of the frame r about the frame s is given by $\phi_{rs} = \left(\phi_x^{rs}, \phi_y^{rs}\right)$ (see §2.1.2) resp. ω_{rs}.

A reference frame is not considered in this thesis; we considered the surface of earth as an inertial system which is hopefully for the Foucault pendulum experiment not the case. However, the gyroscope is aimed for vehicles like cars, which have a much higher angular velocity (about 1[rad/s) than the earth does ($7.27 \cdot 10^{-5}$[rad/s]).

As mentioned in §2.2.1.a, the gyroscopic effects appear when the rotor angular momentum is derived. Therefore its rotation must be well defined. On that purpose, we will use the Euler rotation definition used in §2.1.2.

The rotor is affected by four referential rotations and by its spin speed Ω_z. Two referential rotations of the type ϕ_x and ϕ_y affect the stator (resp. the rotor) about the fix frame (resp. the stator). As the only available sensors to describe the complete gyroscopic movement of the rotor are bound to the stator, the angular moment L_G of the rotor expressed in G will be derived in the stator frame (see Eq.(9.16)).

$$\left[\frac{dL_G}{dt}\right]_s = \left[\vec{\phi}_{rs}\right]_s \cdot \left[\left[\left.\frac{dL_G}{dt}\right|_r\right]_r + \left[\vec{\omega}_{rf}\right]_r \times \left[L_G\right]_r\right] \tag{9.16}$$

In Eq.(9.16), $\left.\frac{d\bullet}{dt}\right|_i$ means that the derivative of $\bullet$ only includes its coordinates and not the reference frame in which $\bullet$ is expressed.

According to Eq.(9.16), the expression of the first derivative of the rotor angular momentum expressed in the stator coordinate frame is proposed in Eq.(9.17). As the gyroscope only measures the angular velocities ($\dot{\phi}_x^{sf}$, $\dot{\phi}_y^{sf}$) of the vehicle relatively to the ground, the derivative of the angular momentum about the Z-axis is not presented here. This equation is a first order Taylor series assuming that the rotor angles ϕ_x^{rs} and ϕ_y^{rs} as well as the corresponding angular velocities are very small compared to the stator angular data relatively to the fix frame. The detailed development of Eq.(9.17) can be found in §A.

$$\begin{aligned}
\tfrac{d\vec{L}_G}{dt} \quad &= \quad J_r \begin{bmatrix} \left(\ddot{\phi}_x^{sf} + \ddot{\phi}_x^{rs}\right) + c_x^{sf} \cdot s_x^{sf} \cdot \left[\left(\dot{\phi}_y^{sf}\right)^2 + 2 \cdot \dot{\phi}_y^{sf} \cdot \dot{\phi}_y^{rs}\right] \\ \left(\ddot{\phi}_y^{sf} + \ddot{\phi}_y^{rs}\right) \cdot c_x^{sf} - 2 \cdot s_x^{sf} \cdot \left(\dot{\phi}_y^{sf} \cdot \dot{\phi}_x^{sf} + \dot{\phi}_x^{sf} \cdot \dot{\phi}_y^{rs} + \dot{\phi}_y^{sf} \cdot \dot{\phi}_x^{rs}\right) \end{bmatrix} \\
&\quad + J_z \begin{bmatrix} -c_x^{sf} \cdot s_x^{sf} \cdot \left[\left(\dot{\phi}_y^{sf}\right)^2 + 2 \cdot \dot{\phi}_y^{sf} \cdot \dot{\phi}_y^{rs}\right] \\ s_x^{sf} \cdot \left(\dot{\phi}_y^{sf} \cdot \dot{\phi}_x^{sf} + \dot{\phi}_x^{sf} \cdot \dot{\phi}_y^{rs} + \dot{\phi}_y^{sf} \cdot \dot{\phi}_x^{rs}\right) \end{bmatrix} \\
&\quad + J_z \cdot \Omega_z \begin{bmatrix} c_x^{sf} \cdot \left(\dot{\phi}_y^{sf} + \dot{\phi}_y^{rs}\right) \\ -\left(\dot{\phi}_x^{sf} + \dot{\phi}_x^{rs}\right) \end{bmatrix} \\
&= \quad J_r \begin{bmatrix} \ddot{\phi}_x^{rs} \\ \ddot{\phi}_y^{rs} \cdot c_x^{sf} \end{bmatrix} + G^{rs} \begin{bmatrix} \dot{\phi}_x^{rs} \\ \dot{\phi}_y^{rs} \cdot c_x^{sf} \end{bmatrix} - \vec{T}_{gyro}^{sf} - \vec{T}_{acc}^{sf} - \vec{T}_{mix}
\end{aligned} \tag{9.17}$$

$$\text{with } G^{rs} = \begin{bmatrix} 0 & J_z\Omega_z \\ -J_z\Omega_z & 0 \end{bmatrix},$$

$$\vec{T}^{sf}_{gyro} = -J_z \cdot \Omega_z \begin{bmatrix} c^{sf}_x \cdot \dot{\phi}^{sf}_y \\ -\dot{\phi}^{sf}_x \end{bmatrix}$$

$$\vec{T}^{sf}_{acc} = -J_r \begin{bmatrix} \ddot{\phi}^{sf}_x \\ \ddot{\phi}^{sf}_y \cdot c^{sf}_x \end{bmatrix}$$

$$\begin{aligned} \vec{T}_{mix} = \quad & -J_r \begin{bmatrix} c^{sf}_x \cdot s^{sf}_x \cdot \left[\left(\dot{\phi}^{sf}_y\right)^2 + 2 \cdot \dot{\phi}^{sf}_y \cdot \dot{\phi}^{rs}_y\right] \\ -2 \cdot s^{sf}_x \cdot \left(\dot{\phi}^{sf}_y \cdot \dot{\phi}^{sf}_x + \dot{\phi}^{sf}_x \cdot \dot{\phi}^{rs}_y + \dot{\phi}^{sf}_y \cdot \dot{\phi}^{rs}_x\right) \end{bmatrix} \\ & -J_z \begin{bmatrix} -c^{sf}_x \cdot s^{sf}_x \cdot \left[\left(\dot{\phi}^{sf}_y\right)^2 + 2 \cdot \dot{\phi}^{sf}_y \cdot \dot{\phi}^{rs}_y\right] \\ s^{sf}_x \cdot \left(\dot{\phi}^{sf}_y \cdot \dot{\phi}^{sf}_x + \dot{\phi}^{sf}_x \cdot \dot{\phi}^{rs}_y + \dot{\phi}^{sf}_y \cdot \dot{\phi}^{rs}_x\right) \end{bmatrix} \end{aligned}$$

and J_r, J_z the rotor radial and polar inertia.

The matrix G^{rs} represents the gyroscopic effects induced by the movement of the rotor itself. The torque $\vec{T}^{sf}_{gyro}$ represents the gyroscopic effects due to the movement of the vehicle. The torque represents $\vec{T}^{sf}_{acc}$ describes the action on the rotor due to the angular accelerations of the stator. Finally, the torque $\vec{T}_{mix}$ represents the influence of the stator onto the rotor movements and vice versa.

As shown in Eq.(9.17), the expression of the torque due to the external gyroscopic effects $\vec{T}^{sf}_{gyro}$ is quite completed but it must well known to measure the angular velocity of the vehicle within the fix reference frame. To simplify the expression of this torque two main assumptions are made throughout this thesis:

1. As mentioned in §1.1, such types of gyroscopes are interesting if the vehicle on which they are mounted has no fix link with the ground as a car, a mobile robot, a satellite, an helicopter[1]... An example of a fix to the ground vehicles would be a machining tool for which motor encoders are much easier to use. Therefore, we consider that the gyroscope developed in this thesis is built on the former class of vehicles. Of all the vehicles, that have been described the helicopter is the one that can reach the highest angular velocities (about 20[rpm]). Therefore the sampling time (T_s=0.2[ms]) of the controller is sufficiently high in comparison to the vehicle angular velocity to consider that the terms c^{sf}_x and s^{sf}_x included in the torque $\vec{T}^{sf}_{gyro}$ are, at the time t, constants based on the vehicle attitude measured at the time $t - T_s$.

2. According to the previous assumption, a controller with sufficient dynamics to achieve a near to perfect trajectory control can be found for the currently

---

[1] An helicopter is in fact a gyroscope.

studied gyroscope. Therefore the terms of $\vec{T}^{sf}_{gyro}$ that contain the angular data describing the movements of the rotor about the stator can be canceled.

The complete action $\overrightarrow{FT}^{sf}_{gyro}$ of the gyroscopic effects on the rotor are:

$$\overrightarrow{FT}^{sf}_{gyro} = B_{gyro} \cdot \vec{T}^{sf}_{gyro}, \text{ with } B_{gyro} = \begin{bmatrix} 0 & 0 \\ 0 & 0 \\ 0 & 1 \\ 0 & 0 \\ 1 & 0 \end{bmatrix} \tag{9.18}$$

9.2.2 Unbalance Effects

A rotor is never perfectly balanced due among other to hard contacts with the stator during tests, machining, thermal dilatation... Certain applications can profit from it [Bol05]. Unfortunately this is not our case. This rotor unbalance leads to the creation of a centrifugal force proportional to the square of the rotor spin speed. As a high spin speed is one of the most important component for the angular velocity measurement, this rotor unbalance must be considered in our model.

To model the action $\overrightarrow{TF}_u$ of the unbalance force $\vec{F}_u$ on the rotor, a mass m_u, on which this force applies, is artificially bound to the rotor. This mass is placed at the coordinates $[x_u, 0, z_u]$ (this set of coordinates is expressed in the reference frame bound to the stator). Expressed in the reference frame bound to the rotor, the unbalance effects on the rotor will be:

$$\overrightarrow{FT}_u = B_u \cdot \vec{F}_u, \text{ with } B_u = \begin{bmatrix} 0 & 0 \\ 1 & 0 \\ z_u & 0 \\ 0 & 1 \\ 0 & -z_u \end{bmatrix} \text{ and } \vec{F}_u = -m_u x_u \Omega_z^2 \begin{bmatrix} 1 \\ 0 \end{bmatrix}. \tag{9.19}$$

9.2.3 Rigid Body Model

According to the finite element simulations (see Fig.(9.4)), the first bending modes of the rotor come from the two discs which start to oscillate around 11′000[Hz]. This is much higher than the spin speed of the rotor and therefore the assumption of a rigid rotor will be made for the model of the gyroscope.

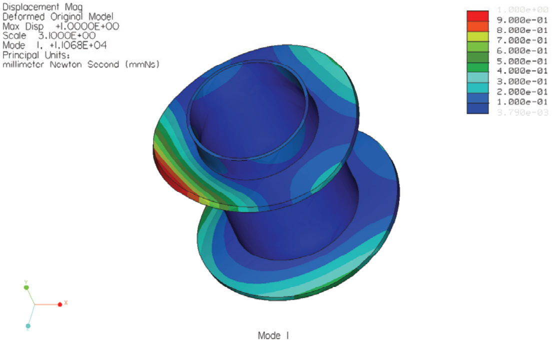
Displacement Mag
Deformed Original Model
Max Disp +1.0000E+00
Scale 3.1000E+00
Mode 1, +1.1068E+04
Principal Units:
millimeter Newton Second (mmNs)
1.000e+00
9.000e-01
8.000e-01
7.000e-01
6.000e-01
5.000e-01
4.000e-01
3.000e-01
2.000e-01
1.000e-01
3.790e-03
Y
X
Mode 1

Figure 9.4: First bending mode of the rotor at the frequency 11′068[Hz]. This simulation has been run by Dominique Chapuis.

9.3 Complete Model

Using the reference frames introduced in §9.2.1, the part of dynamics acceleration $\overrightarrow{a}_G$ of the shaft is given by:

$$m\overrightarrow{a}^s_G = \sum\vec{F} = m\overrightarrow{g} + \overrightarrow{F}_{AMB} - m\vec{a}^{sf} + \vec{F}_u \tag{9.20}$$

With:

- $m\vec{g}$: the gravity acting on the rotor.
- $\vec{a}^{sf}$: the external accelerations comprising the Coriolis acceleration, the acceleration of S (the origin of the stator reference frame).

According to Eq.(9.17) and to Eq.(9.19), the dynamical equations of the shaft attitude $\phi^{rs} = \left[\phi^{rs}_x,\ \phi^{rs}_y\right]$ are given by:

$$J_r\frac{d^2\vec{\phi}^{rs}}{dt^2} = \sum\vec{T} = -G^{rs}\frac{d\vec{\phi}^{rs}}{dt} + \vec{T}_{AMB} + \vec{T}^{sf}_{gyro} + \vec{T}^{sf}_{acc} + \vec{T}_{mix} + \begin{bmatrix} 0 & -z_u \\ z_u & 0 \end{bmatrix}\cdot\vec{F}_u \tag{9.21}$$

Expressed in an unified matrix form Eq.(9.20) and Eq.(9.21) become (the expression of X_G is presented in Eq.(B.1)):

$$\begin{aligned}
M \cdot \ddot{X}_G &= \overrightarrow{FT}_{AMB} - G^{rs} \cdot \dot{X}_G + m\vec{g} + \overrightarrow{FT}^{sf}_{gyro} + \overrightarrow{FT}^{sf}_{acc} + \overrightarrow{FT}_{mix} + \overrightarrow{FT}_u \\
&= -K_x \cdot X_G + K_i \cdot \delta I_c - G^{rs} \cdot \dot{X}_G \\
&\quad + m\vec{g} + \overrightarrow{FT}^{sf}_{gyro} + \overrightarrow{FT}^{sf}_{acc} + \overrightarrow{FT}_u \\
\text{with } \overrightarrow{FT}^{sf}_{acc} &= \left[0, -m a^{sf}_x, -J_r \ddot{\phi}^{sf}_y, -m a^{sf}_y, -J_r \ddot{\phi}^{sf}_x\right]^T \\
\overrightarrow{FT}^{sf}_{mix} &= \left[0, 0, T_{mix(2,1)}, 0, T_{mix(1,1)}\right]^T
\end{aligned} \tag{9.22}$$

The matrices M (mass matrix) and G^{rs} (gyroscopic matrix) are presented in Appendix B.1.

Eq.(9.22) reveals three reasons that impose the use of a controller for such a system:

1. The instability inherent to the AMB systems: the matrix $[M^{-1} \cdot K_x]$ (stiffness matrix expressed in the stator coordinate system) is diagonal and only contains negative terms, which means that the poles of the system belong to the complex right half plane. Thus the solution of the system homogeneous equation contains a diverging exponential term.

2. The gyroscopic effects: the matrix $[M^{-1} \cdot G^{rs}]$ (equivalent to Eq.(9.22) shows that the differential equations of the angles ϕ^{rs}_x and ϕ^{rs}_y are fully coupled through the rotating speed Ω_z of the rotor around its main inertia axis. Moreover, this coupling is absolutely nonlinear, as it consists in the multiplication of the angular velocity $\dot{\phi}^{rs}_x$ or $\dot{\phi}^{rs}_y$ with Ω_z, which in our case will not be a constant. As a matter fact, we have seen in section 2.2.1.a that the higher Ω_z, the better the gyroscope precision.

3. The external actions, $\vec{d}(t) = m\vec{g} + \overrightarrow{FT}^{sf}_{acc} + \overrightarrow{FT}^{sf}_{gyro} + \overrightarrow{FT}_{mix}$, are *a priori* not known and will therefore be considered as disturbances.

A state space expression of Eq.(9.22) would be:

$$\begin{cases} \dot{\chi}_{\mathrm{G}} &= \begin{bmatrix} 0_{55} & I_{55} \\ -M^{-1}K_x & -M^{-1}G^{rs} \end{bmatrix} \chi_{\mathrm{G}} + \begin{bmatrix} 0_{58} \\ M^{-1}K_i \end{bmatrix} \delta I_c + \begin{bmatrix} 0 \\ M^{-1}\left(\vec{d}(t) + \overrightarrow{FT}_u\right) \end{bmatrix} \\ & = A \cdot \chi_{\mathrm{G}} + B \cdot \delta I_c + \begin{bmatrix} 0_{51} \\ M^{-1}d(t) \end{bmatrix} + \begin{bmatrix} 0_{52} \\ M^{-1}B_u \end{bmatrix} \vec{F}_u \\ Y_G &= [I_{55} \quad 0_{55}]\, \chi_{\mathrm{G}} = C \cdot \chi_{\mathrm{G}} + D \cdot \delta I_c \end{cases}$$

$$\text{with } \chi_{\mathrm{G}} = \begin{bmatrix} X_G & \dot{X}_G \end{bmatrix}^T \tag{9.23}$$

Based on this state space model, a method to measure the vehicle angular velocity will be presented in section 9.4 and a controller synthesized in chapter 10.

9.4 Measurement of the Angular Velocity

The proposed measurement algorithm is based on the model developed in §9.3 and on the assumption of a perfect trajectory tracking, i.e. the position and the attitude of the rotor as well as their derivatives are null. The consequences of this assumption will be used for the angular velocity measurement algorithm and explained in the corresponding paragraphs.

Perfect trajectory tracking means that the active magnetic bearings achieve a perfect compensation of the external actions onto the rotor. Concerning the angular velocity, this means a perfect compensation of the unbalance effects, of the gyroscope and acceleration torques due to the rotation of the stator about the fix reference frame.

With these assumptions, Eq.(9.21) can be rewritten as:

$$J_r \ddot{\phi}_x^{sf} + (J_r - J_z)\, c_x^{sf} \cdot s_x^{sf} \cdot \left(\dot{\phi}_y^{sf}\right)^2 + J_z \Omega_z \cdot c_x^{sf} \cdot \dot{\phi}_y^{sf} = k_{i_\phi} \cdot \delta i_{\phi_x} + T_{u_x} \tag{9.24a}$$

$$J_r \cdot \ddot{\phi}_y^{sf} \cdot c_x^{sf} + (J_z - 2J_r)\, s_x^{sf} \cdot \dot{\phi}_y^{sf} \cdot \dot{\phi}_x^{sf} - J_z \Omega_z \cdot \dot{\phi}_x^{sf} = k_{i_\phi} \cdot \delta i_{\phi_y} + T_{u_y} \tag{9.24b}$$

with T_{u_x} and T_{u_y} the torques due to the unbalance effects.

At first sight, the gyroscopic differential equation system (c.f. Eq.(9.24)) may seem easy to solve. However, one must remark the term c_x^{sf} in Eq.(9.24a) which introduces a non linear dependency from the angle ϕ_x^{sf}. This problem can be easily overcome using the simplification $c_x^{sf} = constant$ if the vehicle moves in the range of small angles within the fix reference frame or when its rotation occurs only about one axis[Mar06].

However, for the desired range of vehicles on which the present gyroscope should be mounted this cosine term can not always be neglected. For example, it can be neglected in a car if the Z-axis is horizontal and pointing in front of the car and the X-axis is horizontal and perpendicular to the Z-axis. The maximal slope experienced by a car is around 15% which means $c_x^{sf} \approx 0.989$. On the opposite in an helicopter, a change in attitude of 30° is absolutely not rare and the cosine can not be neglected any more. Therefore, the cosine term included in Eq.(9.24a) will be maintained. The effects of the cosine will be shown in §11.

The literature often tackles with the resolution of gyroscopic equations in the case of small vehicle angles [Law98] or with the stabilization of the gyroscopic phenomenon [Wan], but the previously mentioned cosine problem, to my knowledge, has not been yet solved. The resolution of the nonlinear gyroscopic equation system Eq.(9.24) will be solved using some simplifications.

The interest for mechanical gyroscopes of spinning the rotor to measure the angular velocity has been shown in §2.2.1.a. One of the goal of this imposed spin is to sufficiently increase the term $J_z \Omega_z \dot{\phi}_x^{sf}$ bound to the angular velocity to neglect the term $J_r \ddot{\phi}_x^{sf}$ bound to the angular acceleration. This is possible for our application since the gyroscope stator will never experienced a high angular acceleration. As a matter of fact a complete rotation of the vehicle can occur within 1 second what represents an angular acceleration of about $248°/s^2$. In comparison, the term $\Omega_z \dot{\phi}_x^{sf}$ for a rotor spinning at $1'000$[rpm] (16[Hz]) will be higher by a factor 16 (equals to the spin frequency). Classically, the spin speed of mechanical gyroscope is around 10'000[rpm], what permits to neglect the terms in Eq.(9.24) bound to the vehicle angular acceleration. A good choice of the rotor shape with $J_z > J_r$ increases the impact of the angular velocity term. Neglecting the angular acceleration term Eq.(9.24) becomes:

$$J_z \Omega_z \cdot c_x^{sf} \dot{\phi}_y^{sf} = k_{i_\phi} \cdot \delta i_{\phi_x} + T_{u_x} \tag{9.25a}$$

$$-J_z \Omega_z \dot{\phi}_x^{sf} = k_{i_\phi} \cdot \delta i_{\phi_y} + T_{u_y} \tag{9.25b}$$

9.5 Summary

A linear and a non linear model of the gyroscope prototype have been developed in this chapter. They consider the forces and torques generated by the electromagnets, the unbalance effects, the gyroscopic effects and the movements of the vehicle.

Based on the linear model of the electromagnetic forces, an angular velocity measurement method considering the non linear behavior of the gyroscopic effects has been proposed. This measurement method will be evaluated in Chapter 11.

Chapter 10

Control of the AMB based Gyroscope

10.1 Control Method

The couplings due to the gyroscopic effect (see Eq.(2.3)) and to the radial actuator configuration with six electromagnets (see 9.1.1.b) imply that the different rotor coordinates cannot be treated as independent from each other but as a whole. Therefore MIMO control seems to be mandatory in our case [Sko96].

Second, in normal use, the rotor will obviously be first levitated and then accelerated until it reaches its operating rotating speed. This induces that a close to reality plant model should evolve with the rotor speed and thus strongly differs between its behavior with the rotor at stand still and its comportment as it rotates at its operating speed. This major uncertainty on the model naturally leads us to opt for robust control as according to [Sko96]: "*a control system is called robust if it is insensitive to differences between the actual system and the model of the system which was used to design the controller.*".

This robust controller will be synthesized based on the linear model developed in Chapter 9. This model-based controller permits to estimate through a state space model of the system its actual state, and thus to realize a state feedback. By nature, a model always contains errors due to uncertainties on the model parameters, unmodeled dynamics or hidden nonlinearities of the plant. Thus, how can one ensure that a model-based controller works for the actual system? This question is the starting point of robust control theory. In the particular case of H_∞ robust control theory, the ambition is to develop a controller that can stabilize the actual system within predefined specifications of the worst case uncertainty.

10.2 Loop Shaping of Closed-Loop Transfer Functions

Usually, loop shaping consists in the study of the magnitude of the transfer function $L = GK$ over frequency, G being the transfer function of the system to control and K the controller transfer function. For perfect control, we would like to have the measured signal y to be as close to the reference signal r as possible (see Fig.(D.1)).

$$y_m = (I + L)^{-1} L \cdot r + (I + L)^{-1} G \cdot d + (I + L)^{-1} L \cdot n \approx 1 \cdot r + 0 \cdot d + 0 \cdot n \quad (10.1)$$

The tracking performance condition requires $\|L\| \gg 1$ over the whole frequency domain. On the opposite, $\|L\| \ll 1$ so that the influence of the noise on the loop is kept as low as possible. Therefore, the design of the controller K is a compromise between these two mentioned requirements.
Fortunately, the conflicts between these objectives are generally in different frequency ranges and this compromise can be found with $\|L\| > 1$ for low frequencies and $\| L \| < 1$ for the highest ones.

This last approach, often called *open loop shaping*, is insufficient due to the the relation between the sensitivity function S and the complementary sensitivity function T (their mathematical expressions are given in Table(D.1)):

$$\|S + T\| = 1$$

Hence, there is no problem when $\|L\| \gg 1$ and $\|L\| \ll 1$, on the opposite there exists a grey zone where $\|L\|$ is close to one. If, in this zone, the phase of L becomes $-180°$ then $\|S\|$ and $\|T\|$ can experience high overshoot. The idea of *closed loop shaping* in order to avoid this problem is to design the controller based on a predesign of the shape of $\|S\|$ and $\|T\|$.

This predesign can be done with the help of weights placed on the exogenous inputs as well as on the regulated outputs can be weighted (see Fig.(10.1)). These weights consist in transfer functions $W_w(s)$ and $W_z(s)$ whose singular values reflect the inverse of the singular values desired in the loop shaping.

The design of the loop using weights is well treated by robust control, particularly H_∞ control permits a good physical representation of the manner to satisfy the requirements imposed by a particular application (see §10.3.2).

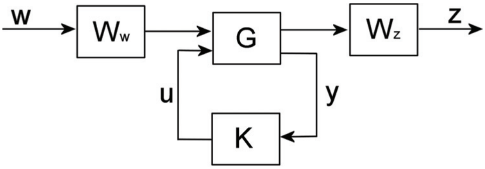

Figure 10.1: Generalized with weighting functions. The exogenous inputs w are weighted by W_w, the regulated outputs z by W_z. u represents the command signals and y the controller inputs.

10.3 Introduction to Robust Control

10.3.1 Representing Uncertainty

As mentioned in section §(10.1), a H_∞ controller is developed based on a linear model of a plant that contains some uncertainties. Uncertainties are distributed into *structured* and *unstructured* uncertainty.

10.3.1.a Structured Uncertainty

In this case, the structure of the plant and the uncertainty to be described are well-known. This uncertainty often concerns uncertain gains, time constants... On that purpose, this type of uncertainty is also often referred as *parametric*.

The structured uncertainty can be composed of three different elements: repeated scalar matrices, repeated scalar complex matrices, full complex matrices. R is the number of real matrices, S the number of scalar complex matrices and F the number of full complex matrices. The dimensions of the single matrices are $r_1, ..., r_R$, $s_1, ..., s_S$ and $f_1, ..., f_F$. Using these notations yields the following definition:

$$\text{Structured uncertainty:} \begin{cases} \Delta^s \subset \mathbb{C}^{n_w \times n_z} \\ \\ \Delta^s = \operatorname{diag}\left(\delta_1^r I_{r_1}, ..., \delta_R^r I_{r_R}, \delta_1^c I_{s_1}, ..., \delta_S^c I_{s_S}, \Delta_1, ..., \Delta_F\right) \\ \\ \delta_i^r \in \mathbb{R},\ \delta_i^c \in \mathbb{C} \text{ and } \Delta_i \in \mathbb{C}^{f_i \times f_i} \end{cases} \tag{10.2}$$

Due to its structure, some off-diagonal elements of Δ^s are zero. Therefore, structured uncertainty is a less conservative approach than unstructured uncertainty. Yet, modeling the plant using structured uncertainty implicates the minimization of the structured singular value μ and thus to use μ-synthesis for controller design what it is a more complicated strategy. It is also very difficult to exactly quantify the uncertainties of a real plant.

10.3.1.b Unstructured Uncertainty

This kind of uncertainty will always affect the chosen model as it covers unmodeled dynamics (for example hidden dynamics or high frequency dynamics that are excited in the application) as well as uncertain system poles or zeros [Chr96].

A formal definition of such uncertainties is the use of any "full" complex perturbation matrices Δ that satisfies:

$$\forall\, \omega, \quad \bar{\sigma}\left(\Delta\left(j\omega\right)\right) < b_u(\omega) \tag{10.3}$$

With ω the frequency, $\bar{\sigma}$ the upper singular value and $b_u(\omega)$ the pertubation matrix upper bound.

Because of its more general expression (see Eq.10.3), the unstructured uncertainty is more conservative than the structured one. Moreover, the loop shaping aspect will be mainly examined in our application and H_∞ can very well handle this. These two reasons lead us to focus along this thesis on unstructured uncertainty.

10.3.2 The H_∞ Problem

Along this section, we will consider the system described in Fig.(10.2). This system is made out of the controller K and of the plant P which is called the *augmented plant*. P includes the general plant G as well as the weights W_w and W_z (see Fig.(10.1)) designed in order to assign the closed loop performance of the system.

In general, the computation of a standard form H_∞ controller (Fig.(10.2)) can be reduced first to a problem of stabilization of the closed loop system and of perturbation rejection, and second to a minimization problem.

As the maximal value between the energies of the output $z(t)$ and input $w(t)$ signals are represented by the H_∞ norm (see §D.4.2), its minimization is required to optimize both the perturbation rejection and the trajectory tracking.

10.3.2.a The Optimal H_∞ Problem

The so called optimal H_∞ problem consists in the synthesis of a control law $u = K{\cdot}y$, that, among all controllers K that can internally stabilize the system, minimizes the

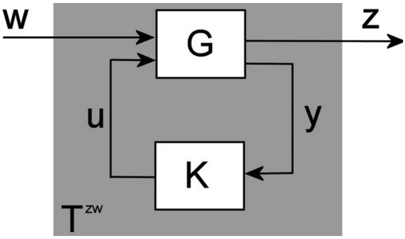

Figure 10.2: Lower LFT standard form. w represents the exogenous inputs, z the regulated outputs, u the command signals, y the controller inputs and T^{zw} the transfer function from w to z.

H_∞ norm of the transfer function $F_l\left(P(s), K(s)\right)$, i.e. $\|F_l\left(P(s), K(s)\right)\|_\infty$, between the exogenous inputs w and the regulated outputs z. The transfer function from w to z is designated by T^{zw} (see Fig.(10.2)).

The optimal H_∞ problem can be summarized as:

$$\text{Find } K \text{ so that: } \begin{cases} \text{(i) } T^{zw} = F_l\left(P(s), K(s)\right) \text{ is stable.} \\ \\ \text{(ii) } \|T^{zw}\|_\infty = \|F_l\left(P(s), K(s)\right)\|_\infty \text{ is minimal.} \end{cases} \tag{10.4}$$

The minimization goal of $\|T^{zw}\|_\infty$ (point (ii) of Eq.(10.4)) is to increase the maximal uncertainty Δ that the plant can admit. As a matter of fact, the closed loop system represented in Fig.(10.3) and composed of the control loop plus the unstructured uncertainty Δ can be written as:

$$(I - T^{zw}\Delta)^{-1} \tag{10.5}$$

Under the assumption that both T^{zw} and Δ are stable, system described in Eq.(10.5) is stable if (*Small Gain Theorem*):

$$\|T^{zw}\Delta\|_\infty < 1 \;\Rightarrow \bar{\sigma}\left(T^{zw}\right) < \frac{1}{\bar{\sigma}\left(\Delta\right)} = \frac{1}{b_u(\omega)} \tag{10.6}$$

10.3.2.b The Suboptimal H_∞ Problem

A second formulation of the H_∞ problem, called *suboptimal*, does not consist in minimizing $\|T^{zw}\|_\infty$ but in first choosing the maximal admissible uncertainty $b_u(\omega)$

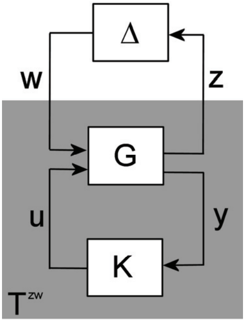

Figure 10.3: Control system with unstructured uncertainty Δ.

(see Eq.(10.3)) and then to find a controller K such that $\|F_l\left(P(s), K(s)\right)\|_\infty < \gamma$.

The suboptimal H_∞ problem can be summarized as:

$$\text{For a given } \gamma \in \mathbb{R}^+ \ / \ \|\Delta(\omega)\|_\infty \leq \frac{1}{\gamma}, \text{ find } K \ / \ \|F_l\left(P(s), K(s)\right)\|_\infty < \gamma \tag{10.7}$$

However the loop design using the optimal H_∞ problem is more conservative than the one using the suboptimal H_∞ problem, only this last one will be considered along this thesis due to its easier computation. Therefore, the denomination *H_∞ problem* will designate the suboptimal H_∞ problem.

10.3.2.c Resolution of the H_∞ Problem with the Riccati Equations

Many resolution methods ([Doy89], [Gah94], [Zho95]) exist for the H_∞ problem. For the time being and for the resolution of important size problem, the resolution proposed in [Doy89], which is based on a state space variable approach, seems to be one of the best adapted from a numerical point of view and will, therefore, be used throughout this work.

10.3.2.c.i) State Space Representation of the Augmented Plant

The previously mentioned augmented plant (see §10.3.2) can be represented as:

$$\left[\begin{array}{c} \dot{x} \\ \hline z \\ y \end{array}\right] = \left[\begin{array}{c|cc} A & B_1 & B_2 \\ \hline C_1 & D_{11} & D_{12} \\ C_2 & D_{21} & D_{22} \end{array}\right] \left[\begin{array}{c} x \\ \hline w \\ u \end{array}\right] \tag{10.8}$$

The augmented plant has the following dimensions:

- m_1 the number of exogenous inputs w.
- p_1 the number of regulated outputs z.
- m_2 the number of command signals u.
- p_2 the number of measurement signals y.
- n the dimension of the state vector of P.

10.3.2.c.ii) Assumptions

The resolution of the problem, with the method of [Doy89], is possible only under the following three assumptions:

H$_1$: (A, B_2, C_2) is stabilizable and detectable[1].

H$_2$: $\text{rank}(D_{12}) = m_2$ and $\text{rank}(D_{21}) = {p_2}^2$.

H$_3$: $\begin{bmatrix} A - j\omega I & B_2 \\ C_1 & D_12 \end{bmatrix}$ and $\begin{bmatrix} A - j\omega I & B_1 \\ C_2 & D_21 \end{bmatrix}$ have full row rank for all ω^3.

Two unnecessary assumptions for H$_\infty$ ([Sko96]) are made to get a proper P_{11} and a strictly proper P_{22}:

H$_4$: $\bar{\sigma}(D_{11}) < \gamma$

H$_5$: $D_{22} = 0$

10.3.2.c.iii) General H$_\infty$ Algorithm

If all the assumptions $\mathbf{H}_1$ to $\mathbf{H}_5$ are fulfilled, then there exists a controller K that ensures $\|F_l\left(P(s), K(s)\right)\|_\infty < \gamma$ and internally stabilizes the system if and only if the Riccati equations Eq.(10.9a) and Eq.(10.9b) respectively admit X_∞ and Y_∞ as solutions and that these solutions verify Eq.(10.9c).

$$A^T X + XA + X\left(\gamma^{-2} B_1 B_1^T - B_2 B_2^T\right) X + C_1^T C_1 = 0, \tag{10.9a}$$

$$AY + YA^T + Y\left(\gamma^{-2} C_1^T C_1 - C_2^T C_2\right) Y + B_1 B_1^T = 0, \tag{10.9b}$$

$$X_\infty \geq 0 \quad Y_\infty \geq 0 \quad \text{and } \rho\left(X_\infty Y_\infty\right) < \gamma^2. \tag{10.9c}$$

---

[1] Required for the existence of controllers K.

[2] Sufficient to ensure the controllers to be proper and thus realizable.

[3] Guarantee that the solution of the Riccati is not destabilizing the closed-loop system.

A dichotomy scheme is used to find an optimal γ. The existence of a solution $K(s)$ for the definite γ is tested at each iteration step. Algorithms to find the existing solutions are often already implemented within functions proposed in mathematical softwares such as Matlab. Therefore, we can focus on the choice of the weighting scheme and of the weighting functions in order to design the closed loop transfer function of the system. This will be the topic of the next section.

10.3.3 The Weighted H_∞ Synthesis

In this section, we will consider the augmented plant $P(s)$ as defined in §10.3.2, i.e. the general plant $G(s)$ combined with the weights $W_w(s)$ on the exogenous inputs and $W_z(s)$ the weights on the regulated outputs (see Fig.(10.1)).

These weights can be described as diagonal matrices acting on chosen exogenous inputs and/or regulated outputs:

$$W_w(s) = \begin{bmatrix} W_{w_1}(s) & & \emptyset \\ & \ddots & \\ \emptyset & & W_{w_m}(s) \end{bmatrix} \text{ and } W_z(s) = \begin{bmatrix} W_{z_1}(s) & & \emptyset \\ & \ddots & \\ \emptyset & & W_{z_p}(s) \end{bmatrix} \tag{10.10}$$

If $\|W_z(s)T_{zw}(s)W_e(s)\|_\infty \leq \gamma$ then:

$$\begin{gathered} \forall \omega \in \mathbb{R},\ \forall i \in [1; m] \text{ and } \forall j \in [1; p], \\ |W_{z_j}(j\omega)T_{z_jw_i}(j\omega)W_{w_i}(j\omega)| \leq \gamma \Leftrightarrow |T_{z_jw_i}(j\omega)| \leq \frac{\gamma}{|W_{z_j}(j\omega)W_{w_i}(j\omega)|} \end{gathered} \tag{10.11}$$

The inequality described in Eq.(10.11) property permits to see these weights as calibrators over the frequency domain for the SISO systems $T_{z_jw_i}(s)$. This approach is called *mixed sensitivity H_∞ synthesis.*

The following sections, that consist in a presentation of the existing weighting schemes, will use some notations based on Fig.(10.4) and that are introduced to get shorter expressions of the transfer functions (see Tab.(10.1)).

The different variables represented in Fig.(10.4) are described as follows:

- r represents the reference signal set by the user.
- y consists in the measurable plant outputs including the noise d in the measurement of the plant outputs.
- $e = r - y$ is the error between the reference signal and the measurable plant outputs.

Sensitivity at the system output	$T_{er} = T_{yd} = (I + GK)^{-1} = S_e$
Sensitivity at the system input	$T_{uv} = (I + KG)^{-1} = S_u$
Complementary sensitivity at the system output	$T_{yr} = GKS_e = I - S_e = T_e$
Complementary sensitivity at the system input	$-T_{\bar{u}v} = KGS_u = I - S_u = T_u$

Table 10.1: Transfer function notations for the weighting schemes.

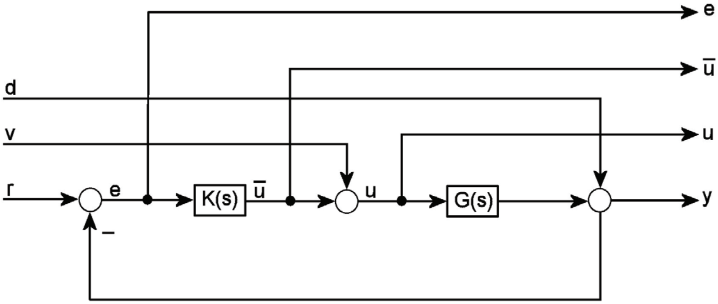

Figure 10.4: Input output notations for the weighting schemes.

- $\bar{u}$ represents the output of the controller also called control signal.
- v represents the disturbances that affect the control signal.
- $u = \bar{u} + v$ describes the actual signal that feeds the plant, i.e. the control signal after the adjunction of the disturbances v.
- d represents the noise affecting the measurements of the plant output.

The following table shows how some of the previously listed variables are linked to the physical data of the gyroscope prototype developed in §9:

In most cases, a H$_\infty$ synthesis, that is directly computed from the model, i.e. without the use of any weight, does not enable to reach satisfactory performances in

variable	physical data	vector size
r	reference position and attitude of the rotor	5×1
y	measured position and attitude of the rotor	5×1
$\bar{u}$	currents of the different electromagnet coils	8×1

Table 10.2: List of the controller variables bound to the meaningful physical data of the gyroscope prototype.

trajectory tracking, perturbation rejection and in robustness with respect to model uncertainties.

Therefore, the user imposes, with the help of the calibrators (i.e. the weights), the desired shape of the singular values of the different transfer functions, such as the sensitivity, the complementary sensitivity, the transmission of the perturbations on the outputs... Different weighting strategies will be described in the next sections.

10.3.3.a Weighting of the Outputs: The S/KS/T Weighting Scheme

A very well known weighting method is the *mixed sensitivity* method or S/KS/T which is represented on Fig.(10.5). In this method, the sensitivity S_e, the complementary sensitivity T_e and the transfer function KS_e from the input r to the output u are respectively weighted by $W_e(s)$, $W_y(s)$ and $W_u(s)$. $W_u(s)$ can be chosen as a constant or to prevent the command to include high amplitude signals what can be useful if the command signal is limited by a saturation.

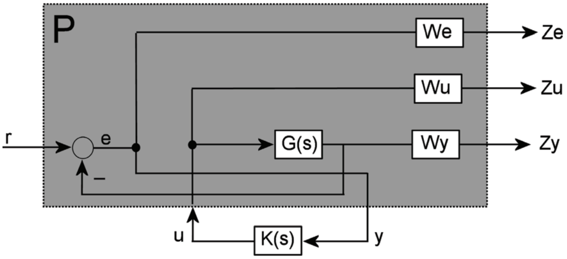

Figure 10.5: Mixed sensitivity weighting scheme.

The closed-loop transfer function T_{zw} is:

$$T_{zw} = \begin{bmatrix} W_e S_e \\ W_u K S_e \\ W_y T_e \end{bmatrix} \tag{10.12}$$

This weighting scheme is intuitive as to satisfy Eq.(10.11), we can choose:

$$W_e \approx \frac{1}{S_e},\ W_y \approx \frac{1}{T_e} \text{ and } W_u \text{ a small constant.}$$

Hence, W_e is chosen so that the low frequency perturbations are rejected (W_e has a high gain in this frequency range) and to reduce the static error (integration behavior).

The weight W_y is not always included in the weighting scheme, but it may be necessary to increase the high frequency roll-off of T_e.

The S/KS/T synthesis presents two important drawbacks:

- the sensitivity and the complementary sensitivity are separately shaped. But, these two are bound by the relationship $S+T=I$, and therefore this synthesis method presents a lot of constraints such as the *the waterbed effect* [Sko96].
- often, one cannot accept the inverse of the plant to be included in the controller. As a matter of fact, this inversion implies a slower response if the poles and zeros are closed to the imaginary axis and where the latter ones are imprecise due to the uncertainty affecting the plant.

Because of these disadvantages, the S/KS/T method will not be used in this thesis.

10.3.3.b The Plant Non-Inverting GS/T Weighting Scheme

To cope with the transient response problem of the S/KS/T synthesis, [Chr96] introduced the GS/T method that is based on the use of weights at the system input what is a very well suited strategy for ill-conditioned plants. To avoid the inverse of the plant to be in the controller, the idea is to include the plant itself inside the weighting of the sensitivity function. On that purpose, the reference signal r is waited instead of the error signal e (see Fig.(10.6)).

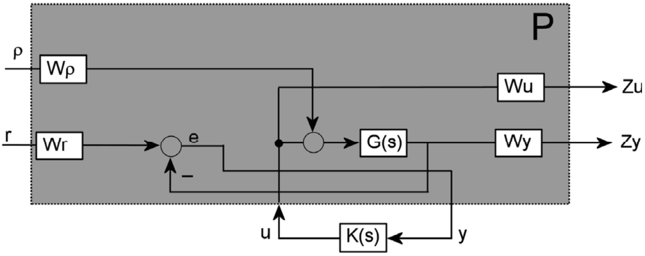

Figure 10.6: The GS/T weighting scheme.

Thus, the closed loop transfer function of T_{zw} becomes:

$$T_{zw} = \begin{bmatrix} -W_u T_u W_\rho & W_u S_u K W_r \\ W_y G S_u W_\rho & W_y T_e W_r \end{bmatrix} \tag{10.13}$$

The weight W_u can be chosen as in the S/KS/T synthesis, i.e. small and constant. Hence, this choice will lead to a small first line of T_{zw} which will, therefore, barely influence the norm of T_{zw}.

Eq.(10.13) shows that the weighting scheme T_{zw} contains the plant G in the term $W_y G S_u W_\rho$ which ensures the controller not to include the inverse of the plant [Chr96].

In order to have a physical feeling about the dimensioning of the weights W_r and W_ρ, we choose $W_y = 1$. Therefore the second line of T_{zw} becomes $[GS_u W_\rho \quad T_e W_r]$. Hence, the complementary sensitivity function T_e is shaped by W_r and GS_u by W_ρ.

How can we in a more intuitive manner dimension the weight W_ρ? To do answer this question, the reader is recalled that $GS_u W_\rho = S_e G W_\rho$ and therefore W_ρ shapes the term $S_e G$. Thus, W_ρ must reflect only that part of the sensitivity S_e which is not covered by G. Theoretically, we should choose $W_y = (S_e G)^{-1}$ but only the envelope of the plant singular values is to be taken into account to prevent the controller from again including G^{-1} [Chr97] which would lead to the previously mentioned problem of transient response (see §10.3.3.a).

10.3.4 Two DOF H_∞ Controller

10.3.4.a Motivations

The main drawback of the controllers mentioned in §10.3.3.a and §10.3.3.b is that one cannot specify the perturbation rejection performance independently from the trajectory tracking one. On that purpose, a two-degree-of-freedom controller can be implemented:

$$K = [K_f \; K_b]$$

Both parts (explained in next section) of such a controller are, in the general case, separately computed. However there exist a one step synthesis procedure, which presents some advantages in comparison to the two step procedure. Both strategies will be exposed in the following sections.

10.3.4.b Different 2DOF Approaches

[Per81] showed that the properties of the sensitivity function and the properties of the transfer function from the reference to the output signal can be dissociated, if feedforward controller is used for the reference signal. The inputs e and d of this controller are respectively connected to the feedback gain K_b and to the feedforward term K_f. Both gains are dynamic. The general block diagram of the closed loop system is shown on Fig.(10.7).

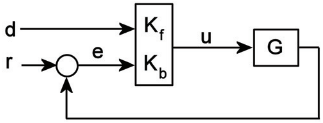

Figure 10.7: Two-degree-of-freedom H_∞ controller.

Typically, the controller is synthesized in two steps. First, the behavior of the closed loop system is optimized by K_b. Then, the trajectory tracking properties are satisfied with the design of K_f. However, both parts can be simultaneously calculated if the same design method is used.

Several authors described weighting methods for the H_∞ with a prefilter: [Chi92] proposed a two step method based on the S/KS/T weighting synthesis. One step procedures also based on the S/KS/T weighting have been proposed by [Chr94] and [Edm].

The following section exposes extensions of the previously described one and two step procedures based on the GS/T weighting scheme. These procedures are mainly inspired by [Chr96].

10.3.4.b.i) The Two-Step Procedure

In Fig.(10.7), the grey block G^{cl} represents the closed loop system in which G is stabilized by the term K_b of the controller. The expression of the transfer matrix from w to Z_y is equal to:

$$T_{z_y w} = W_y T_{yd} W_e = W_y \left(G^{cl}_{yd} + G^{cl}_{yu} K_f \right)$$

Hence, the norm of $T_{z_y w}$ can be reduced with the help of negative feed forward gain K_f. If $W_e = I$, then the shape of T_{yd} will be synthesized by the choice of W_y. The bandwidth of K_f can be set by W_u.

This two step procedure has the advantage that the synthesis of the feedforward controller is fully independent from the feedback synthesis. Hence, it can be applied to any previously stabilized closed loop system. Consequently, if K_b also contains an observer, the resulting two DOF controller $[K_f\ K_b]$ possesses at least three times as many state variables than the original system. Despite the existence of order reduction methods [Saf89], it is better not to introduce as many state variables.

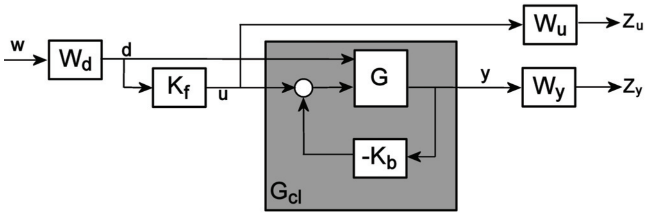

Figure 10.8: Two step procedure for the GS/T weighting scheme.

On that purpose, a one step approach of the two DOF GS/T weighting scheme synthesis is exposed in next paragraph.

10.3.4.b.ii) The One-Step Procedure

This procedure is a combination of the GS/T weighting method proposed in §10.3.3.b and of the feedforward controller synthesis presented in the previous section. This means that, for the one step procedure, the controller input does not only consists of the error e but also of the disturbance d, as represented in Fig.(10.9).

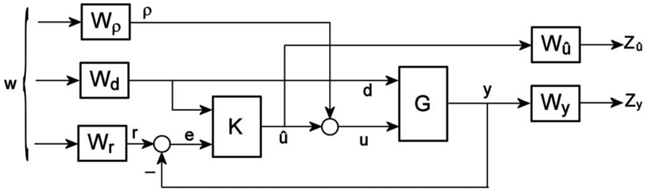

Figure 10.9: One step procedure for the GS/T weighting scheme. The controller includes a feedback and disturbance feedforward gains.

With the previously used notations $K = [K_f \; K_b]$ and $G = [G_{yd} \; G_{yu}]$, the expression of the transfer matrix T_{zw} is given by:

$$T_{zw} = \begin{bmatrix} -W_{\hat{u}} T_u W_\rho & W_{\hat{u}} \left(-S_u K_b G_{yd} - S_u K_f\right) W_d & W_{\hat{u}} S_u K_b W_r \\ W_y G_{yu} S_u W_\rho & W_y T_{yd} W_d & W_y T_e W_r \end{bmatrix} \tag{10.14}$$

$$\text{with } T_{yd} = S_e G_{yd} - G_{yu} S_u K_f$$

The first and third columns are the same as for the synthesis of the feedback alone. The first element of the second column has no important effect as long as $W_{\hat{u}}$ is small, what is most of the time the case.

The second element of the second column define the trajectory tracking properties as T_{yd} is the transfer function corresponding to this trajectory tracking.

10.3.5 H_∞ Controller with Explicit Integrator

The simulations of the nonlinear system with two-degree-of-freedom control strategy (c.f. §11.2) point out a static error in the trajectory tracking realized by the H_∞ controllers obtained with the previous synthesis methods. The H_∞ controller behaves, relatively speaking, as a proportional/derivating controller. As a matter of fact the former controller is computed around an equilibrium position and therefore cannot compensate for an additional disturbance such as in our case a movement of the vehicle.

To increase the disturbance rejection, an extension of the two-degree-of-freedom GS/T structure is introduced in this paragraph. This extension consists of the adjunction of an explicit integrator in the output feedback loop (see Fig.(10.10)). This technic is inspired from [Clé02] about time discrete systems.

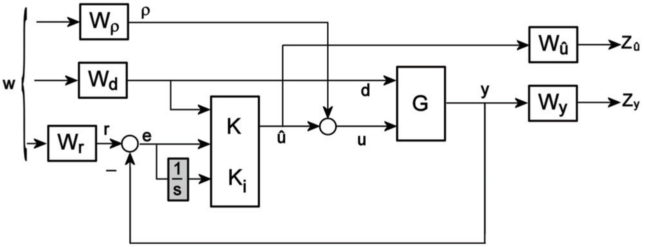

Figure 10.10: The H_∞ controller with explicit integrator (in grey).

The role of the new part K_i of the compensator $K = [K_f \ K_i \ K_b]$ is to strengthen the cancelation of the static error. Thus, the new closed loop transfer function, including the weighting filters, becomes:

$$T_{zw} = \left[\begin{array}{ccc} -W_{\hat{u}} T_u W_\rho & W_{\hat{u}} \left(-S_u K_b^\star G_{yd} - S_u K_f \right) W_d & W_{\hat{u}} S_u K_b^\star W_r \\ W_y G_{yu} S_u W_\rho & W_y T_{yd} W_d & W_y T_e W_r \end{array} \right] \tag{10.15}$$

with $K_b^\star = K_b + \frac{K_i}{s}, \ S_e = \left(I + G K_b^\star\right)^{-1}, \ T_e = S_e G K_b^\star, \ T_{yd} = S_e G K_f,$
$S_u = \left(I + K_b^\star G\right)^{-1}$ and $T_u = S_u K_b^\star$.

Here also, the controller K is synthesized with the help of the "$\gamma-$iteration" method in order to minimize the H_∞ norm of the transfer function T_{zw}. Therefore, in this case, the weighting functions W_ρ, W_r, W_d, W_y and $W_{\hat{u}}$ determine the frequency shape of the sensibility and complementary sensitivity functions S_e, T_e, T_{yd}, S_u and T_u as for the 2 DOF controller without explicit integrator using the GS/T weighting method. However, in the present case, they allow the computation of the new part K_i. As shown in Eq.(10.15), all the sensitivity expressions include this new K_i/s part of the controller. The static error cancelation is, hence, guaranteed by this explicit integrator adjunction in the case of linear systems and for constant reference trajectories, which is our case since we want to keep the rotor still within the stator reference frame. For non linear systems, in our case magnetic bearings, the static error should be diminished and should therefore guarantee that the rotor stays within a small displacement range around the point where the linear model of the plant has been derived.

10.4 Design of the H_∞ Controller

10.4.1 Control in the AMB Actuator Coordinates

Eq.9.23 proposed a linear state space model of the plant in the coordinates of the center of mass, what means that this model was based on the three positions of the center of mass plus the attitude of the rotor. However, this formulation of the problem is not intuitive because of the combination of positions and angles. Therefore, a classical method [Ble84] is to express the previously mentioned model in the coordinates of the actuators. This means that the positions of the rotor center mass and its angular attitude will be converted in five positions: the axial position of the center of mass, the X and Y coordinates of the rotor in the XY plane defined by the upper stage of radial actuators and analogously for the lower radial actuator plane. The obtained coordinate vector will be called χ_{amb}. The new description of the state space model is given by:

$$\left\{ \begin{array}{ll} \dot{\chi}_{AMB} & = A_{AMB} \cdot \chi_{AMB} + B_{AMB} \cdot \delta I_c + d_{AMB}(t) + B_u^{AMB} . \vec{F}_u \\ \\ Y_{AMB} & = [I_{55} \quad 0_{55}] \, \chi_{AMB} \end{array} \right. \tag{10.16}$$

with:

- $T_{AMB\to G}$: the transformation matrix from the AMB coordinates to the coordinates of the center of mass (see Eq.(B.8)).
- $A_{AMB} = T_{AMB\to G}^{-1} \cdot A \cdot T_{AMB\to G}$.
- $B_{AMB} = T_{AMB\to G}^{-1} \cdot B$.
- $d_{AMB}(t) = T_{AMB\to G}^{-1} \cdot \left[\begin{array}{c} 0_{51} \\ M^{-1} d(t) \end{array} \right]$.

- $B_u^{AMB} = T_{AMB\rightarrow G}^{-1} \cdot \begin{bmatrix} 0_{52} \\ M^{-1}B_u \end{bmatrix}$.

This reformulation cannot improve the control of the plant [Her91]. However, the easiness of the plant understanding is helpful to have an idea of the weighting parameters to tune in order to improve the H_∞ controller. As a matter of fact, the singular values of the plant transfer function only explain the behavior of positions regarding the frequency and not a mix of positions and torques. For this reason, the system be from now on expressed in the actuator coordinates.

10.4.2 Choice of the Weights

10.4.2.a Weights for the Standard GS/T Weighting Scheme

As proposed in section §10.3.3.b, the weight W_u is chosen small and constant, and W_y is chosen equal to the 1.
The weight W_r is used to shape the complementary sensitivity function T_e and thus permits to limit its bandwidth. Therefore W_r is designed as high pass filter crossing the $0[dB]$ line at the desired bandwidth that, in our case has been fixed at $1[kHz]$. As presented in Eq.(10.13), the sensitivity function is shaped by the function $G \cdot W_\rho$. A low order dynamics weight W_ρ has been found using a dichotomic approach combined with the linear model of the plant developed in Chapter 9.

10.4.2.b Additional Weights for the Two DOF H_∞ Controller

The two step procedure for the two-degree-of-freedom controller will not be tackled during this thesis due to the large number of state variables that it produces. Therefore, only the one-step procedure of the two-degree-of-freedom controller will be considered.
The weights W_r, W_u and W_y do not change compared to the previous design. Therefore, the weight W_ρ shapes $G_{yu}S_u$.

The main interest of the introduction of a feedforward controller is to anticipate the action of the disturbances on the rotor. In the present case, the AMB system is used as inertial sensor which is aimed to measure the vehicle movements that are the main external disturbances experienced by the gyroscope rotor. Therefore, no other device will sense the external disturbances for the gyroscope. Hence, the only disturbances that can be compensated by the feedforward have an internal origin. Based on this observation, the unbalance effects will be considered as an internal disturbance which will be anticipated with the help of the feedforward controller. Thus, the weight W_d reflects the inverse of the response of the plant to the disturbances, i.e to an approximation of the unbalance effects.

10.4.2.c Adjunction of the Explicit Integrator to the Two DOF H_∞ Controller

The synthesis principle of the explicit integrator controller does not differ from the standard two DOF H_∞ controller, since the computation is done for a gain $K_b^\star = K_b + K_i/s$ instead of K_b. Therefore the choice of the gains will not be affected by this integrator adjunction.

Based on the choice of the gains, the Bode plots of the transfer, sensitivity and complementary sensitivity functions of the plant for the axial bearings and for the radial ones are presented below.

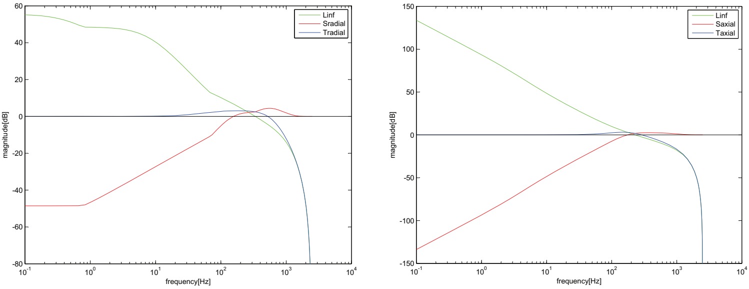

(a) (b)

Figure 10.11: Bode plots of the discrete transfer (green), sensitivity (red) and complementary sensitivity (blue) functions. The functions for the radial bearings are represented in figure (a) vertical and the axial bearings in figure (b).

10.5 Summary

Different standard weighting schemes for the synthesis of H_∞ controllers have been introduced. Based on the introduced schemes three controllers have been developed:

- a controller based on the standard GS/T weighting scheme.
- a feedforward action is added to the first controller.
- an integral action is introduced within the second controller.

These controllers will be evaluated through simulations in chapter §11.

Chapter 11

Theoretical Tests and Results

11.1 Introduction

The simulations have been run for two different orientations of the gyroscope stator (see Fig.(11.1)) because the angular velocities of interest depend from the vehicle. For example, for a plane its attitude is of main interest. On the opposite for a car, the movement that primes is its orientation in the horizontal plane. Thus, the gyroscope orientation in Fig.(11.1(a)) would be recommended for a plane or an helicopter as the gyroscope will measure the angular velocities around the X and Y axes, whereas for a car the orientation of Fig.(11.1(b)) would be wiser. The former orientation will be referred as *plane configuration* in the following, and the latter as *car configuration*.

The model chosen for the simulations is nonlinear, i.e. the forces created by the active magnetic bearings will use the form of Eq.(9.1).

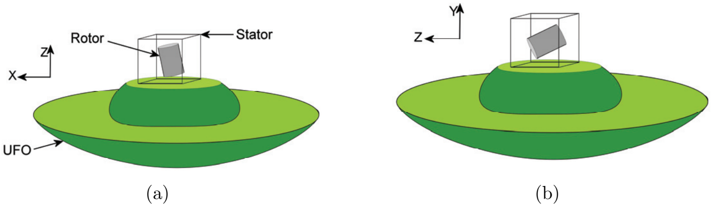

(a) (b)

Figure 11.1: Two different ways of mounting a gyroscope Unidentified Flying Object. The rotor position at stand still is (a) vertical and (b) horizontal.

In this section, the different implementations of GS/T H_∞ controllers introduced in §10 will be tested and a controller that best suits the needs of the gyroscope will be chosen.

Three types of tests will be performed to evaluate these controllers:

- Trajectory tracking with a not spun rotor: the response of the rotor to an acceleration step of $2g$ will be evaluated.
- Maximal spinning speed: the rotor spin speed will be increased until the rotor diverges. The evaluation criteria will be the maximal achieved speed. The interest of this experience is to propose a basis for further works to improve the controller.
- A third series of tests will consist in the quality of the vehicle angular velocity measurement with the mean error as criteria. A sinusoidal angular velocity profile is imposed to the vehicle. The tests are first run without external acceleration and, in a second time, with a $2g$ acceleration. The effect of the nonlinearity of Eq.(9.24) due to the cosine term will be emphasized in this chapter.

11.2 Trajectory tracking without rotor spin

The trajectory tracking without spinning the rotor permits to see the different qualities of the controllers. Fig.(11.2) shows the response of the plant to an acceleration step of $2g$ along the gyroscope stator X-axis at the time 0.25[s]. The gyroscope has also been submitted to an acceleration of $2g$ along its Y-axis, but as all the responses to this stimulation were analog, they have not been represented in this section.

As the reader can remark, Fig.(11.2) does not present the response of the plant fed by the one DOF H_∞ controller because this controller does not stand the acceleration and diverges. On that purpose, this controller is directly disqualified and will not be subject to further tests.

For concision purposes, the H_∞ controller with feedforward action but no integral action will be called non integrative controller. The other controller will be called integrative controller.

Two remarks can be made about the response of the different controllers and gyroscope configurations. First, the integral controller has a faster response and lower overshoot than the non-integrative controller. However, the difference among controllers is not so important. Second, both gyroscope configurations behave the same way along the X-axis; on the opposite, this acceleration step has an effect on the

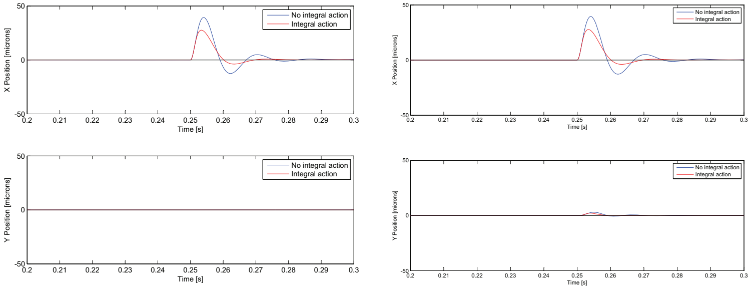

(a) (b)

Figure 11.2: Response of the plant controlled by H_∞ controllers to an acceleration of $2g$ along the gyroscope stator X-axis at the time 0.25[s]. In blue, a H_∞ controller with disturbance compensation. In red, a a H_∞ controller with disturbance compensation plus integral action. Figure (a): gyroscope *plane orientation*, figure (b): gyroscope *car orientation*. The X coordinate (resp. Y coordinate) of the rotor center of mass is represented in first row (resp. second row).

gyroscope when in its *plane configuration* and none in its *car configuration*. The reason for this is probably that in the latter orientation the X and Y axes do not have the same role and that the rotor is submitted along the Y-axis to its own weight, what is not the case in the former orientation.

11.3 Maximal Spinning Speed

Both controllers permit for both gyroscope configurations to reach the same maximal rotor spin speed which is $18.1 \cdot 10^3$ [rpm].

Before they diverge, both controllers show oscillations at the rotor spinning speed with a position amplitude of the signal of $0.3[\mu\text{m}]$ about the center of the stator and an angular velocity amplitude of $0.3[°/s]$ about the stator polar axis. These oscillations are induced by the gyroscopic part of the dynamics.

11.4 Angular Velocity Measurements

The purpose of this section is to find out how wide is the range of measurements that can be made by the gyroscope. This range is expressed in terms of angular velocity, amplitude of the vehicle attitude, frequency of the movement. During these tests the rotor will be spun at $8'000$ [rpm]. The maximum speed is not tested in order to keep sufficient disturbance margin for the measurements.

The tests will consist in exciting the plant with a sinusoidal angular velocity with predefined amplitude and frequency. We will consider that the gyroscope is placed so that the angle ϕ_x^{sf} (angle about the stator X-axis) as well as ϕ_y^{sf} can not be larger than $45[°]$. This assumption is valid for all vehicles in normal condition of use. For example, the main propeller of a helicopter cannot lift the vehicle with an angle higher than $45[°]$.

The angular velocities are tested for $100[°/s]$ and $200[°/s]$ about both X and Y axes. Hence, each series of experiments is a four-degree-of-freedom experiment plan with at least 5 tests to run per degree of freedom. Remarks and conclusions about these tests are presented below.

11.4.1 Angular Velocity Measurements: Analysis of the Mean Error

The results of all the tests performed on both gyroscope configurations and on both controllers are analog, therefore only one test has been presented in this section (see Fig.(11.3)). Some observations can be made about the simulation results. First, as shown on Fig.(11.3), there is no noticeable difference between the non integrative and integrative controllers. This is quite normal as this test only consists in sinusoids without any step that permits to show any integrative action.

Second, the gyroscope orientation plays an important role in the quality of the measurement. As a matter of fact, the quality of the measurements for the *car configuration* case is not as good as for the other configuration. Indeed, the rotor weight mostly acts, in the former case, along the gyroscope X-axis. On the opposite, in the latter case, the weight mostly works along the gyroscope Z axis. As the X axis plays a far more important role than the Z axis in the angular velocity measurement, this difference among both configurations in terms of measurement quality was predictable.

Third, the effect of the cosine presented in Eq.(9.24) can be seen for both gyroscope configurations and for both controllers. Hence, Fig.(11.3) shows that the maximal amplitude of the measurements of the angular velocities about the Y-axis increases and decreases at the frequency of the measured angular velocity about the X-axis. The results have, as expected, shown that the higher the angular velocity amplitude about the X-axis, the more critical the cosine effect on the angular velocity measurement about the Y-axis.

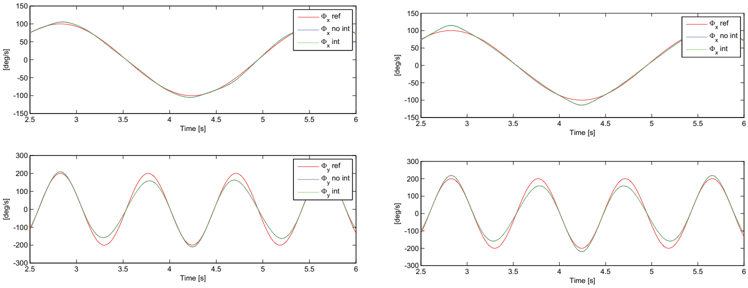

(a) (b)

Figure 11.3: Angular velocity measurement (top about the X-axis and bottom about the Y-axis). The reference angular velocity is drawn in red, the non integrative measurement in blue and the integrative one in green. Y-angular velocity= 200[°/s], amplitude of the Y angle=30[°], X-angular velocity=100[°/s], amplitude of the X angle=45[°]. Figure (a): gyroscope *plane orientation*, figure (b): gyroscope *car orientation*.

11.4.2 Effect of a 2g Acceleration on the Plant

These series have been performed under the effect of a 2g acceleration along the X and Y axes (not during the same simulation) beside the normal acceleration due to gravity. The conditions, save the 2g acceleration, are the same ones as in §11.4.1. As both gyroscope orientations and both controllers responded the same way to the 2g acceleration along the X-axis, the acceleration along the X-axis will not be further tackled in this section.

Only one simulation (see Fig.(11.4)) of the effect of 2g acceleration along the Y-axis is represented in this section as all simulations lead to analog results. In accordance with the Newton's 2^{nd} law of motion, the acceleration along the Y-axis mainly affects the measurement of the angular velocity about the X-axis (see third second in Fig.(11.4)).

Fig.(11.4) does not permit to conclude on any difference among non integrative and integrative controllers. However, the different behavior among the different gyroscope configuration can be clearly observed. When in its *car configuration*, the gyroscope is very sensitive to the imposed acceleration. Thus, one can observe on the measurements of the angular velocity about the X-axis that, for the *car configuration*, the controllers cannot fully compensate the action of the $2g$ acceleration. On the opposite, in the *plane configuration*, the controllers do not need more than a half period to regain the measurement quality without acceleration.

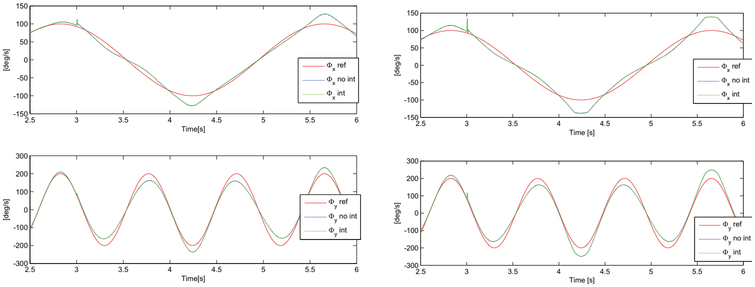

(a) (b)

Figure 11.4: Angular velocity measurement (top about the X-axis and bottom about the Y-axis). An acceleration of $2g$ is imposed along the Y-axis after 3[s] of simulation. The reference angular velocity is drawn in red, the non integrative measurement in blue and the integrative one in green. Y-angular velocity$= 200[°/s]$, amplitude of the Y angle=30[°], X-angular velocity=$100[°/s]$, amplitude of the X angle=45[°]. Figure (a): gyroscope *plane orientation*, figure (b): gyroscope *car orientation*.

11.4.3 Conclusion about the Gyroscope Tests

In this section, three GS/T based H_∞ controllers have been compared. The one-degree-of-freedom controller could not compensate an acceleration of $2g$, whereas the two DOF controllers could. These two controllers differ from a synthesis point of view only by the integral action that one possesses.

During the tests, the controller with integral action has shown a faster response and a smaller overshoot than the non integrative controller. However, the difference among both controllers is so small that the additional computation time required for the integrative controller is not worth. Therefore, the addition of an integrator to the H_∞ controller synthesized on a GS/T basis scheme will not be recommended for vehicle navigation.

The simulations have shown that the gyroscope when mounted in the *car configuration* does not present such a good measurement quality as for *plane configuration* and that it is very sensitive to external disturbances. On that purpose, only the latter configuration will be advised for vehicle navigation.

Chapter 12

Conclusions about the Cylindrical Spinning Rotor Method

The different simulations on the gyroscope model have shown that such a gyroscope should be able to acquire the vehicle angular velocity with high precision (see §11). The advantages and drawbacks of this measurement method are presented in the following sections.

12.1 Advantages

The *cylindrical spinning rotor method*, which is based on the Newton's 2^{nd} law of motion, permits an easy measurement of the angular velocity. As a matter of fact, we consider with this method that the vehicle angular velocity is proportional to the force exerted by the magnetic bearings on the rotor. Moreover, this proportionality prevents from introducing noise in the measurement through a derivation of the position as it was the case for the *ball orbit observation method.*

Another advantage of the *cylindrical spinning rotor method* coming the Newton's 2^{nd} law of motion is that the accelerations of the vehicle do not interfere in the angular velocity measurement.

Finally, as the rotor is levitated by the magnetic bearings, it reaches high spinning speeds synonymous of high rotor moment of inertia, which is directly related to a higher sensitivity of the gyroscope.

12.2 Drawbacks

As presented in Chapter 8, the rotor is driven by ten magnetic bearings. Its position and its attitude are measured by nine sensors. Considering the volume required by the actuators, the sensors and the rotor itself, one can directly conclude that a miniaturization of the prototype within a cube of less than 40[mm] side length will be very difficult.

The use of six AMB to control the rotor attitude introduces a coupled action of the AMB on the rotor. An elaborated control strategy has been required to cope with this coupling problem.

Chapter 13

Conclusion

13.1 Summary

An overview of the nowadays existing gyroscopes highlighted the fact that such devices combining high precision in the angular velocity measurement, miniaturization and low cost are not yet available, what prevents gyroscopes from being used for the navigation of civil vehicles. This thesis proposes to apply the active magnetic bearing technology to gyroscopic sensing in order to meet the challenge offered by the three previously mentioned limitations.
The challenging objective of integrating the active magnetic bearing system within a cube of 40[mm] of ridge length offered the possibility to conceive two gyroscope prototypes, each relying on a different method to measure the vehicle angular velocity.

The first method, referred as *ball orbit observation*, consists in levitating a ball shaped rotor and to have it follow a trajectory, in this case a circular orbit but it could be a sinusoid along one single axis. The vehicle angular velocity is then computed from the measurement of the inclination of the said orbit. Thus, only the position of the rotor in space needs to be controlled what permits an easy prototype design and prevents from any coupling in the electromagnet actions.
In this prototype, the uncertainties due to the non linearities of the magnetic bearings are compensated by regulating the rotor levitation with a model-reference adaptive controller. The idea of such a controller is, by means of an adaption law, to adjust in real time the reference signal feeding the controller (in this case a PID controller) so that the output of the actual plant corresponds to the output of a reference model.
Experimental tests run on this prototype demonstrated the feasibility of this measurement method and validated the adaptive controller choice. However, this method shows some drawbacks; among other, the cross sensitivity of the accel-

eration and angular velocity, the derivation of the attitude angle that increases the measurement noise...

To cope with these inconveniences, a second measurement method, called *cylindrical spinning rotor*, which is based on the Newton's 2^{nd} law of motion has been studied in the present work. Due to the integration objective of the active magnetic bearing system within a cube of 40[mm] of ridge length, a prototype has been conceived based on a trade off between the ability of the gyroscope to measure the vehicle movements within a certain predefined range and the complexity of the designed device control. Indeed, due to its geometry, the presented prototype shows a strong coupling between the action of the forces exerted by the radial electromagnets on the rotor. A linear and a non linear model of the plant expressing the force mutual influence have been developed.
Because of its ability to overcome such couplings and to counteract the plant nonlinear uncertainties, H_∞ robust control has been chosen to drive the plant. Three H_∞ compensators based on GS/T design have been synthesized using the plant linear model. The first controller consists in the basic GS/T controller synthesis scheme. The second controller introduced a feed forward controller whose input is the torques and forces due to the rotor unbalance effects. Finally, the third controller, adds an explicit integrator to the second controller. This explicit integrator H_∞ controller is, to our knowledge, for the first time used to drive active magnetic bearings.
The quality of the angular velocity measurement provided by the three H_∞ controllers has been tested during simulations run on the nonlinear model which also comprises a nonlinear behavior due to the gyroscopic effects. The simulations have shown that both H_∞ controllers including a feed forward can provide an equivalent quality of measurement of the angular velocity. Therefore, only the H_∞ compensator with feed forward but without integral part is advised to be implemented on the real gyroscope.

13.2 Outlook

This thesis is, in our knowledge, the first study reporting the use of miniaturized active magnetic bearings for gyroscope sensing and the application, in the AMB field, of a two-degree-of-freedom H_∞ controller including an explicit integrator. In addition to this, a new method to measure the angular velocity has been developed in this work. Therefore, several axes of research remain to explore. Thus, future studies based on the *ball orbit observation* method should investigate other rotor geometries, such as cylindrical rotors or rotors with a non magnetic unbalance.

For the *cylindrical spinning rotor* method, possible research works could propose:

- a miniaturization of the rotor position sensing system in order to give more space to the electromagnets, which would permit to increase the number of actuators. This would result in the decoupling the radial forces what would improve the quality of the control. This would also allow to add an electromagnet arrangement specifically dedicated to the asynchronous motor function.
- for more accuracy, the measurement of the angular velocity which is currently based on the linear model of the magnetic force should use a non linear model of this force.
- an algorithm, that would compute the nonlinear behavior of the gyroscopic effects in order to improve the quality of the angular velocity measurements, should be developed.
- the measurement of the vehicle three-degree-of-freedom acceleration should be included in order for the presented prototype to behave as a five-degree-of-freedom inertial measurement unit.

Part IV

Appendices

Appendix A

Kinematics

The notations used in §2.1 will be used throughout this chapter. Please refer to Fig.(2.2) for the order of the rotations that is crucial when considering Euler angles as the rotations in space are not commutative.

As a remembering from §2.1, three reference systems have been introduced:

- (O,x_f, y_f, z_f): the fix reference frame.
- (S,x_s, y_s, z_s): the reference frame bound to the stator.
- (G,x_r, y_r, z_r): the reference frame bound to the rotor.

In this chapter, we assume that the control of the rotor is stiff enough to allow for the small angle approximation for ϕ_x^{rs} and ϕ_y^{rs}. We will also consider that the spin speed Ω_z of the rotor is constantly directed around the axis z_r.

Along this chapter, the following notations will be used:

$$\begin{array}{ll} c_x = \cos\left(\phi_x^{sf} + \phi_x^{rs}\right) & s_x = \sin\left(\phi_x^{sf} + \phi_x^{rs}\right) \\ c_x^{rs} = \cos\left(\phi_x^{rs}\right) & s_x^{rs} = \sin\left(\phi_x^{rs}\right) \\ c_x^{sf} = \cos\left(\phi_x^{sf}\right) & s_x^{sf} = \sin\left(\phi_x^{sf}\right) \end{array}$$

A.1 Expression of the Rotor Angular Momentum in the Rotor Reference Frame

A.1.1 Angular Velocity of (G,x_r, y_r, z_r) relatively to (O,x_f, y_f, z_f)

The angular velocity of (G,x_r, y_r, z_r) relatively to (O,x_f, y_f, z_f) is:

$$\vec{\omega}_{rf} = \left(\dot{\phi}_y^{sf} + \dot{\phi}_y^{rs}\right) \cdot \vec{y}_f + \left(\dot{\phi}_x^{sf} + \dot{\phi}_x^{rs}\right) \cdot \vec{x}_r = \begin{bmatrix} \dot{\phi}_x^{sf} + \dot{\phi}_x^{rs} \\ \left(\dot{\phi}_y^{sf} + \dot{\phi}_y^{rs}\right) \cdot c_x \\ -\left(\dot{\phi}_y^{sf} + \dot{\phi}_y^{rs}\right) \cdot s_x \end{bmatrix}_r \tag{A.1}$$

A.1.2 Angular Velocity of the Rotor

The angular velocity $\vec{\omega}_{rotor}$ of the rotor expressed in the reference frame bound to the rotor is the sum of the angular velocity $\vec{\omega}_{rf}$ (see Eq.(A.1)) and of the rotor spin speed $\Omega_z \cdot \vec{z}_r$:

$$\vec{\omega}_{rotor} = \vec{\omega}_{rf} + \Omega_z \cdot \vec{z}_r = \begin{bmatrix} \dot{\phi}_x^{sf} + \dot{\phi}_x^{rs} \\ \left(\dot{\phi}_y^{sf} + \dot{\phi}_y^{rs}\right) \cdot c_x \\ -\left(\dot{\phi}_y^{sf} + \dot{\phi}_y^{rs}\right) \cdot s_x + \Omega_z \end{bmatrix}_r \tag{A.2}$$

A.1.3 Rotor Angular Momentum

The expression of the rotor angular momentum becomes with the help of Eq.(A.2) and assuming that the rotor is a perfect cylinder with radial (resp. polar) inertia J_r (resp. J_z):

$$\vec{L}_G\Big|_r = \begin{bmatrix} J_r \cdot \left(\dot{\phi}_x^{sf} + \dot{\phi}_x^{rs}\right) \\ J_r \cdot \left(\dot{\phi}_y^{sf} + \dot{\phi}_y^{rs}\right) \cdot c_x \\ J_z \cdot \left[-\left(\dot{\phi}_y^{sf} + \dot{\phi}_y^{rs}\right) \cdot s_x + \Omega_z\right] \end{bmatrix}_r \tag{A.3}$$

A.2 Derivation of the Angular Momentum in the Rotor Reference Frame

The computation of the derivative of the angular momentum will be done using the Newton's second law of motion (see Eq.(2.2)).

A.2.1 Derivation of the Rotor Angular Momentum Relatively to the Rotor Reference Frame

The first step when using Eq.(2.2) consists in deriving the rotor angular momentum relatively to the rotor reference frame. The following equations do not present the coordinates of the computed vectors along the Z-axis as they are of no interest for the present work.

$$\left.\frac{d\vec{L}_G}{dt}\right|_r = \begin{bmatrix} J_r \cdot \left(\ddot{\phi}_x^{sf} + \ddot{\phi}_x^{rs}\right) \\ \\ J_r \cdot \left[\left(\ddot{\phi}_y^{sf} + \ddot{\phi}_y^{rs}\right) \cdot c_x - s_x \cdot \left(\dot{\phi}_y^{sf} + \dot{\phi}_y^{rs}\right) \cdot \left(\dot{\phi}_x^{sf} + \dot{\phi}_x^{rs}\right)\right] \end{bmatrix}_r \tag{A.4}$$

A.2.2 Computation of the Cross Product of the Newton's 2^{nd} Law of Motion

The second step to get the derivative of the rotor angular momentum consists in computing the cross product between the angular velocity of the rotor reference frame (see Eq.(A.1)) and the rotor angular momentum (see Eq.(A.3)).

$$\begin{aligned} \vec{\omega}_{rf} \times \left.\vec{L}_G\right|_r = \; & J_r \begin{bmatrix} c_x \cdot s_x \cdot \left(\dot{\phi}_y^{sf} + \dot{\phi}_y^{rs}\right)^2 \\ -s_x \cdot \left(\dot{\phi}_y^{sf} + \dot{\phi}_y^{rs}\right) \cdot \left(\dot{\phi}_x^{sf} + \dot{\phi}_x^{rs}\right) \end{bmatrix} \\ & + J_z \begin{bmatrix} -c_x \cdot s_x \cdot \left(\dot{\phi}_y^{sf} + \dot{\phi}_y^{rs}\right)^2 + \Omega_z \cdot c_x \cdot \left(\dot{\phi}_y^{sf} + \dot{\phi}_y^{rs}\right) \\ s_x \cdot \left(\dot{\phi}_y^{sf} + \dot{\phi}_y^{rs}\right) \cdot \left(\dot{\phi}_x^{sf} + \dot{\phi}_x^{rs}\right) - \Omega_z \cdot \left(\dot{\phi}_x^{sf} + \dot{\phi}_x^{rs}\right) \end{bmatrix} \end{aligned} \tag{A.5}$$

A.2.3 Complete expression of the Derivative of the Rotor Angular Momentum

The expression of the derivative of the rotor angular momentum relatively to the rotor reference frame is given by the sum of Eq.(A.4) and Eq.(A.5):

$$\begin{aligned} \frac{d\vec{L}_G}{dt} = \; & J_r \left[\begin{array}{l} \left(\ddot{\phi}_x^{sf} + \ddot{\phi}_x^{rs}\right) + c_x \cdot s_x \cdot \left(\dot{\phi}_y^{sf} + \dot{\phi}_y^{rs}\right)^2 \\ \left(\ddot{\phi}_y^{sf} + \ddot{\phi}_y^{rs}\right) \cdot c_x - 2 \cdot s_x \cdot \left(\dot{\phi}_y^{sf} + \dot{\phi}_y^{rs}\right) \cdot \left(\dot{\phi}_x^{sf} + \dot{\phi}_x^{rs}\right) \end{array} \right] \\ & + J_z \left[\begin{array}{l} -c_x \cdot s_x \cdot \left(\dot{\phi}_y^{sf} + \dot{\phi}_y^{rs}\right)^2 + \Omega_z \cdot c_x \cdot \left(\dot{\phi}_y^{sf} + \dot{\phi}_y^{rs}\right) \\ s_x \cdot \left(\dot{\phi}_y^{sf} + \dot{\phi}_y^{rs}\right) \cdot \left(\dot{\phi}_x^{sf} + \dot{\phi}_x^{rs}\right) - \Omega_z \cdot \left(\dot{\phi}_x^{sf} + \dot{\phi}_x^{rs}\right) \end{array} \right] \end{aligned} \tag{A.6}$$

Considering that the angles between the rotor and the stator stay small, Eq.(A.6) can be approximated as:

$$\begin{aligned} \frac{d\vec{L}_G}{dt} = \; & J_r \left[\begin{array}{l} \left(\ddot{\phi}_x^{sf} + \ddot{\phi}_x^{rs}\right) + c_x^{sf} \cdot s_x^{sf} \cdot \left[\left(\dot{\phi}_y^{sf}\right)^2 + 2 \cdot \dot{\phi}_y^{sf} \cdot \dot{\phi}_y^{rs}\right] \\ \left(\ddot{\phi}_y^{sf} + \ddot{\phi}_y^{rs}\right) \cdot c_x^{sf} - 2 \cdot s_x^{sf} \cdot \left(\dot{\phi}_y^{sf} \cdot \dot{\phi}_x^{sf} + \dot{\phi}_x^{sf} \cdot \dot{\phi}_y^{rs} + \dot{\phi}_y^{sf} \cdot \dot{\phi}_x^{rs}\right) \end{array} \right] \\ & + J_z \left[\begin{array}{l} -c_x^{sf} \cdot s_x^{sf} \cdot \left[\left(\dot{\phi}_y^{sf}\right)^2 + 2 \cdot \dot{\phi}_y^{sf} \cdot \dot{\phi}_y^{rs}\right] + \Omega_z \cdot c_x^{sf} \cdot \left(\dot{\phi}_y^{sf} + \dot{\phi}_y^{rs}\right) \\ s_x^{sf} \cdot \left(\dot{\phi}_y^{sf} \cdot \dot{\phi}_x^{sf} + \dot{\phi}_x^{sf} \cdot \dot{\phi}_y^{rs} + \dot{\phi}_y^{sf} \cdot \dot{\phi}_x^{rs}\right) - \Omega_z \cdot \left(\dot{\phi}_x^{sf} + \dot{\phi}_x^{rs}\right) \end{array} \right] \end{aligned} \tag{A.7}$$

Appendix B

Matrices

B.1 Mechanical Matrices

The coordinates of the rotor in the center of mass (subscript "G") coordinates:

$$X_G = [z_G,\ x_G,\ \phi_G^y,\ y_G,\ \phi_G^x]^T \tag{B.1}$$

The current vector δI_c corresponds to the currents which flow in the different electromagnet coils:

$$\delta I_c = \left[\delta i_z^{up},\ \delta i_z^{down},\ \delta i_0^{up},\ \delta i_0^{down},\ \delta i_{120}^{up},\ \delta i_{120}^{down},\ \delta i_{240}^{up},\ \delta i_{240}^{down}\right]^T \tag{B.2}$$

The AMB force tensor $\overrightarrow{FT_{amb}}$ represents the electromagnetic forces and torques applied to the rotor. Using the notations of §9.1.2.c, $\overrightarrow{FT_{amb}}$ is given by:

$$\overrightarrow{FT_{AMB}} = [F_{AMB}^z,\ F_{AMB}^x,\ T_{AMB}^y,\ F_{AMB}^y,\ T_{AMB}^x]^T \tag{B.3}$$

The mass matrix M of the rotor composed of m its mass, J_r its radial inertia:

$$M = \begin{bmatrix} m & 0 & 0 & 0 & 0 \\ 0 & m & 0 & 0 & 0 \\ 0 & 0 & J_r & 0 & 0 \\ 0 & 0 & 0 & m & 0 \\ 0 & 0 & 0 & 0 & J_r \end{bmatrix} \tag{B.4}$$

The gyroscopic matrix G^{rs} of the rotor composed of Ω_z its spin speed and J_z its axial inertia:

$$-G = \Omega_z \begin{bmatrix} 0 & 0 & 0 & 0 & 0 \\ 0 & 0 & 0 & 0 & 0 \\ 0 & 0 & 0 & 0 & J_z \\ 0 & 0 & 0 & 0 & 0 \\ 0 & 0 & -J_z & 0 & 0 \end{bmatrix} \tag{B.5}$$

The matrix K_x (called stiffness matrix) expresses the force displacement stiffness due to the AMB actuators:

$$-K_x = \begin{bmatrix} k_z & 0 & 0 & 0 & 0 \\ 0 & k_r & 0 & 0 & 0 \\ 0 & 0 & k_\phi & 0 & 0 \\ 0 & 0 & 0 & k_r & 0 \\ 0 & 0 & 0 & 0 & k_\phi \end{bmatrix} \tag{B.6}$$

The matrix K_i, called current matrix, contains the current to force proportional factors of the AMB actuators:

$$K_i = \begin{bmatrix} k_{i_z} & -k_{i_z} & 0 & 0 & 0 & 0 & 0 & 0 \\ 0 & 0 & -2k_{i_r} & -2k_{i_r} & k_{i_r} & k_{i_r} & k_{i_r} & k_{i_r} \\ 0 & 0 & 0 & 0 & \sqrt{3}k_{i_\Phi} & -\sqrt{3}k_{i_\Phi} & -\sqrt{3}k_{i_\Phi} & \sqrt{3}k_{i_\Phi} \\ 0 & 0 & 0 & 0 & -\sqrt{3}k_{i_r} & -\sqrt{3}k_{i_r} & \sqrt{3}k_{i_r} & \sqrt{3}k_{i_r} \\ 0 & 0 & -2k_{i_\Phi} & 2k_{i_\Phi} & \sqrt{3}k_{i_\Phi} & -\sqrt{3}k_{i_\Phi} & \sqrt{3}k_{i_\Phi} & -\sqrt{3}k_{i_\Phi} \end{bmatrix} \tag{B.7}$$

B.2 Transformation Matrices

The matrix $T_{AMB \to G}$ describes the transformation from the AMB coordinates to the center of mass coordinates:

$$T_{AMB \to G} = \frac{1}{2} \begin{bmatrix} 2 & 0 & 0 & 0 & 0 \\ 0 & 1 & 1 & 0 & 0 \\ 0 & 1/h_4 & -1/h_4 & 0 & 0 \\ 0 & 0 & 0 & 1 & 1 \\ 0 & 0 & 0 & -1/h_4 & 1/h_4 \end{bmatrix} \tag{B.8}$$

The matrix $T_{G \to AMB}$ describes the transformation from the center of mass coordinates to the AMB coordinates:

$$T_{G \to AMB} = \begin{bmatrix} 1 & 0 & 0 & 0 & 0 \\ 0 & 1 & h_4 & 0 & 0 \\ 0 & 1 & -h_4 & 0 & 0 \\ 0 & 0 & 0 & 1 & -h_4 \\ 0 & 0 & 0 & 1 & h_4 \end{bmatrix} \tag{B.9}$$

Appendix C

Model of the Torques Generated by the AMB Radial Actuators

The variables introduced in this section are:

- $\Delta_{r0} = b + 2(r - \rho)$.
- $S_r = 2\gamma \cdot \rho \cdot e$. S_r is the surface of one pole of a radial electromagnet. The pole shape is cylindrical section with an angular opening of 2γ (see Fig.(9.3)). e is the pole thickness but this variable will not been used any further.
- α_0 is the mean angle of an actuator, in our case it can be 0, $\frac{2\pi}{3}$ or $\frac{4\pi}{3}$ depending on the actuator.
- $h_j,\ j \in \{1; 2\}$ is the Z coordinate of the pole j.

The torque $\vec{\tau} = [\tau_x, \tau_y, \tau_z]$ exerted by a radial actuator with two identical poles placed at the height h_{r1} and h_{r2} on the rotor is proposed in Eq.(C.1).

$$\begin{aligned}
\tau_x \; = \; & \frac{ai_0^2 S_r(h_{r1}+h_{r2})}{\gamma\Delta_{r0}^2}\sin(\alpha_0)\sin(\gamma)+\frac{2ai_0 S_r(h_{r1}+h_{r2})}{\gamma\Delta_{r0}^2}\sin(\alpha_0)\sin(\gamma)\cdot\delta i \\
& +\frac{ai_0^2 S_r}{2\gamma\Delta_{r0}^3}\Big[r\Delta_{r0}\left(2\gamma-\cos(2\alpha_0)\sin(2\gamma)\right)+4\left(h_{r1}+h_{r2}\right)^2\sin(\alpha_0)\sin(\gamma)\Big]\cdot\phi_x \\
& -\frac{ai_0^2 S_r}{2\gamma\Delta_{r0}^3}\Big[r\Delta_{r0}\sin(2\alpha_0)\sin(2\gamma)+4\left(h_{r1}+h_{r2}\right)^2\sin(\alpha_0)\sin(\gamma)\Big]\cdot\phi_y \\
& -\frac{ai_0^2 S_r\left(h_{r1}+h_{r2}\right)}{\gamma\Delta_{r0}^3}\sin(2\alpha_0)\sin(2\gamma)\cdot x_G \\
& -\frac{ai_0^2 S_r\left(h_{r1}+h_{r2}\right)}{\gamma\Delta_{r0}^3}\left(2\gamma-\cos(2\alpha_0)\sin(2\gamma)\right)\cdot y_G
\end{aligned} \tag{C.1a}$$

$$\begin{aligned}
\tau_y \; = \; & \frac{-ai_0^2 S_r(h_{r1}+h_{r2})}{\gamma\Delta_{r0}^2}\cos(\alpha_0)\sin(\gamma)-\frac{2ai_0 S_r(h_{r1}+h_{r2})}{\gamma\Delta_{r0}^2}\cos(\alpha_0)\sin(\gamma)\cdot\delta i \\
& -\frac{ai_0^2 S_r}{2\gamma\Delta_{r0}^3}\Big[r\Delta_{r0}\sin(2\alpha_0)\sin(2\gamma)+4\left(h_{r1}+h_{r2}\right)^2\cos(\alpha_0)\sin(\gamma)\Big]\cdot\phi_x \\
& +\frac{ai_0^2 S_r}{2\gamma\Delta_{r0}^3}\Big[r\Delta_{r0}\left(2\gamma+\cos(2\alpha_0)\sin(2\gamma)\right)+4\left(h_{r1}+h_{r2}\right)^2\cos(\alpha_0)\sin(\gamma)\Big]\cdot\phi_y \\
& +\frac{ai_0^2 S_r\left(h_{r1}+h_{r2}\right)}{\gamma\Delta_{r0}^3}\left(2\gamma+\cos(2\alpha_0)\sin(2\gamma)\right)\cdot x_G \\
& +\frac{ai_0^2 S_r\left(h_{r1}+h_{r2}\right)}{\gamma\Delta_{r0}^3}\sin(2\alpha_0)\sin(2\gamma)\cdot y_G
\end{aligned} \tag{C.1b}$$

$$\begin{aligned}
\tau_z \; = \; & \frac{-ai_0^2 S_r\sin(\gamma)}{\gamma\Delta_{r0}^2}\left(h_{r1}+h_{r2}\right)\left[\cos(\alpha_0)\cdot\phi_x+\sin(\alpha_0)\cdot\phi_y\right] \\
& -\frac{2ai_0^2 S_r\sin(\gamma)}{\gamma\Delta_{r0}^2}\left[\sin(\alpha_0)\cdot x_G-\cos(\alpha_0)\cdot y_G\right]
\end{aligned} \tag{C.1c}$$

The prototype contains two symmetrical about the XY plane stages of radial actuators. The stages are referenced as up and down. The sum $\vec{T}$ of the torques generated by two actuators symmetrically placed about the XY plane will result for the torques T_x and T_x (resp. T_z) in a canceling of the constant term and of the effects of x_G and y_G (resp. of ϕ_x and ϕ_y). The expression of $\vec{T}$ is given by:

$$\begin{aligned}
T_x &= \frac{2ai_0S_r(h_{r1}+h_{r2})}{\gamma\Delta_{r0}^2}\sin(\alpha_0)\sin(\gamma)\cdot(\delta i_{up}-\delta i_{down}) \\
&+\frac{ai_0^2S_r}{\gamma\Delta_{r0}^3}\Big[r\Delta_{r0}\left(2\gamma-\cos(2\alpha_0)\sin(2\gamma)\right)+4\left(h_{r1}+h_{r2}\right)^2\sin(\alpha_0)\sin(\gamma)\Big]\cdot\phi_x \\
&-\frac{ai_0^2S_r}{\gamma\Delta_{r0}^3}\Big[r\Delta_{r0}\sin(2\alpha_0)\sin(2\gamma)+4\left(h_{r1}+h_{r2}\right)^2\sin(\alpha_0)\sin(\gamma)\Big]\cdot\phi_y \qquad \text{(C.2a)} \\
T_y &= -\frac{2ai_0S_r(h_{r1}+h_{r2})}{\gamma\Delta_{r0}^2}\cos(\alpha_0)\sin(\gamma)\cdot(\delta i_{up}-\delta i_{down}) \\
&-\frac{ai_0^2S_r}{\gamma\Delta_{r0}^3}\Big[r\Delta_{r0}\sin(2\alpha_0)\sin(2\gamma)+4\left(h_{r1}+h_{r2}\right)^2\cos(\alpha_0)\sin(\gamma)\Big]\cdot\phi_x \qquad \text{(C.2b)} \\
&+\frac{ai_0^2S_r}{\gamma\Delta_{r0}^3}\Big[r\Delta_{r0}\left(2\gamma+\cos(2\alpha_0)\sin(2\gamma)\right)+4\left(h_{r1}+h_{r2}\right)^2\cos(\alpha_0)\sin(\gamma)\Big]\cdot\phi_y \\
T_z &= -\frac{4ai_0^2S_r\sin(\gamma)}{\gamma\Delta_{r0}^2}\left[\sin(\alpha_0)\cdot x_G-\cos(\alpha_0)\cdot y_G\right] \qquad \text{(C.2c)}
\end{aligned}$$

Three such torques are created by the actuators placed at $\alpha_0 = 0°$, $\alpha_0 = 120°$ and $\alpha_0 = 240°$. The sum of these tree torques is given by:

$$\begin{aligned}
\sum T_x &= \frac{2ai_0S_r(h_{r1}+h_{r2})}{\gamma\Delta_{r0}^2}\sin(\gamma)\sin(\frac{2\pi}{3})\left[(\delta i_{120up}-\delta i_{120down})-(\delta i_{240up}-\delta i_{240down})\right] \\
&+\frac{6ai_0^2S_r}{\Delta_{r0}^2}\cdot r\cdot\phi_x \qquad \text{(C.3a)} \\
\sum T_y &= -\frac{2ai_0S_r(h_{r1}+h_{r2})}{\gamma\Delta_{r0}^2}\sin(\gamma)\left[(\delta i_{0up}-\delta i_{0down})\right. \\
&\left.-\frac{1}{2}\cdot(\delta i_{120up}-\delta i_{120down}+\delta i_{240up}-\delta i_{240down})\ \right] \\
&+\frac{6ai_0^2S_r}{\Delta_{r0}^2}\cdot r\cdot\phi_y \qquad \text{(C.3b)} \\
\sum T_z &= 0 \qquad \text{(C.3c)}
\end{aligned}$$

Appendix D

Matrix Theory and Norms

D.1 State Space Representation of a System

A LTI invariant system (SISO or MIMO) can be fully described by a set of linear differential equations with constant coefficients and by its initial conditions.

$$\begin{cases} \dot{x}(t) = A \cdot x(t) + B \cdot u(t) & A \in \mathbb{R}^{n\times n} \quad B \in \mathbb{R}^{n\times m} \\ y(t) = C \cdot x(t) + D \cdot u(t) & B \in \mathbb{R}^{p\times n} \quad D \in \mathbb{R}^{p\times m} \\ x(0) = x_0 \end{cases} \tag{D.1}$$

In Eq.(D.1), $x \in \mathbb{R}^n$ is the state vector, $u \in \mathbb{R}^m$ the input vector and $y \in \mathbb{R}^p$ the output vector.

A more compact notation is:

$$[y] = \left[\begin{array}{c|c} A & B \\ \hline C & D \end{array}\right] [u]$$

D.2 Frequency Domain Representation

Applying the Laplace transformation to Eq.(D.1) one gets:

$$\begin{cases} s \cdot X(s) = A \cdot X(s) + B \cdot U(s) \\ Y(s) = C \cdot X(s) + D \cdot U(s) \end{cases}$$

This leads to the matrix transfer function of the linear dynamic system G(s) defined as:

$$Y(s) = G(s) \cdot U(s) = C \cdot (s \cdot I - A)^{-1} cdot B + D$$

Loop Transfer Function	$L = GK$
Sensitivity Function	$(I + GK)^{-1} = (I + L)^{-1}$
Complementary Sensitivity	$(I + GK)^{-1} GK = (I + L)^{-1} L$

Table D.1: Transfer Functions of the Control System.

D.3 Closed Loop Transfer Functions

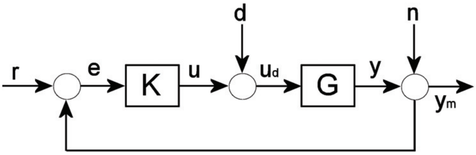

Figure D.1: General MIMO control system. K is the controller, G the plant to control, r the reference signal, d and n disturbance signals and y_m the measured signal.

The general MIMO control system presented in Fig.(D.1) has the following closed loop response:

$$y_m = (I + GK)^{-1} GK \cdot r + (I + GK)^{-1} G \cdot d \, (I + GK)^{-1} GK \cdot n$$

This equation leads to a set of notations used throughout this thesis and that are given in Tab.(D.1):

D.4 Signal and System Norms

D.4.1 Definition of a Signal Norm

The p-norm of a vector signal $u(t) = [u_i(t)]$ is a real number $\|u\|_p$ defined as:

$$\|u\|_p = \sqrt[p]{\sum_{i=0}^{n} \int_0^{\infty} |u_i(\tau)|^p d\tau}$$

D.4.2 The H_∞ Norm of a System

The norm of a system can be directly derived from the signal norm. We consider the system with a stable transfer function $G(s)$ and its input and output vector signals $U(s)$ and $Y(s)$. The H_∞ of $G(s)$ is defined as:

$$\|G\|_\infty = \sup_{\|u\|_2 \neq 0} \frac{\|y\|_2}{\|u\|_2}$$

For a matrix $G(s) \in \mathcal{H}_\infty = \{G(s)|G(s) \text{ is analytic in } Re(s) > 0, \|G(s)\|_\infty < \infty\}$ (this space is called Hardy space) we have the following identity:

$$\|G\|_\infty = \max_{Re(s)>0} \bar{\sigma}(G(s)) = \max_{\omega} \bar{\sigma}(G(j\omega))$$

The H_∞ norm of a system is the maximum over all frequencies of all its largest singular value.

D.5 Singular Values

The singular values $\sigma_1 \geq \sigma_2 \geq ... \geq \sigma_k$ ($k = min\{l, m\}$) of a matrix $A \in \mathbb{C}^{l \times m}$ are defined as the eigenvalues of the matrix $(A^*)^T \cdot A$:

$$\sigma_i = \sqrt{\lambda_i \left((A^*)^T \cdot A \right)} \quad i = 1..k$$

The maximum and minimum singular values are noted:

$$\sigma_{max}(A) = \sigma_1(A) = \bar{\sigma}(A) = \max_{d \neq 0} \frac{\|Gd\|_2}{\|d\|_2}$$

$$\sigma_{min}(A) = \sigma_k(A) = \underline{\sigma}(A) = \min_{d \neq 0} \frac{\|Gd\|_2}{\|d\|_2}$$

Hence for all vectors, the gains of the matrix A belong to the range $[\underline{\sigma}(A); \bar{\sigma}(A)]$. Therefore, the singular values have been chosen as measure of gain in the case of MIMO systems [Sko96].

Appendix E

Sensing System

E.1 Sensor Selection

The rotor center of gravity as well its attitude needs to be precisely measured within its whole displacement range. Moreover, in order to keep the advantage of a frictionless levitation the rotor must be sensed without any contact. Induction, capacitive and light based sensors combine these conditions.
Optical reflective sensors OSRAM SFH 9201 have been chosen because they provide a high sensitivity over the whole rotor displacement range [Zoe02].

E.2 Configuration Choice

In order to levitate the cylindrical rotor, the position (three DOF) of its center of gravity as well as the attitude (two DOF) of its main axis must be controlled. Therefore, at least five sensors are required. The chosen spatial configuration of the sensing system is made out of nine sensors. This redundant information will permit to mean certain signals thus increasing the measurement precision.

These nine sensors are arranged on three similar "Sensing Planes" (see fig.E.1), each plane includes two horizontal sensors (HU and HD) and one vertical sensor(V). Plane number 2 (resp. number 3) is the replica of plane number 1 by a rotation of $\frac{-\pi}{3}$ (resp. $\frac{-2\pi}{3}$) around the gyroscope main axis.

The distance measured by sensor HU is called "u", called "v" for sensor V and "d" for sensor HD. The subscripts 1,2 or 3 attached to the sensor names or measured distances tell to which sensing plane a sensor belongs.

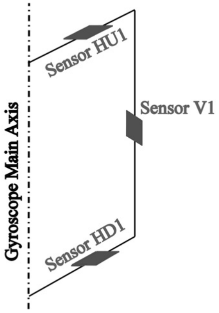

Figure E.1: Configuration of the sensing plane number 1. The sensors are represented in grey.

In the gyroscope cartesian coordinate system, the sensor coordinates are designated by the subscripts X, Y and Z.
Inside its plane, the coordinates of a sensor are its distance (subscript R) to the gyroscope main axis and its height (subscript Z) along this last axis.

Section (E.2) details the method to compute the above mentioned rotor five DOF using these sensing planes and combinations of the sensors HU_i and HD_i, $i \in [1;3]$.

E.3 Position and Angle Calculation

In a first time the rotor angles φ_x and φ_y are computed through the measurement of a unitary vector parallel to the cylinder main axis. This is done in four steps (the first two steps are repeated for the lower plane):

1. Two vectors of the upper rotor disc are computed using the measurements of the three upper horizontal sensors. The coordinates of these vectors are $(HU1_X - HU2_X, HU1_Y - HU2_Y, HU1_Z + u1_Z - HU2_Z - u2_Z)$ and $(HU3_X - HU2_X, HU3_Y - HU2_Y, HU3_Z + u3_Z - HU2_Z - u2_Z)$.
2. The cross product of these vectors is computed and divided by its norm. The result will consist in a unitary vector parallel to the cylinder main axis. This vector is called the upper cylinder main vector.
3. The mean of the upper and lower cylinder main vectors is computed to get a better approximation of the cylinder main axis.

4. The angles will then be computed using the first order Taylor series of the rotation matrix applied to the rotor main axis.

In a second time the position of the center of gravity is measured. Using the previously computed angles φ_x and φ_y, one calculates the angles φ_1, φ_2 and φ_3 corresponding to the inclination of the cylinder inside each measurement plane. The center of gravity coordinates inside a plane $i, i \in [1;3]$ are R_i and Z_i (Eq.E.1):

$$\begin{cases} R_i = & \frac{1}{2}\left[(HUi_R + HDi_R)\sin^2(\varphi_i) + 2\,(Vi_R - v_i)\cos^2(\varphi_i) \right. \\ & \qquad \left. - \,(u_i + HUi_Z - d_i - HDi_Z)\cos(\varphi_i)\sin(\varphi_i)\right] \\ & \\ Z_i = & \frac{1}{2}\left[(2Vi_R - 2v_i - HUi_R - HDi_R)\sin(\varphi_i) + (u_i + HUi_Z - d_i + HDi_Z)\cos(\varphi_i)\right] \end{cases} \tag{E.1}$$

Using the different R_i and Z_i one obtains for the coordinates of the gravity center (Eq.E.2):

$$\begin{cases} X_G = & \frac{1}{2}\left[\frac{R_1}{\cos\left(\frac{-\pi}{6}\right)} + \frac{R_3}{\cos\left(\frac{-5\pi}{6}\right)}\right] \\ & \\ Y_G = & \frac{1}{3}\left[\frac{R_1}{\sin\left(\frac{-\pi}{6}\right)} + \frac{R_2}{\sin\left(\frac{-\pi}{2}\right)} + \frac{R_3}{\sin\left(\frac{-5\pi}{6}\right)}\right] \\ & \\ Z_G = & \frac{1}{3}\left[Z_1 + Z_2 + Z_3\right] \end{cases} \tag{E.2}$$

List of Figures

2.1 Reference frames. 8
2.2 Euler angles. 9
2.3 Law of gyroscopics 11
2.4 External Gimbal Gyro 11
2.5 Dry Tuned Gyro 12
2.6 Gas Bearing Gyroscope 13
2.7 The Vibrating String Gyroscope 15
2.8 The Tuning Fork Gyro. 15
2.9 The Vibrating Cylinder Gyro. 16
2.10 Sagnac Effect 17

3.1 Passive Levitation of a Diamagnetic and a Ferromagnetic Rotor . . 19

4.1 Ball Orbit 25
4.2 Top view of the orbit described by the ball shaped rotor. $A_{(n)}$ (resp. $C_{(n)}$) represents the ball position (resp. the orbit center) at the time $t_{(n)}$. m is the number of ball position measurements per revolution. 26

5.1 Exploded view of the prototype. The ball shaped rotor is represented in green, the electromagnetic actuator coils in red and their cores in blue. 30
5.2 Magnetic Force Representation 31
5.3 Block diagram of the controller/plant system. 34
5.4 Schematics of the coil command electronics. 36
5.5 Block diagram of the system including the DA card 37
5.6 Antiwindup Feedback Structure 37

5.7 General representation of MRACs. 38
5.8 General representation of STCs. 38
5.9 Implementation of the MRAC to the AMB-Gyroscope. 40
5.10 Introduction of the control law in the MRAC. 41

6.1 Test Rig 44
6.2 Angular velocity measurement 44
6.3 Noise in the angular velocity measurement 45

8.1 Two stage repartition of the radial actuators 52
8.2 Axial actuator shape. 54
8.3 Asymmetric forces exerted by one axial electromagnet on the rotor 55
8.4 Rotor shape. 55

9.1 Single Actuator 59
9.2 Slanted Ring. 61
9.3 Single Actuator 63
9.4 First bending mode of the rotor. 70

10.1 Weighted Plant. 77
10.2 Lower LFT standard form. 79
10.3 Control system with unstructured uncertainty 80
10.4 Input output notations for the weighting schemes 83
10.5 Mixed sensitivity weighting scheme. 84
10.6 The GS/T weighting scheme. 85
10.7 The 2-DOF H_∞ controller. 87
10.8 Two step procedure for the GS/T weighting scheme 88
10.9 One step procedure for the GS/T weighting scheme 88
10.10 The H_∞ controller with explicit integrator 89
10.11 Bode plots of the transfer, sensitivity and complementary sensitivity functions 92

11.1 Gyroscope mounted on an UFO 93
11.2 Comparison among the H_∞ without rotor spin 95

11.3 Angular velocity measurement 97
11.4 Angular velocity measurement in presence of an acceleration 98

D.1 General MIMO control system 122

E.1 Sensing plane configuration 126

List of Tables

2.1 Typical performances of different types of gyroscopes. 18

6.1 Performance of AMB based gyroscope when measuring the angular velocity with the ball orbit method. 46

10.1 Transfer function notations for the weighting schemes 83
10.2 Control physical data. 83

D.1 Transfer Functions of the Control System 122

Bibliography

[AG08] Mecos Traxler AG. Applications on: *http://www.mecos.ch/en/applications/index.php*, last accessed in 2008.

[Bar08] F. Barrot. *Acceleration and inclination sensors based on magnetic levitation - Application in the particular case of structural health monitoring in civil engineering.* PhD thesis, EPFL, 1015 Lausanne, Switzerland, 2008.

[Bau97] R. Baumanna, W. Maeder, D. Glauser and R. Clavel. The pantoscope: A spherical remote-center-of-motion parallel manipulator for force reflection. In *Proceedings of the 1997 IEEE International Conference on Robotics and Automation*, pages 718–723, 1997.

[Ble84] H. Bleuler. *Decentralized Control of Magnetic Rotor Bearing System.* PhD thesis, ETHZ, Zurich, Switzerland, 1984.

[Bol05] A. Boletis. *High Speed Micromotor on a Three Axis Active Magnetic Bearing.* PhD thesis, EPFL, 1015 Lausanne, Switzerland, 2005.

[Bol07] A. Boletis, F. Barrot and R. Moser. Three axis active magnetic levitation for inertial sensing systems. Switzerland Patent US 7,252,001 B2. August, 7. 2007.

[Bry90] G. Bryan. On the beats in the vibrations of a revolving cylinder or bell. *Proc. Camb. Phil. Soc.*, VII:101–111, November 1890.

[Chi92] R. Chiang and M. Safonov. Real k_m-synthesis via generalized popov multipliers. In *Proceedings of the American Control Conference*, pages 2417–2418, 1992.

[Chr94] U. Christen, M. Weilenmann and H. Geering. Design of H_2 and H_∞ controllers with two degrees of freedom. In *Proceedings of the American Control Conference*, pages 2391–2395, 1994.

[Chr96] U. Christen. *Engineering Aspect of $H_\infty Control$.* PhD thesis, ETH, Zurich, Switzerland, 1996.

[Chr97] U. Christen and H. Geering. Inverting and noninverting H_∞*controllers*. *Systems and Control Letters*, 30:31–38, 1997.

[Clé02] B. Clément and G. Duc. Synthèse multicritère par retour de sortie: utilisation de la paramétrisation de youla et de l'optimisation lmi. In *Conception de commandes robustes*, pages 228–268. Hermès, 2002.

[Doy89] J. Doyle, K. Glover, P. Khargonekar and B. Francis. State space solutions to standard H_2 and H_∞ control problems. *IEEE Transaction on Automatic Control*, 34(8):831–847, 1989.

[Edm] J. Edmunds. Output response tuning of one- and two-degree of freedom controllers using an H_∞.

[Fas08] Fascinations. Levitron on:
http://www.levitron.com/, last accessed in 2008.

[Fou52a] L. Foucault. Sur les phénomènes d'orientation des corps tournants entrainés par un axe fixé à la surface de la terre. *Compte Rendu de l'Académie des Sciences*, 35:424, 1852.

[Fou52b] L. Foucault. Sur une nouvelle démonstration expérimentale du mouvement de la terre fondée sur la fixité du plan de rotation. *Compte Rendu de l'Académie des Sciences*, 35:421, 1852.

[Fra94] G. Franklin, J. Powell and A.Emami-Naeini. *Feedback Control of Dynamic Systems*. Mechanical Engineering Series, Addison-Wesley, Reading, 3 edition, 1994.

[Gah94] P. Gahinet. Explicit controller formulas for lmi-based H_∞ synthesis. In *Proceedings of the American Control Conference*, 1994.

[Gla02] A. Glattfelder and W. Schaufelberger. *Control Systems with Input and Output Constraints. Design and Analysis of 'Antiwindup' and 'Overrides'*. Springer, Berlin, 2002.

[Had84] M. Hadfield. Hollow rotor esg technology. *IEEE Trans. on Aerospace and Electronic Systems AES-20*, 4:414–444, 1984.

[Har83] R. Harrigan. Levitation device. US 382245. May, 03. 1983.

[Her91] R. Herzog. *Ein Beitrag zur Regelung von magnetgelagerten Systemen mittels positiv reeller Funktionen und H_∞-Optimierung*. PhD thesis, ETH, Zurich, Switzerland, 1991.

[How64] E. Howe and P. Savet. The dynamically tuned free rotor gyro. *Control Engineering*, pages 67–72, 1964.

[Hun64] G. Hunt and A. Hobbs. Development of an accurate tuning-fork gyroscope. In *Symposium on Gyros, Proc. Inst. Mech. Eng. (London)*, 1964.

[Inc08] Crossbow Technologies Inc. Datasheet of the imu700 on: *http://www.xbow.com/*, last accessed in 2008.

[Joo77] D. Joos. Comparison of typical gyro errors for strapdown applications. In *DGON Symposium Gyro Technology*, 1977.

[Kha92] H. Khalil. *Nonlinear Systems.* Macmillan Publishing Company, New York, 2 edition, 1992.

[Kie08] Kieff. Gyroscope flywheel diagram on: *http://en.wikipedia.org/wiki/Gyroscope*, last accessed in 2008.

[Law98] A. Lawrence. *Modern Inertial Technology, Navigation, Guidance, and Control.* Mechanical Engineering Series, Springer-Verlag New York, Inc., 2 edition, 1998.

[Lib08] Midi Libre. La construction vérifiée grâce au satellite on: *http://viaduc.midilibre.com/article_reportages.php?id_article=218*, last accessed in 2008.

[Lyn84] D. Lynch. Hemispherical resonator gyro. *IEEE Trans. on Aerospace and Electronic Systems*, AES-20,4:414–444, 1984.

[Mar06] Y. Maruyama, M. Takasaki, Y. Ishino, T. Mizuno, T. Ishigami and H. Kameno. Basic study on gyroscopic sensor using active magnetic bearing. In *Proc. of the 10th International Symposium on Magnetic Bearings (ISMB 10)*, 2006.

[Mos06] R. Moser, J. Sandtner, A. Schorderet, J. Giovanola and H. Bleuler. Design of very high speed friction spindle using passive magnetic bearings,. In *Proc. of the 10th International Symposium on Magnetic Bearings (ISMB 10)*, 2006.

[Mur03] T. Murakoshi, Y. Endo, K. Fukatsu, S. Nakamura and M. Esashi. Electrostatically levitated ring-shaped rotational-gyro/accelerometer. *Japanese Journal of Applied Physics*, 42:2468–2472, 2003.

[New87] I. Newton. *Philosophiae Naturalis Principia Mathematica.* Samuel Pepys, London, 1687.

[Nor96] A. Nordsieck. *Principles of the Electric Vacuum Gyroscope*, volume A54. 1996.

[Par08] A. Parsch. An/asn - airborne special/combination navigation equipment on: *http://www.designation-systems.net/usmilav/jetds/an-asn.html*, last accessed in 2008.

[Per81] L. Pernebo. An algebraic theory for the design of controllers for linear multivariable systemsŰpart ii: Feedback realizations and feedback design. *IEEE Transactions on Automatic Control,*, 26:183–194, 1981.

[Qui64] W. Quick. Theory of the vibrating string as an angular motion sensor. *Trans. ASME, Journal of Applied Mechanics*, pages 523–534, 1964.

[Rou77] E. Routh. *A Treatise on the Stability of a Given State of Motion.* Macmillan, London, 1877.

[RTR08] Railway Technical Research Institute RTRI. Overview of maglev r&d: Superconducting magnetically levitated vehicle on: *http://www.rtri.or.jp/rd/maglev/html/english/maglev_frame_E.html*, last accessed in 2008.

[Saf89] M. Safonov and R. Chiang. A schur method for balanced model reduction. *IEEE Transactions on Automatic Control*, 34:729–733, 1989.

[Sag13] G. Sagnac. Sur la preuve de la réalité de l'éther lumineux par l'expérience de l'interférographe tournant. *Compte Rendu de l'Académie des Sciences*, 95:1410–1413, 1913.

[Sch94] G. Schweitzer, H. Bleuler and A. Traxler. *Active Magnetic Bearings: Basics, Properties and Applications of Active Magnetic Bearings.* vdf Hochschulverlag an der ETHZ, Zurich, 1994.

[Sie08] Siemens and ThyssenKrupp. Transrapid international on: *http://www.transrapid.de/*, last accessed in 2008.

[Sko96] S. Skogestad and I. Postlethwaite. *Multivariable feedback Control.* John Wiley and Sons„ Chichester (UK), 1996.

[Slo91] J. Slotine. *Applied Nonlinear Control.* Prentice Hall International Inc., Upper Saddle River, New Jersey, 1991.

[Tit] D. Titterton and J. Weston. *Strapdown Inertial Navigation Technology.*

[Wan] C. Wan. *Global stabilization of nonlinear gyroscopic systems.* PhD thesis, Michigan University, Ann Arbor, Michigan.

[Wei93] M. Weinberg, J. Bernstein, S. Cho, A. King, A Kourepenis and P. Maciel. A micromachined comb-drive tuning fork rate gyroscope. In *Institute of Navigation, Proc. of the 49th Annual Meeting*, 1993.

[Wil74] P. Willems. *Gyrodynamics*. Springer Verlag, New York, 1974.

[Zho95] K. Zhou, J. Doyle and K. Glover. *Robust and Optimal Control*. Prentice Hall International Inc., Upper Saddle River, New Jersey, 1995.

[Zoe02] J. Zoethout. *Design and integration of position sensing systems*. PhD thesis, EPFL, 1015 Lausanne, Switzerland, 2002.

Curriculum Vitae

Name: Thomas Bosgiraud
Date of Birth: 28.04.1979
Place of Birth: Paris, France
Nationality: French

2004-2008:
Ecole Polytechnique Fédérale de Lausanne (EPFL)
Ph.D. project at the Laboratoire de Systèmes Robotiques
in collaboration with the Japanese company JTEKT Corp. (Nara, Japan).

Publication: Overcoming of High Centrifugal Forces
in a 5 DOF Micro AMB Gyroscope.
11th Int. Symp. on Magnetic Bearings (ISMB11), 2008.
and Journal of System Design and Dynamics.

1999-2004:
Eidgenössische Technische Hochschule Zürich (ETHZ)
Master of Sciences in Electrical Engineering and Information Technologies
with majors in mechatronics, automatic control and biomedical engineering.

Publication: A Model to Predict the Effect
of Calf Muscle Stimulation at Push-Off
9th IFESS Conference, 2004.

1997-1999:
Classes Préparatoires Stanislas, Paris, France.
with majors in mathematics and physics.

1999:
French scientifical Baccalauréat, Blois, France.